Title

Technoeconomic optimization and thermohydraulic characterization of superalloy supercritical CO2 microtube shell-and-tube heat exchangers

Author

Krishna, Akshay Bharadwaj

Publication Date

2022

Peer reviewed|Thesis/dissertation

UNIVERSITY OF CALIFORNIA

Los Angeles

Technoeconomic optimization and thermohydraulic characterization of superalloy supercritical CO_2 microtube shell-and-tube heat exchangers

A dissertation submitted in partial satisfaction

of the requirements for the degree

Doctor of Philosophy in Mechanical Engineering

by

Akshay Bharadwaj Krishna

2022

ABSTRACT OF THE DISSERTATION

Technoeconomic optimization and thermohydraulic characterization of superalloy supercritical CO_2 microtube shell-and-tube heat exchangers

by

Akshay Bharadwaj Krishna

Doctor of Philosophy in Mechanical Engineering

University of California, Los Angeles, 2022

Professor Timothy S. Fisher, Chair

High-temperature supercritical CO_2 Brayton cycles are promising candidates for future stationary power generation and hybrid electric propulsion applications. Supercritical CO_2 thermal cycles potentially achieve higher energy density and thermal efficiency by operating at elevated temperatures and pressures. Heat exchangers are indispensable components of aerospace systems and improve efficiency of operation by providing necessary heat input, recovery, and dissipation. Tubular heat exchangers with unconventionally small tube sizes (tube diameters less than 5 mm) are promising components for supercritical CO_2 cycles and provide excellent structural stability. Accurate and computationally efficient estimation of heat exchanger performance metrics at elevated temperatures and pressures is important for the design and optimization of sCO_2 systems and thermal cycles. In this study, new Colburn and friction factor correlations are developed to quantify shell-side heat transfer and friction characteristics of flow within heat exchangers in the shell-and-tube configuration. Using

experimental and CFD data sets from existing literature, multivariate regression analysis is conducted to achieve correlations that capture the effects of multiple critical geometric parameters. These correlations offer superior accuracy and versatility as compared to previous studies and predict the thermohydraulic performance of about 90% of the existing experimental and CFD data within ±15%. Supplementary thermohydraulic performance data is acquired from CFD simulations with sCO_2 as the working fluid to validate the developed correlations and to demonstrate application to sCO_2 heat exchangers. A computationally efficient and accurate numerical model is developed to predict the performance of STHXs. The highly accurate correlations are utilized to improve the accuracy of performance predictions, and the concept of volume averaging is used to abstract the geometry for reduced computation time. The numerical model is validated by comparison with CFD simulations and provides high accuracy and significantly lower computation time compared to existing numerical models. A preliminary optimization study is conducted, and the advantage of using supercritical CO_2 as a working fluid for energy systems is demonstrated. A microtube heat exchanger is fabricated, and essential design and fabrication guidelines of a compact shell-and-tube heat exchanger with microtubes (with inner diameters of 1.75 mm) are provided. A heat exchanger test rig is used to evaluate the thermohydraulic performance of this heat exchanger with supercritical CO_2 and air as working fluids. Thermohydraulic data are reported for more than forty sets of experiments with varying Reynolds numbers for shell and tube flows. Critical performance metrics are calculated from the data and compared with predictions from the numerical model. The average deviations between the experimental and model results fall within 10% for all critical metrics. This excellent agreement validates the numerical model for supercritical CO_2 heat exchanger optimization and

scale-up. A generalized costing model is developed to estimate the capital costs incurred to manufacture microtube shell-and-tube heat exchangers. This model is utilized in conjunction with an accurate and efficient 2D numerical shell-and-tube heat exchanger performance prediction model to conduct optimization studies with two key objectives - minimization of cost and maximization of heat exchanger power density - on supercritical CO_2 microtube heat exchangers utilizing superalloy Haynes 282 as the solid material. A methodology is then demonstrated to optimize these heat exchangers for aerospace applications, and highly compact and cost-effective optimal designs with power density around 20 kW/kg and cost per conductance less than 5 $\$ \cdot \mathrm{K/W}$ are obtained.

The dissertation of Akshay Bharadwaj Krishna is approved.

Jayathi Y. Murthy

Nasr M. Ghoniem

Xiaochun Li

Portonovo S. Ayyaswamy

Timothy S. Fisher, Committee Chair

University of California, Los Angeles

2022

Contents

List of Figures

List of Tables

Acknowledgments

I would like to express my sincere gratitude and appreciation to my advisor, Prof. Timothy Fisher, for his constant encouragement and invaluable mentorship. His guidance through each step of the process played an integral role in defining the path of my research and helped majorly in my progress as a researcher and a person.

I would also like to thank the following people, whose contribution to this research work and my academic development is highly appreciated:

- Prof. Ivan Catton, for his mentorship, critical technical inputs and constant support.
- Prof. Portonovo Ayyaswamy, for his extensive contribution and continuous backing.
- Prof. Jayathi Murthy, Prof. Xiaochun Li and Prof. Nasr Ghoniem for their valuable advice and research collaboration.
- Dr. Kaiyuan Jin and Mr. Zachary Wong, for their research collaborations, stimulating discussions and insightful feedback.
- Honeywell Aerospace and Hal Strumpf in particular for their research collaboration and critical research inputs.
- Members of the SHOTEAM project and Nanoscale Transport Research Group (NTRG), especially Abdalla and Mostafa, for their prompt and unquestioning help whenever I needed them.

- Advanced Research Projects Agency–Energy and University of California, Los Angeles, for their generous financial support.

- Any others who have contributed to this work who were left unnamed.

Finally, I would like to thank my parents, Mythili and Krishna, brother, Anirudh, and wife, Divya, whose undying love and support, helped me become the person I am today. I will forever be indebted to them for their willingness to support both my academic and extra-curricular pursuits, disregarding any of their personal difficulties. My academic work and accolades are a dedication to their unconditional love.

Vita

Education

Master of Science in Mechanical and Aerospace Engineering 2018 - 2020

University of California, Los Angeles

Bachelor of Technology in Mechanical Engineering 2014 - 2018

Vellore Institute of Technology, Vellore

Journal publications

A. B. Krishna, K. Jin, P. S. Ayyaswamy, I. Catton, T. S. Fisher, Technoeconomic optimization of superalloy supercritical CO_2 microtube shell-and-tube heat exchangers, Under review.

K. Jin, **A. B. Krishna**, Z. Wong, P. S. Ayyaswamy, I. Catton, T. S. Fisher, Thermohydraulic experiments on a supercritical carbon dioxide - air microtube heat exchanger, Under review.

A. B. Krishna, K. Jin, P. S. Ayyaswamy, I. Catton, T. S. Fisher, Modeling of supercritical CO_2 shell-and-tube heat exchangers under extreme conditions. Part 1: Correlation development, ASME Journal of Heat Transfer (2022).

A. B. Krishna, K. Jin, P. S. Ayyaswamy, I. Catton, T. S. Fisher, Modeling of supercritical CO_2 shell-and-tube heat exchangers under extreme conditions. Part 2: Heat exchanger model, ASME Journal of Heat Transfer (2022).

Z. Wong, K. Jin, **A. B. Krishna**, I. Catton, T. S. Fisher, Shell-side maldistribution metric for supercritical CO_2 shell-and-tube heat exchangers, In preparation.

N. Wolff, **A. B. Krishna**, K. Jin, I. Ghosh, T. S. Fisher, Computationally efficient solutions of thermal performance for annular fins in heat exchangers operating at extreme temperatures and pressures, In preparation.

L. Pretorius, K. Jin, **A. B. Krishna**, T. S. Fisher, Hybrid electric propulsion with supercritical carbon dioxide thermal cycle for future aviation systems, In preparation.

Software publication

A. B. Krishna, K. Jin, P. S. Ayyaswamy, I. Catton, T. S. Fisher, akshayb29/Shell-and-Tube-Heat-Exchanger-STHX-numerical-model: Shell-and-tube heat exchanger numerical model, Zenodo. https://doi.org/10.5281/zenodo.5117859

Appointments

University of California, Los Angeles

Teaching Assistant

– MAE 105D, Transport Phenomena 2020

– MAE 157, Basic Mechanical and Aerospace Engineering Laboratory 2022

Mentor

– Center for Excellence in Engineering and Diversity (CEED) E87, Introduction to Engineering Disciplines 2021

Chapter 1: Introduction

1.1 Motivation

Increasing the capacity and efficiency of energy conversion processes is critical to alleviate worldwide energy and environmental challenges and support global economic development. Supercritical carbon dioxide (sCO_2) is considered to be a promising working fluid in future energy conversion systems for providing superior thermal efficiency [1–3], more compact system footprint [4–6] than the conventional power generation cycles such as the air Brayton cycle and the steam Rankine cycle [1, 7, 8], and higher system stability [9, 10] in comparison to conventional working fluids. Good chemical stability, high density at high temperatures, and a low critical point (7 MPa and 300 K) make sCO_2 a more attractive candidate fluid for operation in energy systems than other supercritical fluids [11–13]. With these benefits, sCO_2 Brayton cycles are being considered for high-temperature power generation using fuels such as coal [10, 14] and nuclear [12], solar-thermal power applications [2, 13], hybrid power for electric propulsion systems [11, 15], concentrated solar power (CSP) [13, 16, 17], and waste heat to power (WHP) [18, 19].

Heat exchangers (HXs) are essential components in sCO_2 Brayton cycles and provide significant thermal transport, recovery, and management [20–22]. The heat-source HX is indispensable and provides necessary energy input for closed sCO_2 cycle systems. In addition, recuperative HXs (named 'recuperators') are also commonly implemented to recover waste heat from the turbine outlet stream for improved system energy efficiency [23, 24]. Given that sCO_2 HXs are highly compact and operate under extreme temperatures and pressures,

the design and fabrication processes are more complex than conventional approaches and require further investigation for more accurate performance evaluation [25–28]. Numerous configurations of HXs are being developed for improved performance [29–31]. Plate HXs with micro-scale channels generally have the smallest footprints and therefore are considered as attractive options for sCO_2 applications [32, 33]. Among plate HXs, printed circuit HXs (PCHXs) have gained particular attention for their high heat transfer area-to-volume ratios, long-term structural integrity, and attractive heat transfer performance [20, 29, 34]. In recent years, multiple promising flow channel designs, including straight [35], zigzag [35, 36], and finned [37, 38] have been utilized for sCO_2 PCHXs to achieve superior performance metrics. Various experimental studies [39–42] have been performed to characterize the thermohydraulic behavior of sCO_2 for these PCHX layouts and provide the necessary design basis for future scaled-up sCO_2 applications.

Arguably, the most common type of high-temperature and high-pressure HX is the shell-and-tube heat exchanger (STHX) [43, 44]. This type consists of a shell with parallel tubes and baffles inside. A fluid flow (tube-side flow) runs inside the tubes and heats or cools the second flow (shell-side flow) that runs over the tube outer surfaces and inside the shell. Heat transfer is enhanced by having multiple passes on the shell side. This enhancement is usually achieved by placing baffles in the fluid stream on the shell side to guide the flow. These configurations are generally versatile and can withstand extreme operating conditions, largely because the circular flow boundaries in tubular HXs have excellent structural stability at high temperatures and pressures [45, 46]. STHXs are popular owing to their high effectiveness, versatility in operation, and reduced cost [47–49] but are generally heavier and occupy larger volumes due to the usage of tubes with inner diameter larger than 5 mm [50]. In recent years,

multi-path HXs using microtubes, namely microtube STHXs (MT-STHXs), have gained interest and the first sCO_2 microtube HX was proposed and fabricated by Thar Energy LLC in 2017 [51]. Using tubes of $\approx$ 1mm diameter, several HX prototypes with a single flow path achieved a similar heat transfer area density to PCHXs ($\approx$ 1800 m2/m3). MT-STHXs are gaining interest as they exhibit all advantages of STHXs and are compact with high power densities [51]. The drawbacks of STHXs are mitigated in MT-STHXs by utilizing tubes of smaller inner diameters.

Given that the geometries and operating conditions are unusual in comparison to typical applications, the thermohydraulic behavior of such sCO_2 STHXs requires further study, particularly with respect to constraints imposed by extreme thermomechanical conditions [52]. Therefore, aside from selection of working fluids, selection of solid material is crucial because the MT-STHX needs to withstand long duration of operation at elevated temperatures and pressures. Superalloys such as Haynes 282 are promising candidates due to their high creep strength at extreme operating conditions [53–55]. Although Haynes282 have the above-mentioned advantages, creep property of the material varies considerably with precipitate and dislocation structure, stress triaxiality, average grain size, heat treatment method, and temperature gradient effects. Creep data is required from samples that have thickness similar to that of the thin-walled tubes as the number of grains through the thickness significantly influences the creep strength of the material [56]. Additionally, experimental data needs to be obtained at the heat affected zones to provide information on material processing and behavior of the material under different loading conditions.

In order to optimize for MT-STHX performance, an accurate and computationally efficient performance prediction model is required. One of the main challenges is that prior

correlations for friction and Colburn factor for flow over tube banks are insufficiently accurate and there is insufficient evidence to show that these correlations are applicable to sCO_2 flow. Additionally, most HX numerical models are either computationally expensive and resource intensive or less accurate in prediction of thermohydraulic performance. Another major bottleneck is that although there is experimental data for PCHXs in the literature, experimental data for tubular HXs with sCO_2 as a working fluid remain scarce. In this thesis, we develop highly accurate and unified correlations for Colburn and friction factor that can be applied to characterize flow over bare, disc-finned, and cylindrical pin-finned tube banks. We utilize these correlations to develop a high fidelity, computationally efficient MT-STHX performance prediction numerical model. We obtain experimental data for thermohydraulic performance of a fabricated MT-STHX to validate the developed model. Even though a proven numerical model is developed, current cost models are either applicable to devices with steel as the solid material or are not comprehensive enough to account for the various components of heat exchangers. We develop a generalized form for the cost estimation of MT-STHXs, perform cost and power density optimization studies, and provide a potentially promising objective function for optimization of future aerospace systems.

1.2 Organization of the document

This thesis is divided into 4 main chapters, each of which contribute significantly towards achieving the final goal of optimizing MT-STHXs for application in the aerospace industry. Since every chapter revolves around different fundamentals, an extensive literature review is provided in each chapter in context. The main highlights of the various chapters of the thesis are summarized below.

Chapter 2 discusses the development of accurate and unified Colburn and friction factor correlations by utilizing existing experimental and CFD data sets to predict flow over bare, disc-finned, and cylindrical pin-finned tube banks. These correlations offer superior accuracy and versatility and predicts about 90% of existing data with ±15% error.

Chapter 3 utilizes the correlations from Chapter 2 to develop a highly versatile, computationally efficient, and accurate numerical model to predict the thermohydraulic performance of MT-STHXs. The model is initially validated using CFD simulations and a preliminary optimization study is conducted to display the potentially significant benefits of utilizing sCO_2 as the working fluid for future energy systems.

Chapter 4 details the fabrication of an MT-STHX and an sCO_2 test rig to predict the thermohydraulic performance of MT-STHX. Experiments are conducted with high pressure sCO_2 as the internal fluid and high temperature air as the external fluid. The data is compared with predictions from the numerical model and shows great agreement. The experiments in this chapter provide confidence and validation to the numerical model developed in Chapter 3.

Chapter 5 provides the development of a generalized costing model to estimate capital cost of microtube shell-and-tube heat exchangers. Optimization studies are performed to optimize MT-STHXs of various capacities for cost and power density. A cost-constrained, power density maximization objective function is provided to optimize future aerospace systems and promising MT-STHX designs with high power densities and low costs are obtained.

Chapter 2: Thermohydraulic performance prediction correlations

2.1 Introduction

Characterization of the hydraulic and heat transfer behavior of both shell-side and tube-side flows in STHXs plays an important role in performance prediction and design optimization. Friction factor, f, and Nusselt number, Nu, or Colburn factor, j_H, are commonly used to characterize flow pressure drop and heat transfer rates. The tube-side flow physics is relatively simple, and the relevant friction factors and Nusselt numbers can be calculated accurately by using Petukhov formula [57] and Gnielinski correlation [58], respectively. The shell-side flow physics is much more complex and dominated by multiple geometric parameters, such as tube diameter, pitch ratios, shell diameter, baffle geometry, and fin parameters. Correlations for the thermohydraulic behavior of shell-side flow must be accurate, generalizable, and account for critical geometric parameters.

Owing to the popularity of STHXs, extensive research has been conducted in characterizing the heat transfer of tube bundles in crossflow [59, 60]. Grimson [61] and Pierson [62] conducted multiple experiments and developed generalized heat transfer correlations for tube bundles in boilers. Extensive studies for HXs were reported by Gregorig [63] and Kays and London [64], who conducted experiments to calculate the hydraulic resistance and heat transfer characteristics of many test cases with varying pitch dimensions, tube diameters,

A large portion of this chapter created the paper by A. B. Krishna, K. Jin, P. S. Ayyaswamy, I. Catton, and T. S. Fisher, titled "Modeling of supercritical CO_2 shell-and-tube heat exchangers under extreme conditions. Part 1: Correlation development" published in ASME Journal of Heat Transfer. DOI: 10.1115/1.4053510

and arrangements. Zukauskas [65] developed Nusselt number correlations for low, moderate, and high Re flows over both inline and staggered tube bundle configurations.

Staggered tubes potentially provide better thermohydraulic performance and the correlation of Nusselt number proposed by Zukauskas is

$$Nu = CRe^{0.60}Pr^{0.36}\left(\frac{Pr}{Pr_f}\right)^{0.25} \tag{2.1}$$

where C is a function of the transverse pitch to longitudinal pitch ratio of the tube bundle. Pressure drop calculations for flow over a bank of tubes have been performed based on friction factor data obtained by Jakob [66], Gunter and Shaw [67], Zukauskas [65]. Boucher and Lapple [68] provided a correction to the method of calculation by Gunter and Shaw [67]. A commonly used data set for pressure drop and friction factor was developed by Zukauskas [65], who plotted the data as a function of Reynolds number for various tube bundle configurations.

Heat transfer can be further enhanced by increasing the surface area between the two flows within HXs. For shell-and-tube configuration, this increase in surface area is typically achieved by creating augmentations on tube outer surfaces. Tube augmentations also act as turbulence promoters and cause periodic vortex shedding that can increase the heat transfer coefficient [69–73]. Among the studies conducted in the past, the most popular choice of augmentations were disc fins and pin fins on tubular surfaces. Kays and London [64] performed experiments to obtain data for thermohydraulic performance of tube banks with disc fins as augmentations for various tube bank arrangements and disc-fin geometries. Tian et al. [74] developed CFD models to elucidate the heat transfer and friction characteristics of staggered bank of tubes with circular pin-fin enhancements. Even though pin-fins usually

exhibit a higher pressure drop than other fins, Sahiti et al. [75] numerically predicted that pin-fins are possibly the most effective method to enhance heat transfer.

Biery [76] utilized the data of Mirkovic [77], Zukauskas [65], and Kays and London [64] for flow over bare tube banks to create a transformation for emulating heat transfer over a bank of tubes augmented with continuous circular fins and segmented disc fins, culminating in a generalized correlation for Nusselt number [76]:

$$Nu = CRe^{0.6}Pr^{0.33} \tag{2.2}$$

where C is a complex function of the geometric parameters of the tube bundle. For flow over pin-fin tube bundles, none of the previous studies has developed correlations to predict thermohydraulic behavior.

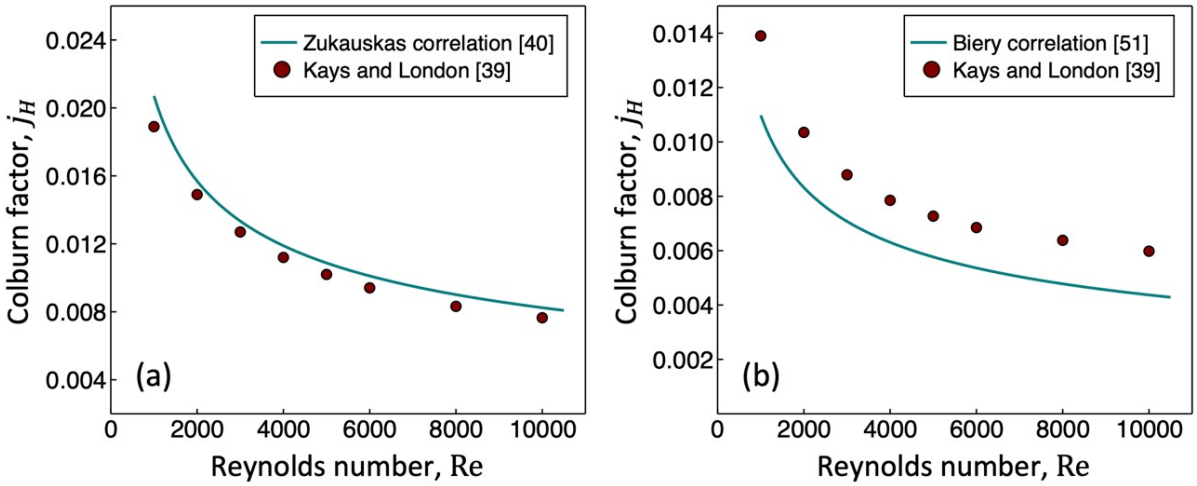

Figure 2.1: Comparison between the Colburn factors obtained from (a) Kays and London [64] experimental data and the Zukauskas correlation [65], and (b) Kays and London [64] experimental data and the Biery correlation [76].

To understand the overall accuracy of the correlations in Eqs. 2.1 and 2.2, a comparative analysis of the correlations is performed with the experimental data from Kays and London [64]. The average error, considering all cases, between the Zukauskas correlation [65] and data from Kays and London [64] for flow over bare tubes is 2.4%. The case with the largest error is shown in Fig. 2.1(a) and has an average error of 7%. The Zukauskas correlation [65] is highly accurate but applicable only for bare tube geometries. On the other hand, the Biery correlation [76] for Colburn factor can be applied to both bare and disc-finned tubes. The average error, considering all the cases, between the Biery correlation [76] and data from Kays and London [64] for flow over disc-finned tubes is 11.7%. However, this correlation predicts the performance of some disc-finned tube bank cases with a relatively high error of 20.9% as shown in Fig. 2.1(b).

Previous studies do not cover friction factor correlations both for bare and finned tube bundles, Colburn factor correlations for pin-finned tube bundles, and can be insufficiently accurate in their prediction capability. In addition, there is insufficient evidence that proves the previous correlations are applicable for sCO_2 as working fluids. The objective of the current study is to develop highly accurate and unified correlations to predict the Colburn and friction factor for sCO_2 flow over bare, disc-finned, and cylindrical pin-finned tube banks. Thirty-nine data sets (312 data points) of thermohydraulic performance data are employed and multivariate regression analysis is performed for correlation development. CFD simulations using sCO_2 as the external fluid domain at high temperature and pressure are performed to validate the accuracy of the developed correlations. The developed correlations are compared with existing and newly obtained data and their superior accuracy of prediction is demonstrated.

2.2 Methodology

In this section, important length scales and data sets used for correlation development are introduced. The various forms of correlations and multivariate regression analysis performed are discussed in the latter half of this section.

Figure 2.2 provides a representative schematic for flow over tube banks and defines the various geometric parameters associated with the tube bundle, tubes, and fins. Thirty-nine unique variations of bare, disc-finned, and cylindrical pin-finned tube banks are used to develop correlations with the geometries of Fig. 2.2 as a baseline. All data in this chapter involve tube bundles in a staggered configuration. Staggered tube bundles have been chosen over inline tube bundles due to their superior thermal performance particularly under volume constraints associated with aerospace applications.

Reynolds number is a measure of inertial and viscous forces in the flow, as well as its turbulent character. Hydraulic diameter, D_h, is defined by Kays and London [64] as a length scale to compute the Reynolds number of flows over various types of tube bundle geometries, including bare and finned tube banks. The hydraulic diameter is a function of the minimum open area and the total area of flow, and is defined as

$$D_h = \frac{2A_c P_l}{A_{HT}} \tag{2.3}$$

Reynolds number is calculated as

$$Re_{D_h} = \frac{u_{max} D_h}{\nu} \tag{2.4}$$

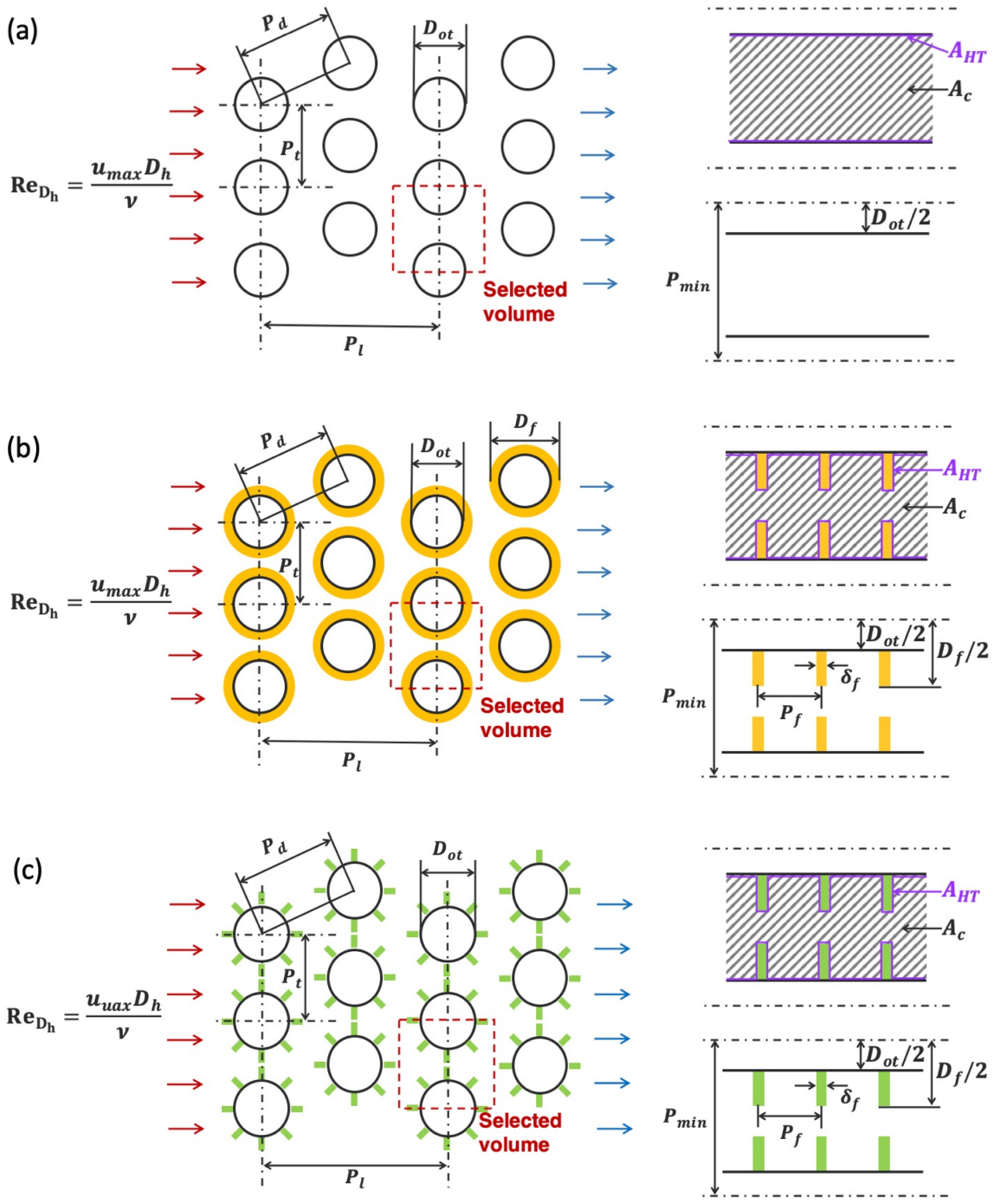

Figure 2.2: Schematic of the staggered tube bank (left). Side view of the selected volume depicting the cross-sectional and heat transfer areas (top right). Geometric parameters (bottom right associated with (a) bare, (b) disc-finned, and (c) cylindrical pin-finned tube banks.

where u_{max} is the maximum flow velocity located at the minimum free flow area, A_{min}. Zhou [78] used volume averaging theory (VAT) to determine a length scale (D_{VAT}) to collapse the Colburn and friction factor data in the development of correlations. Hydraulic diameter and Reynolds number as defined by VAT are given below. Further details regarding VAT and its related parameters is provided in Chapter 3.

$$D_{VAT} = \frac{4\phi}{S_w} \tag{2.5}$$

$$Re_{VAT} = \frac{u_{avg} D_{VAT}}{\nu} \tag{2.6}$$

where $\phi = \frac{\text{Volume occupied by the component}}{\text{Total volume}}$ and is the volume fraction of the fluid, and $S_w = \frac{\text{Tube area wetted by the fluid + Fin area wetted by the fluid}}{\text{Total volume}}$ and is the specific wetted surface area of the fluid.

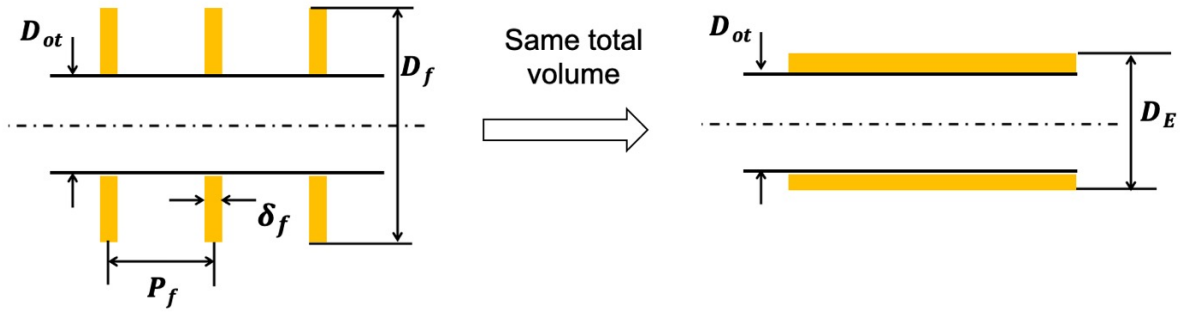

Figure 2.3: Schematic depicting the concept of effective diameter, D_E.

We propose the effective diameter, D_E, as an additional length scale in correlations to better describe the geometry of fins on tubes. As shown in Fig. 2.3, the effective diameter is defined as the diameter of the tube if the fins were melted and spread out evenly along the tube surfaces. Effective diameter is based on conservation of total volume and is given by

$$\frac{\pi D_E^2 P_f}{4} = V_{tube} + V_{fin} \tag{2.7}$$

Given that D_h is a characteristic length for the whole flow path, the ratio between D_h and D_E is used to provide a measure of the compactness of the tube bundle (higher ratios correspond to less compactness). For the bare-tube case, fin diameter is equal to tube diameter and $D_h/D_E = D_h/D_f$. For augmented tubes with a high density of fins, fin thickness is almost the same as the fin pitch ($\delta_f \rightarrow P_f$), and therefore, $D_h/D_E = D_h/D_f$. More parameters, such as the fin diameter to tube outer diameter ratio, D_f/D_{ot}, and the fin spacing to fin pitch ratio, $(P_f - \delta_f)/P_f$, are used in the developed correlations to capture additional fin geometry effects.

2.2.1 Datasets used for correlation development

The critical geometric parameters for thirteen selected bare tube banks are listed in Table 2.1 and the data is obtained from experiments and correlations that utilize air as the working fluid. The first seven geometric configurations (BT1 – BT7) are from Kays and London's [64] experiments and the remaining six cases (BT8 – BT13) are chosen to accommodate a wider range of values for the compactness of the heat tube bundle, D_h/D_E. For these cases (BT8 – BT13), the necessary Colburn and friction factor data are obtained from the Zukauskas correlation and friction factor plot [65]. The Kays and London [64] experimental data measurements have a 5% measurement error.

Table 2.1: Geometric details of the bare tube bank configurations from Kays and London [64] experimental data (BT1 – BT7) and using the Zukauskas correlation (BT8 – BT13) [65].

Case #	D_{ot}[mm]	P_t[mm]	P_l[mm]	D_h/D_E
BT1	6.35	9.53	15.88	0.796
BT2	9.53	14.29	23.82	0.796
BT3	9.53	11.91	23.82	0.398
BT4	9.53	14.29	19.05	0.637
BT5	9.53	14.29	28.58	0.955
BT6	9.53	19.05	19.05	1.056
BT7	9.53	23.81	14.29	0.875
BT8	9.65	24.77	20.32	4.197
BT9	16.38	31.29	34.29	2.452
BT10	16.38	46.94	34.29	4.970
BT12	19.66	39.55	44.45	2.912
BT12	19.66	69.22	44.45	7.256
BT13	19.66	50.34	34.93	3.530

The critical geometric parameters of the tubes with fins for thirteen disc-finned tube banks are listed in Table 2.2. All relevant experimental data are obtained from Kays and London's [64] study of flow of air over disc-finned tube banks (DF1 – DF13). The Kays and London [64] experimental data measurements have a 5% measurement error.

Table 2.2: Geometric details of the disc-finned tube bank configurations from Kays and London [64] experimental data.

Case #	D_{ot}[mm]	P_t[mm]	P_l[mm]	D_f[mm]	δ_f[mm]	P_f[mm]	D_h/D_E
DF1	9.65	24.77	40.64	23.37	0.457	3.460	0.362
DF2	9.65	24.77	40.64	23.37	0.457	2.913	0.292
DF3	10.67	24.77	40.64	21.87	0.483	2.913	0.320
DF4	16.38	31.29	68.58	28.47	0.254	3.629	0.381
DF5	16.38	31.29	68.58	28.47	0.254	2.920	0.309
DF6	16.38	46.94	68.58	28.47	0.254	2.920	0.657
DF7	19.66	39.55	88.90	37.16	0.305	2.807	0.230
DF8	19.66	50.34	88.90	37.16	0.305	2.807	0.369
DF9	19.66	69.22	88.90	37.16	0.305	2.807	0.610
DF10	19.66	69.22	40.64	37.16	0.305	2.807	0.217
DF11	19.66	50.34	69.86	37.16	0.305	2.807	0.290
DF12	26.01	49.76	104.80	44.12	0.305	2.886	0.206
DF13	26.01	78.21	104.80	44.12	0.305	2.886	0.475

The critical geometric parameters of the tubes and fins for thirteen cylindrical pin-finned tube banks are listed in Table 2.3. All relevant thermohydraulic performance data for flow of air over circular pin-finned tube banks are obtained from the study by Tian et al. [74] (CPF1 – CPF13). The CFD data from the study by Tian et al. has an average error of 7.25% when compared with Zukauskas correlation [74].

Table 2.3: Geometric details of the cylindrical pin-finned tube bank configurations from Tian et al. [74] CFD data.

Case #	D_{ot}[mm]	P_t[mm]	P_l[mm]	D_f[mm]	δ_f[mm]	P_f[mm]	N_f	D_h/D_E
CPF1	30	96	132	45	1.5	8	10	2.84
CPF2	30	96	132	45	2.0	8	10	2.33
CPF3	30	96	132	45	3.0	8	10	1.63
CPF4	30	96	132	45	4.0	8	10	1.18
CPF5	30	96	132	45	1.5	8	6	3.56
CPF6	30	96	132	45	1.5	8	16	2.17
CPF7	30	96	150	45	1.5	8	10	3.23
CPF8	30	96	180	45	1.5	8	10	3.88
CPF9	30	75	132	45	1.5	8	10	1.85
CPF10	30	66	132	45	1.5	8	10	1.43
CPF11	30	105	132	45	1.5	8	10	3.27
CPF12	30	96	132	45	3.0	12	10	2.29
CPF13	30	96	132	45	3.0	16	10	2.78

2.2.2 Correlation development

Table 2.4 lists the six forms of correlations that were used to fit all selected experimental and CFD data. The correlations assume a power-law form for five of the six cases, while a polynomial correlation (PC) was assumed for the last case. Reynolds number is defined

using the hydraulic diameter as the length scale for all cases, except for PLC4 and PLC5. The tube diameter is used as the length scale for PLC4, while the VAT hydraulic diameter is used for PLC5.

Table 2.4: Forms of correlations developed.

Correlation Form (j_H or f)	
Power law 1 (PLC1)	$C_1 \left(\frac{D_h}{D_E}\right)^{C_2} Re_{D_h}^{C_3}$
Power law 2 (PLC2)	$C_1 \left(\frac{D_h}{D_{ot}}\right)^{C_2} Re_{D_h}^{C_3}$
Power law 3 (PLC3)	$C_1 \left(\frac{D_h}{D_E}\right)^{C_2} \left(\frac{P_t}{D_{ot}}\right)^{C_3} \left(\frac{P_l}{2D_{ot}}\right)^{C_4} \left(\frac{D_f}{D_{ot}}\right)^{C_5} \left(\frac{P_f-\delta_f}{P_f}\right)^{C_6} Re_{D_h}^{C_7}$
Power law 4 (PLC4)	$C_1 \left(\frac{P_t}{D_{ot}}\right)^{C_2} \left(\frac{P_l}{2D_{ot}}\right)^{C_3} \left(\frac{D_f}{D_{ot}}\right)^{C_4} \left(\frac{P_f-\delta_f}{P_f}\right)^{C_5} Re_{D_t}^{C_6}$
Power law 5 (PLC5)	$C_1 \left(\frac{D_{VAT}}{D_E}\right)^{C_2} \left(\frac{P_t}{D_{ot}}\right)^{C_3} \left(\frac{P_l}{2D_{ot}}\right)^{C_4} \left(\frac{D_f}{D_{ot}}\right)^{C_5} \left(\frac{P_f-\delta_f}{P_f}\right)^{C_6} Re_{D_{VAT}}^{C_7}$
Polynomial (PC)	$\left[C_1 + C_2\frac{D_h}{D_E} + C_2\left(\frac{D_h}{D_E}\right)^2\right] Re_{D_h}^{\left[C_4+C_5\frac{D_h}{D_E}+C_6\left(\frac{D_h}{D_E}\right)^2\right]}$

Using Colburn and friction factor data from the foregoing experimental and CFD studies, the coefficients and exponents, C_1-C_7, are determined by performing multivariate regression analysis on the six correlation forms. The regression analysis is carried out by taking the log-

arithm of each correlation equation [79]. Taking PLC3 as an example, the reduced equation takes the form shown below.

$$\ln(j_H) \text{ or } \ln(f) = \ln(C_1) + C_2 \ln\left(\frac{D_h}{D_E}\right) + C_3 \ln\left(\frac{P_t}{D_{ot}}\right) + C_4 \ln\left(\frac{P_l}{D_{ot}}\right) + C_5 \ln\left(\frac{D_f}{D_{ot}}\right) + C_6 \ln\left(\frac{P_f - \delta_f}{P_f}\right) + C_7 \ln\left(Re_{D_h}\right) \quad (2.8)$$

When using PLC3 to quantify flow characteristics of bare tube banks, $D_f = D_t$ and $\delta_f = 0$, and thus PLC3 reduces to the following form:

$$j_H \text{ or } f = C_1 \left(\frac{D_h}{D_E}\right)^{C_2} \left(\frac{P_t}{D_{ot}}\right)^{C_3} \left(\frac{P_l}{D_{ot}}\right)^{C_4} Re_{D_h}^{C_7} \quad (2.9)$$

The development and comparison of these correlations are assessed in the following section.

2.3 Results and discussion

Multivariate regression analysis was performed using thirteen training data sets each for bare, disc-finned, and cylindrical pin-finned tube banks. Each data set contains eight data points (total 39 data sets and 312 data points) with Reynolds numbers ranging from 1,000 to approx. 10,000 and Pr=0.73. The PLC3 form of correlation produces the best agreement with the experimental and CFD data among the five correlation forms, and hence the correlations shown in this section assume the PLC3 form. Three sets of Colburn and friction factor correlations have been developed and are reported in the section below.

2.3.1 Unified correlations for various tube bank configurations

In comparison to bare tube bundles, the finned-tube geometry in HXs provide superior heat transfer performance but also incur higher pressure drops and manufacturing costs. Different fin shapes also have unique consequences for HX thermohydraulic and cost performance.

Therefore, unified and reliable correlations that are applicable for various tube bundle configurations are important for HX design and optimization of HX geometries. In this section, unified correlations for both Colburn and friction factors are developed using all thirteen data sets each for bare, disc-finned and cylindrical pin-finned tube banks. This type of correlation can be applied in the initial stages of designing a HX to provide direction as to whether fins provide an added advantage for the problem at hand, and what type of fin is most beneficial for the problem.

The Colburn factor for flow over bare, disc-finned, and cylindrical pin-finned tube banks takes the form

$$j_H = 0.47 \left(\frac{D_h}{D_E}\right)^{0.53} \left(\frac{P_t}{D_{ot}}\right)^{-0.21} \left(\frac{P_l}{D_{ot}}\right)^{-0.19} \left(\frac{D_f}{D_{ot}}\right)^{0.12} \left(\frac{P_f - \delta_f}{P_f}\right)^{-0.38} Re_{D_h}^{-0.40} \qquad (2.10)$$

Friction factor is given by

$$f = 0.54 \left(\frac{D_h}{D_E}\right)^{0.62} \left(\frac{P_t}{D_{ot}}\right)^{0.40} \left(\frac{P_l}{D_{ot}}\right)^{-0.20} \left(\frac{D_f}{D_{ot}}\right)^{-0.45} \left(\frac{P_f - \delta_f}{P_f}\right)^{-0.23} Re_{D_h}^{-0.23} \qquad (2.11)$$

These correlations are applicable within the ranges $0.2 \leq \frac{D_h}{D_E} \leq 7.3, 1.2 \leq \frac{P_t}{D_{ot}} \leq 3.5, 1.5 \leq \frac{P_l}{D_{ot}} \leq 6.0, 1.0 \leq \frac{D_f}{D_{ot}} \leq 2.4, 0.5 \leq \frac{P_f - \delta_f}{P_f} \leq 1.0$, and $1,000 \leq Re_{D_h} \leq 10,000$.

Figure 2.4 provides a comparison between the Colburn and friction factors obtained using Eqs. 2.10 and 2.11, and those obtained experimentally and using CFD (BT1-BT13, DF1-DF13, and CPF1-CPF13). The average and maximum deviations between the correlations and data are 6.5% and 33.9% for Colburn factor, and 8.3% and 34.2% for friction factor. In general, Eqs. 2.10 and 2.11 estimate 96% of the Colburn and 85% of the friction factor data within ±15%.

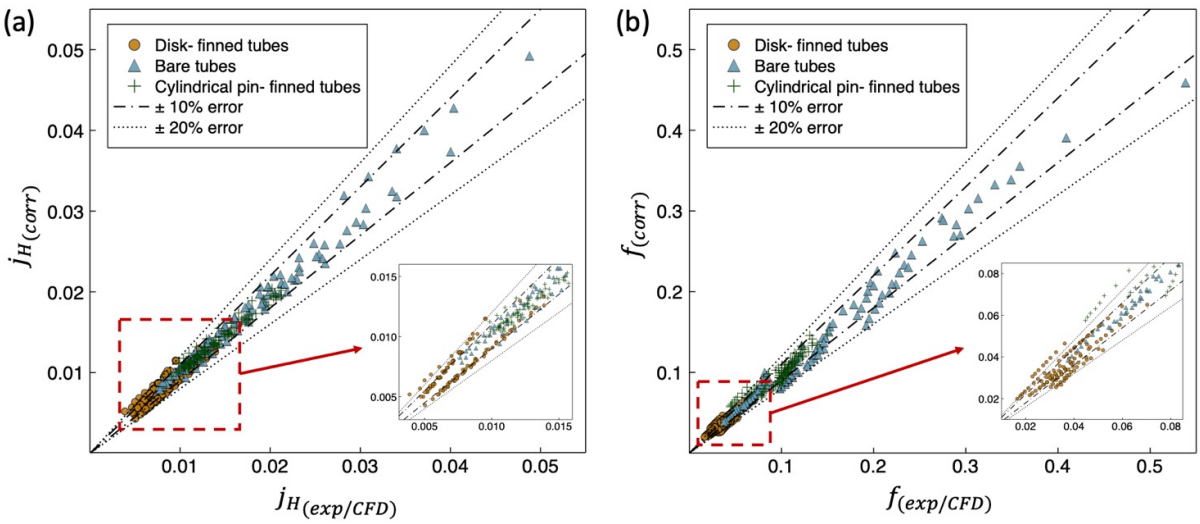

Figure 2.4: Experimental and CFD data for (a) Colburn and (b) friction factor plotted against the correlated values from Eqs. 2.10 and 2.11 for flow over bare, disc-finned, and cylindrical pin-finned tube banks.

2.3.2 Correlations for disc-finned tube banks

Disc-finned tubes find use in applications for which compact dissipation of heat is essential. This feature is commonly found in HXs (e.g., double pipe, shell-and-tube), cylinders of internal combustion engines, and cooling of nuclear reactors. These correlations have been developed specifically for disc-finned tube banks with fin-to-tube diameter ratio, D_f/D_{ot}, varying from 1 to 2.4. The continuous range for fin height enables the correlation to predict thermohydraulic performance of both bare and disc-finned tube banks. These correlations can be used when disc-finned tube banks are the target application, and to quantify the thermohydraulic performance of this system with greater accuracy compared to the unified correlations of Eqs. 2.10 and 2.11.

The Colburn factor for flow over bare and disc-finned tube banks takes the form

$$j_H = 0.41 \left(\frac{D_h}{D_E}\right)^{0.50} \left(\frac{P_t}{D_{ot}}\right)^{-0.18} \left(\frac{P_l}{D_{ot}}\right)^{-0.16} \left(\frac{D_f}{D_{ot}}\right)^{-0.33} \left(\frac{P_f - \delta_f}{P_f}\right)^{-2.35} Re_{D_h}^{-0.38} \quad (2.12)$$

Friction factor is given by

$$f = 0.63 \left(\frac{D_h}{D_E}\right)^{0.89} \left(\frac{P_t}{D_{ot}}\right)^{-0.09} \left(\frac{P_l}{D_{ot}}\right)^{-0.53} \left(\frac{D_f}{D_{ot}}\right)^{0.11} \left(\frac{P_f - \delta_f}{P_f}\right)^{-2.28} Re_{D_h}^{-0.21} \quad (2.13)$$

These correlations are applicable within the ranges $0.2 \leq \frac{D_h}{D_E} \leq 7.3, 1.2 \leq \frac{P_t}{D_{ot}} \leq 3.5, 1.5 \leq \frac{P_l}{D_{ot}} \leq 4.5, 1.0 \leq \frac{D_f}{D_{ot}} \leq 2.4, 0.8 \leq \frac{P_f - \delta_f}{P_f} \leq 1.0$, and $1,000 \leq Re_{D_h} \leq 10,000$.

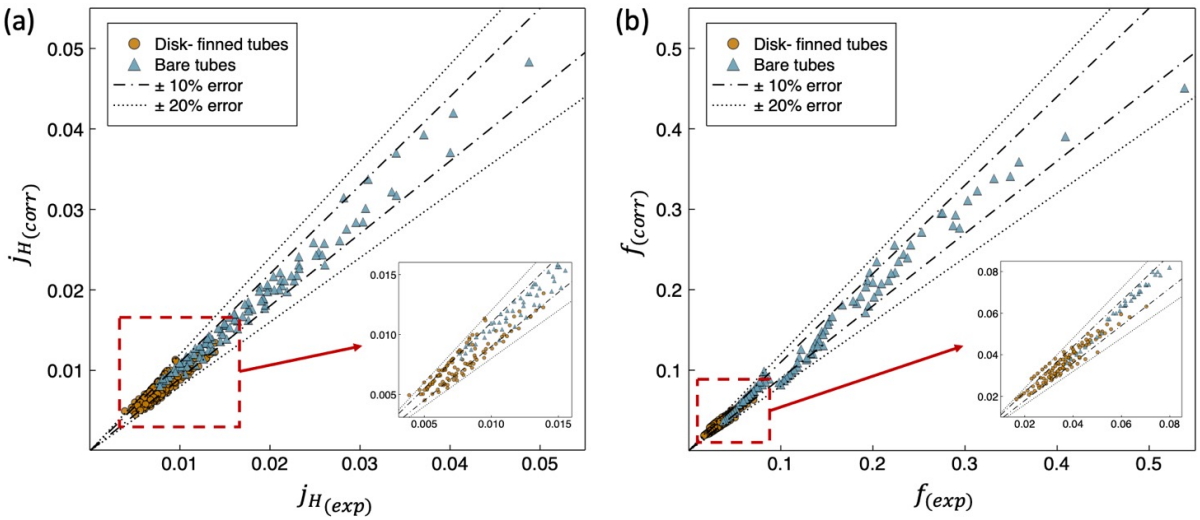

Figure 2.5: Experimental data for (a) Colburn and (b) friction factor plotted against the correlated values from Eqs. 2.12 and 2.13 for flow over bare and disc-finned tube banks.

Figure 2.5 provides a comparison between the Colburn and friction factors obtained using Eqs. 2.12 and 2.13, and those obtained experimentally (BT1-BT13 and DF1-DF13). The average and maximum deviation between the correlations and data are 7.5% and 27.4% for Colburn factor, and 6.6% and 25.1% for friction factor. Eqs. 2.12 and 2.13 estimate 94% of the Colburn and 93% of the friction factor data within ±15%.

2.3.3 Correlations for cylindrical pin-finned tube banks

Cylindrical pin-finned tubes are easy to clean, have a simple structure, and therefore are commonly used in HXs. These traits make tubes with pin-fins as augmentations a viable candidate for improving the performance of systems recovering waste heat. The correlations developed in this section are specific to cylindrical pin-finned tube banks using bare and cylindrical pin-finned tube bank data sets. Similar to Eqs. 2.12 and 2.13, the correlations in this section can accurately quantify the thermohydraulic performance of flow over cylindrical pin-finned tube banks with fin diameter to tube diameter ratio, D_f/D_{ot}, varying from 1 to 1.5.

The Colburn factor for flow over bare and cylindrical pin-finned tube banks takes the form

$$j_H = 0.38 \left(\frac{D_h}{D_E}\right)^{0.32} \left(\frac{P_t}{D_{ot}}\right)^{0.31} \left(\frac{P_l}{D_{ot}}\right)^{-0.01} \left(\frac{D_f}{D_{ot}}\right)^{0.03} \left(\frac{P_f - \delta_f}{P_f}\right)^{0.11} Re_{D_h}^{-0.41} \tag{2.14}$$

Friction factor is given by

$$f = 0.26 \left(\frac{D_h}{D_E}\right)^{0.32} \left(\frac{P_t}{D_{ot}}\right)^{1.14} \left(\frac{P_l}{D_{ot}}\right)^{0.07} \left(\frac{D_f}{D_{ot}}\right)^{-0.82} \left(\frac{P_f - \delta_f}{P_f}\right)^{0.23} Re_{D_h}^{-0.20} \tag{2.15}$$

These correlations are applicable within the ranges $0.4 \leq \frac{D_h}{D_E} \leq 7.3, 1.2 \leq \frac{P_t}{D_{ot}} \leq 3.5, 1.5 \leq \frac{P_l}{D_{ot}} \leq 6.0, 1.0 \leq \frac{D_f}{D_{ot}} \leq 1.5, 0.5 \leq \frac{P_f - \delta_f}{P_f} \leq 1.0$, and $1,000 \leq Re_{D_h} \leq 10,000$.

Figure 2.6 provides a comparison between the Colburn and friction factors obtained using Eqs. 2.14 and 2.15, and those obtained experimentally and using CFD (BT1-BT13 and CPF1-CPF13). The average and maximum deviation between the correlations and data are 2.7% and 12% for Colburn factor, and 5.7% and 25.4% for friction factor. Eqs. 2.14 and 2.15 estimate 100% of the Colburn and 95% of the friction factor data within ±15%.

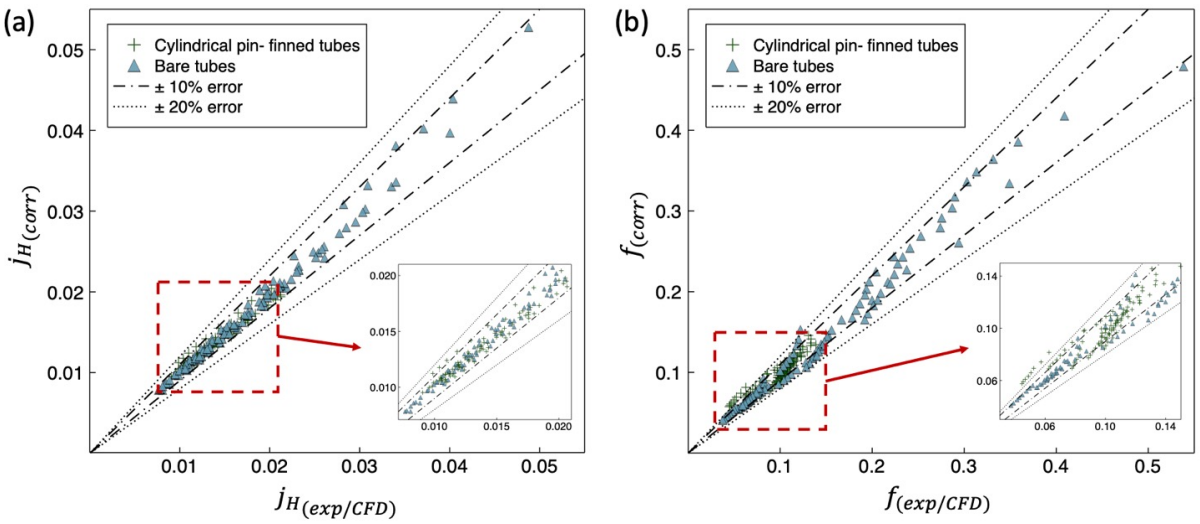

Figure 2.6: Experimental and CFD data for (a) Colburn and (b) friction factor plotted against the correlated values from Eqs. 2.14 and 2.15 for flow over bare and cylindrical pin-finned tube banks.

2.3.4 Correlation validation

CFD simulations were performed using ANSYS Fluent 2021 R2 to validate developed correlations for Colburn and friction factor. The domain used, mesh developed, and the boundary conditions applied in the CFD simulations are shown in Fig. 2.7. The velocity at the inlet of the tube bundle is varied to achieve a range of external flow Reynolds numbers. A hex mesh is selected and the number of tube rows, entrance length, and exit length are selected based on the study conducted by Zhou and Catton [80]. The interface between the tubes and the working fluid is coupled.

The tube material used is steel, and the NIST real gas model is used for thermophysical properties of the working fluid. The working fluid is assumed to be three-dimensional, steady-state, and turbulent. The k-ω shear-stress transport (k-ω SST) model with automatic wall

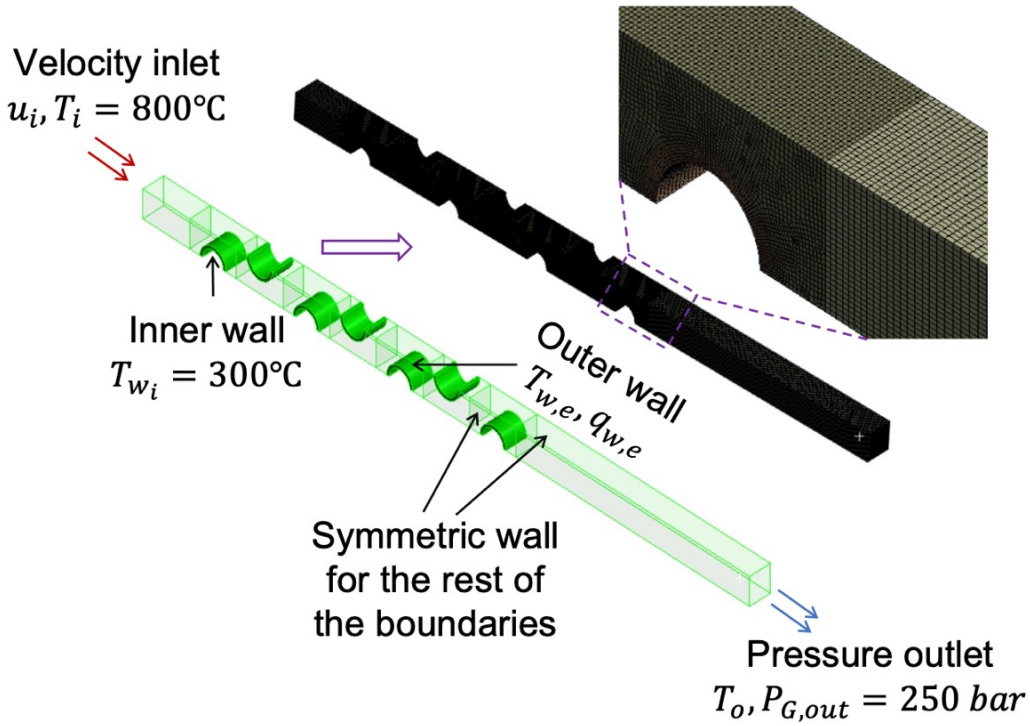

Figure 2.7: Schematic of the domain, mesh, and boundary conditions utilized in the CFD model for correlation validation.

function treatment is used to predict heat transfer and turbulent flow along the tube bundle. A pressure-based coupled algorithm is used, and the RMS type residual criteria for solution convergence is set to 10^{-5} for energy and momentum balances.

The two metrics utilized for comparison are heat transfer coefficient and tube bundle pressure drop. The heat transfer coefficient is calculated from ANSYS Fluent as

$$\overline{h_{tb}} = \frac{\overline{q_{w,e}}}{\Delta T_{LMTD}} \tag{2.16}$$

where $\Delta T_{LMTD} = \frac{\left[\left(T_{tb,in} - \overline{T_{w,e}}\right) - \left(T_{tb,out} - \overline{T_{w,e}}\right)\right]}{ln\left[\frac{\left(T_{tb,in} - \overline{T_{w,e}}\right)}{\left(T_{tb,out} - \overline{T_{w,e}}\right)}\right]}$, $\overline{q_{w,e}}$ is the heat flux at the tube-fluid interface, tb, in and tb, out are locations at the inlet and outlet of the tube bundle respectively, and $\overline{h_{tb}}$ is the heat transfer coefficient of the flow over the tube bundle. Pressure drop of the flow

over the tube bundle is obtained from ANSYS Fluent by taking the difference between the pressures at the inlet and outlet of the tube bundle. The heat transfer coefficient from the Colburn factor correlation is calculated as

$$h_{corr} = j_H Re_{D_h} Pr^{0.33} \frac{\kappa}{D_h} \tag{2.17}$$

where κ and Pr are evaluated at the mean fluid temperature and pressure. Pressure drop is evaluated from the friction factor correlation as

$$\Delta P_{corr} = 2\rho u_{max}^2 f \frac{L_y}{D_h} \tag{2.18}$$

where L_y is the length of fluid flow across the tube bundle and ρ is evaluated at the mean fluid temperature and pressure.

A mesh refinement and grid independence study was performed on a case discussed later with $Re_{D_h} = 6,000$, $\frac{P_t}{D_{ot}} = 1.8$, $\frac{P_l}{D_{ot}} = 3.6$, $D_{ot} = 6.35$, and sCO_2 as the working fluid. The heat transfer coefficient and pressure drop of the flow is plotted as a function of the number of elements in Fig. 2.8. Based on the trend observed in the plot, the mesh with an element size of 0.1 mm was employed for all CFD simulations below.

To verify and validate the CFD model utilized in this section, simulations were carried out for the BT1 geometry utilized by Kays and London [64] with $D_{ot} = 6.35\ mm$, $P_t = 9.53\ mm$, and $P_l = 15.88\ mm$. By using air as the working fluid, seven simulations were performed by varying the inlet velocity, corresponding to a Reynolds number range from 2,000 to 8,000. Figure 2.9 provides a comparison of the heat transfer coefficient and pressure drop obtained from CFD and experiments for the BT1 case. The average deviation of both the heat

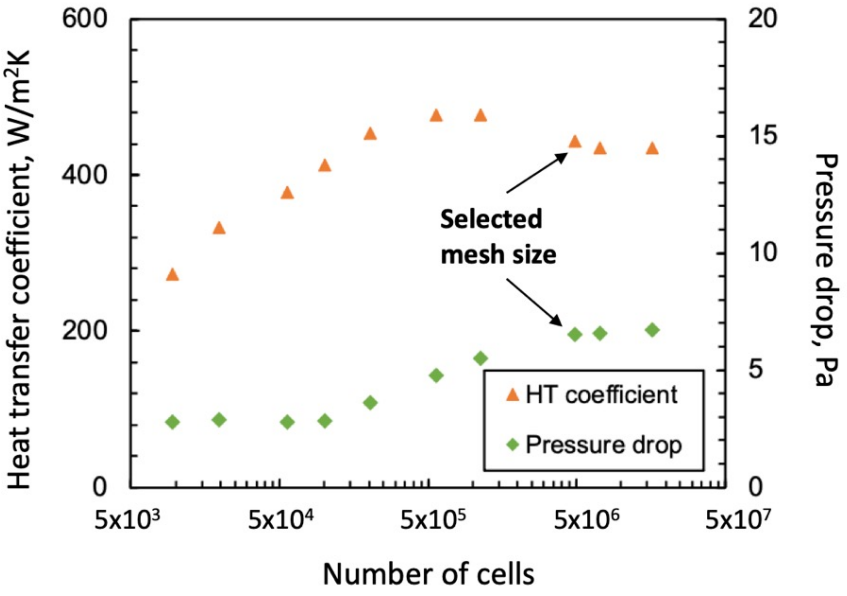

Figure 2.8: Grid size refinement study: comparison of the heat transfer coefficient and pressure drop of the external flow as a function of the number of cells in the domain.

transfer coefficient and pressure drop between CFD and experimental data is less than 10% and therefore demonstrates the accuracy of the developed CFD model.

To further demonstrate the accuracy and versatility of the developed correlations to systems with sCO_2 and air at extreme temperatures and pressures, another set of CFD simulations were conducted. With $D_{ot} = 6.35\ mm, P_t = 11.43\ mm$, and $P_l = 22.86\ mm$, five simulations each for sCO_2 and air as working fluids were performed at different inlet velocities to vary the Reynolds number from 2,000 to 11,000. Figure 2.10 provides a comparison of the heat transfer coefficient and pressure drop obtained from CFD and the unified correlations for sCO_2 and air as the working fluids. The developed correlations predict the heat transfer coefficient and pressure drop with approx. 10% and 5% deviation respectively. This agreement further demonstrates the ability to model thermohydraulic performance of tube

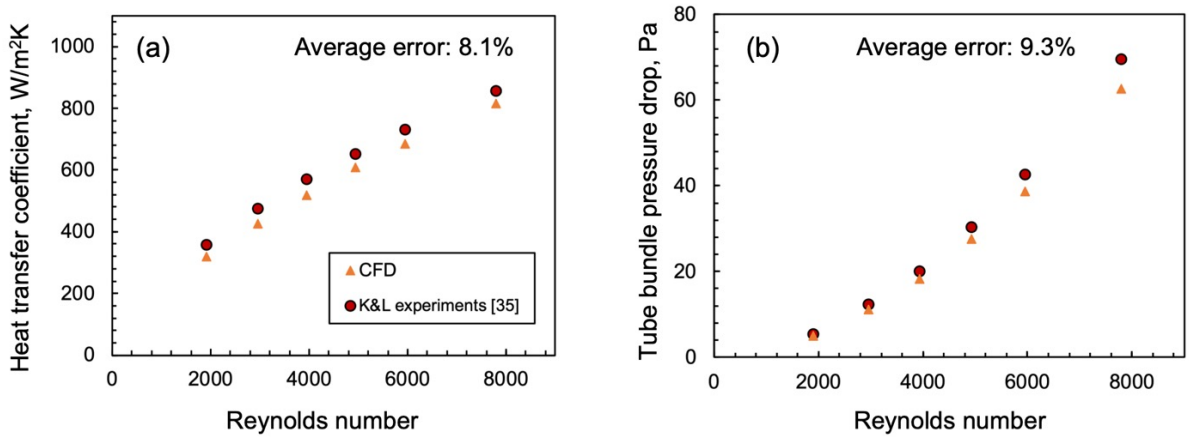

Figure 2.9: Comparison between (a) heat transfer coefficient and (b) pressure drop of external flow obtained from Kays and London [64] experimental data and CFD simulations for the BT1 case to validate the developed CFD model.

bundle geometries outside of the training datasets but within the applicable non-dimensional parameter ranges.

2.3.5 Discussion

A summary of the average and maximum deviations of the three developed correlations with existing experimental and CFD data is provided in Table 2.5. The maximum errors for cases with specific geometries are slightly lower when compared to the unified correlation applicable to bare, disc-finned, and cylindrical pin-finned tube bank geometries.

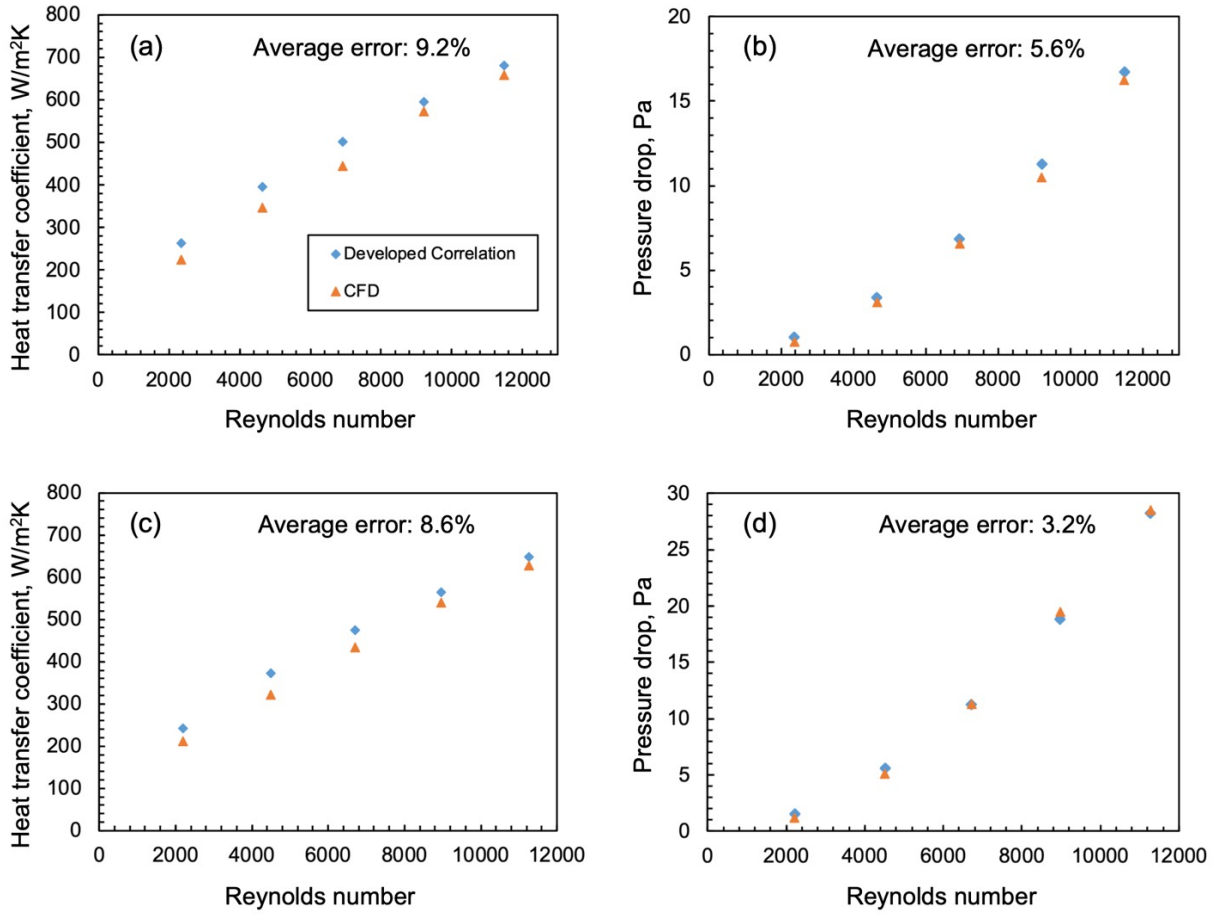

Figure 2.10: Comparison of (a and c) heat transfer coefficient and (b and d) pressure drop obtained from the developed correlations and the CFD model using (a and b) sCO_2 and (c and d) air as working fluids to validate the developed correlations.

Table 2.5: Average and maximum deviations of the three sets of Colburn and friction factor correlations from experimental and CFD data [64, 74].

	Avg. error (j_H)	Max. error (j_H)	Avg. error (f)	Max. error (f)
BT, DF, and CPF tube bank	6.5%	33.9%	8.3%	34.2%

	Avg. error (j_H)	Max. error (j_H)	Avg. error (f)	Max. error (f)
BT and DF tube bank	7.5%	27.4%	6.6%	25.1%
BT and CPF tube bank	2.7%	12%	5.7%	25.4%

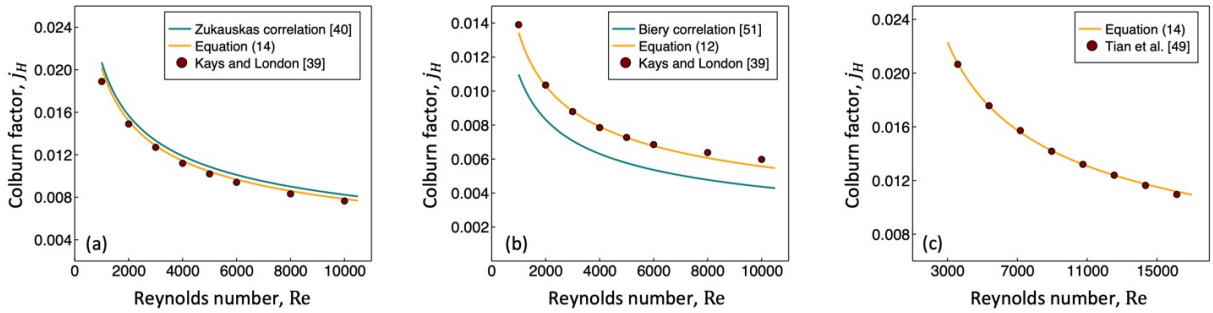

Figure 2.11: Comparison between the Colburn factors obtained from (a) Kays and London [64] experimental data, the Zukauskas correlation [65] for BT1, and Eq. 2.14, (b) Kays and London [64] experimental data, the Biery correlation [76], and Eq. 2.12 for DF3, and (c) Tian et al. [74] CFD data and Eq. 2.14 for CPF7.

The predictive value of Eqs. 2.10-2.15 is better than the Zukauskas and Biery correlations. Figure 2.11 provides a comparison of the predictability of Colburn factor for BT1, DF3, and CPF7 with existing correlations, and experimental and CFD data. Equation 2.14 predicts the Colburn factor of BT1 to within an average deviation of 2.8% from the experimental data [64], while the Zukauskas correlation [65] predicts the same with an average error of 7%. Equation 2.12 predicts the Colburn factor of DF3 to within an average deviation of 1.6%

from the experimental data [64], while the Biery correlation [76] predicts the same with an average error of 21%. Equation 2.14 predicts the CFD data [74] (Colburn factor) of CPF7 with an average error of 2%. In general, the developed friction factor correlations fill the gap in the literature by providing a method to quantify the hydraulic performance of flow over tube banks. In addition, the Colburn and friction factor correlations are more general (applicable to bare, disc-finned, and cylindrical pin-finned tube banks) and have improved accuracy.

2.4 Conclusion

This chapter reports comprehensive correlations for shell-side flow over various finned and bare tube bank geometries in STHXs. Using expansive data sets, three sets of Colburn and friction factor correlations are developed – unified, disc-finned, and cylindrical pin-finned correlations. These correlations assume a power-law form and include hydraulic diameter and newly introduced length scale ratios compatible with various tube bank geometries. The correlations developed in this paper have improved the predictive accuracy of existing bare tube correlations by around 5%, disc-fin correlations by around 20%, and has provided a quantification methodology for cylindrical pin-fin tube banks. All developed correlations can be implemented to conduct modeling studies for compact STHXs such as sCO_2 HXs operating at extreme conditions [81, 82]. These correlations enable highly accurate performance evaluation for HXs with various geometries and a design basis for modeling highly efficient thermal cycles.

Chapter 3: Shell-and-tube heat exchanger numerical model

3.1 Introduction

Thermohydraulic performance predictions of the heat exchangers can be achieved by experimental testing. However, accurate measurement of thermohydraulic performance is extremely complicated, and experimental testing is neither cost nor time efficient [83]. Numerical modeling of the heat exchangers has become an accurate and time-efficient method to obtain detailed temperature, velocity, and pressure fields in a given design. Modeling the entire STHX by representing the tubes in detail using Computational Fluid Dynamics (CFD) is computationally expensive. The concept of distributed resistance has been introduced, and early work was carried out, by Patankar and Spalding [84], Butterworth [85], Sha [86], and Sha et al. [87]. Using this approach, tube bundle details are eliminated, and the model is simplified based on volumetric porosity and surface permeability. Although this approach significantly reduces computation time and provides accurate solutions, hours are typically required to obtain the solution.

Correlation-based modeling is an approach used to design and predict thermohydraulic performance of heat exchangers. Correlation-based approaches are computationally efficient but require highly accurate correlations for thermal and hydraulic performance in order to accurately predict heat exchanger performance. The Kern method [88] and the Bell-Delaware method [89] are commonly used correlation-based approaches. The Kern method

A large portion of this chapter created the paper by A. B. Krishna, K. Jin, P. S. Ayyaswamy, I. Catton, and T. S. Fisher, titled "Modeling of supercritical CO_2 shell-and-tube heat exchangers under extreme conditions. Part 2: Heat exchanger model" published in ASME Journal of Heat Transfer. DOI: 10.1115/1.4053511

is only suitable for initial sizing of the STHX, as this method provides a conservative estimate of performance. The Bell-Delaware method provides an accurate estimation of the shell-side performance but does not have the capability to provide a detailed description of temperature and flow fields within an STHX.

Advances in the modeling of multi-physics transport through heterogeneous media with Volume Averaging Theory (VAT) [90] have allowed engineers to simulate flow and heat transfer in thermal devices in mere seconds on a laptop, in comparison to the many hours (or longer) required for CFD. Volume averaging is a method of abstracting the geometry for computation of complex problems and follows a porous medium approach where the volume occupied by the fluids and the solid are represented in terms of their volume fractions. The flow and temperature fields are described non-locally, and the topology of the problem can be embedded into the governing equations to allow for the complete treatment of conjugate effects [91–93]. Most solutions of the governing equations have been obtained through numerical methods such as finite element and finite difference schemes [94, 95]. Closure must be obtained theoretically, numerically or experimentally for the transport equations in order to account completely for geometric complexities [96, 97]. In Chapter 2, closure was demonstrated, and correlations for friction and Colburn factor were developed. By closing the transport equations, simulations can be executed in express time, and this advancement enables accurate and efficient performance prediction of thermal devices [98], as well as optimization routines that span broad parameter spaces efficiently.

Previous studies provide modeling approaches that are either less accurate in performance predictions or resource-intensive and time-consuming. A simultaneously efficient and accurate methodology is essential to perform feasible multiparameter optimization studies.

The objective of this study is to develop and demonstrate a computationally efficient and accurate numerical model for performance predictions of STHXs. We utilize highly accurate correlations for thermohydraulic performance estimation detailed in Chapter 2 and abstract the geometry of the STHX using the concept of volume averaging. Our approach combines the advantages of correlation-based numerical modeling and the distributed resistance porous media approach to provide a highly accurate and time-efficient modeling methodology for STHXs.

3.2 Methodolgy

In this section, the methodology used to define the STHX geometry and governing equations for the model development are introduced. The model algorithm is reported in the latter half of this section. The STHX modeled in this study is shown in Fig. 3.1.

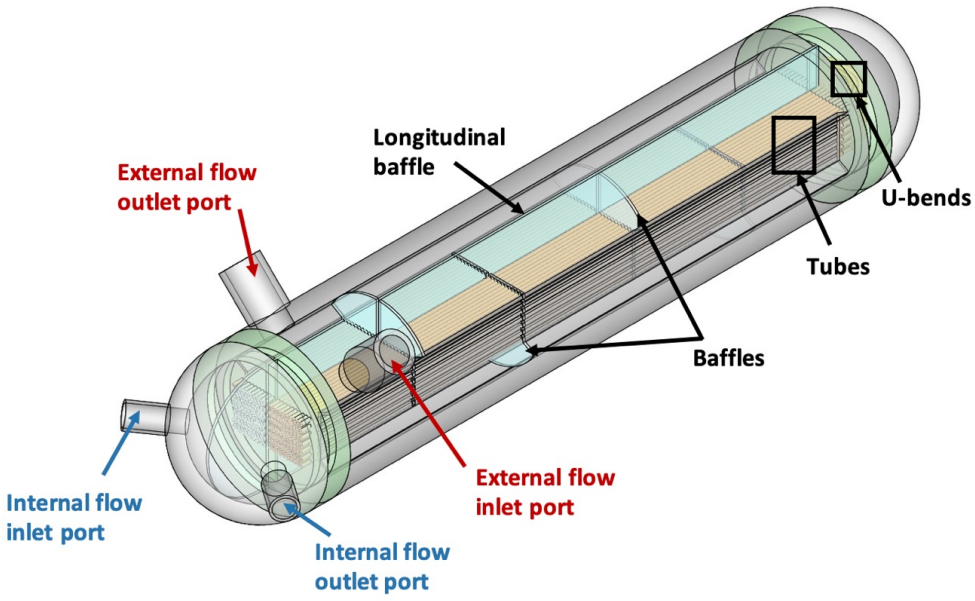

Figure 3.1: Isometric view of the STHX.

3.2.1 Definition of geometric parameters

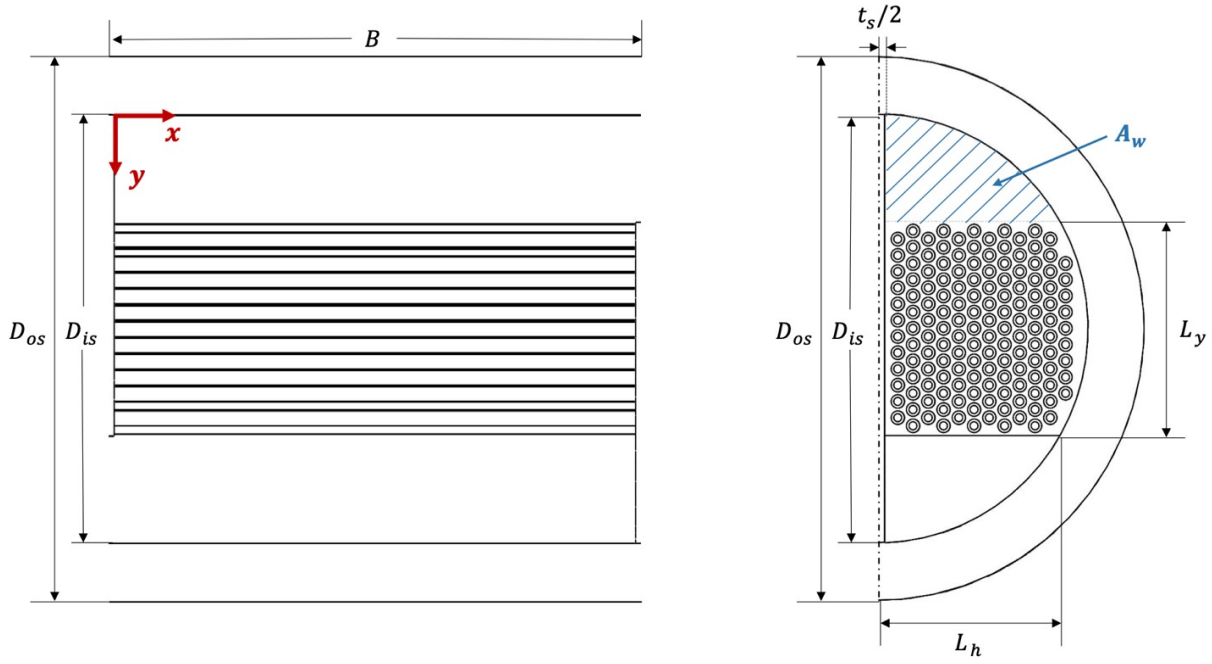

Figure 3.2: Front view (left) and side view (right) of a unit cell of the STHX.

To perform temperature and flow field calculations using volume averaging, a unit cell is defined as shown in Fig. 3.2. The temperature and flow fields through the STHX can be obtained by serially repeating the unit cell over the volume of the STHX and solving for each unit cell individually. Abstraction of the unit cell geometry is carried out by defining three key parameters – volume fraction, ϕ, specific wetted surface area, S_w, and VAT hydraulic diameter, D_{VAT}. These parameters are given by:

$$\phi_i = \frac{\text{Volume occupied by component } i \text{ in the unit cell}}{\text{Total volume of the unit cell}} \tag{3.1}$$

$$S_{w_j} = \frac{\text{Tube area wetted by fluid } j + \text{Fin area wetted by fluid } j}{\text{Total volume of the unit cell}} \tag{3.2}$$

$$D_{VAT_j} = \frac{4\phi_j}{S_{w_j}} \tag{3.3}$$

where component i is the internal fluid stream, external fluid stream, or the solid material, and fluid j is the internal or external fluid stream. As explained in Chapter 2, Reynolds number is a measure of the ratio between inertial and viscous forces in the flow, as well as its turbulent character. Reynolds number is calculated as

$$Re_{D_h} = \frac{u_{max} D_h}{\nu} \tag{3.4}$$

$$Re_{VAT} = \frac{u_{avg} D_{VAT}}{\nu} \tag{3.5}$$

where u_{max} is the maximum velocity of flow located at the minimum free flow area, A_{min}, and u_{avg} is the average velocity located at the frontal area, A_{fr}.

Modified specific wetted surface area, S_{wm}, is defined using the concept of fin efficiency in order to account for the actual wetted area for heat transfer. The parameter is given by

$$S_{wm_j} = \frac{\text{Tube area wetted by fluid } j + (\text{Fin area wetted by fluid } j \times \eta_f)}{\text{Total volume of the unit cell}} \tag{3.6}$$

where fluid j is the internal or external fluid stream and η_f is the fin efficiency defined below.

$$\eta_f = \frac{q_f}{q_{f,max}} \tag{3.7}$$

Disc fins and cylindrical pin-fins are the fin geometries under consideration. The efficiencies of these types of fins are given by [99]:

Disc fins:

$$\eta_{DF} = C_1 \frac{K_1(mr_{ot})\, I_1(mr_{fc}) - I_1(mr_{ot})\, K_1(mr_{fc})}{I_0(mr_{ot})\, K_1(mr_{fc}) + K_0(mr_{ot})\, I_1(mr_{fc})} \tag{3.8}$$

where $C_1 = \frac{2r_{ot}}{m(r_{fc}^2 - r_{ot}^2)}, r_{fc} = (D_f/2) + (\delta_f/2), r_{ot} = D_{ot}/2$, and $m = \sqrt{\frac{2h_1}{\kappa_s \delta_f}}$.

Cylindrical pin-fins:

$$\eta_{CPF} = \frac{\tanh(mL_c)}{mL_c} \tag{3.9}$$

where $L_c = \left(\frac{D_f - D_{ot}}{2}\right) + \left(\frac{\delta_f}{4}\right)$ and $m = \sqrt{\frac{4h_1}{\kappa_s \delta_f}}$. The number of tubes in the bundle is high, and they are packed closely together. The high density of solid phase in the bundle causes majority of the flow resistance and heat transfer to occur in the bundle of the tubes and not due to the presence of the baffles. Therefore, we neglect the effect of the baffles in the evaluation of the external flow characteristics. By making use of the unit cell concept, the volume fraction, specific wetted surface area, and the modified specific wetted surface area for the external flow stream of the various tube bundle configurations is defined as:

Bare tube bundle:

$$\phi_{1,BT} = 1 - \frac{N_t \pi D_{ot}^2 B}{4V_T} \tag{3.10}$$

$$S_{w1,BT} = \frac{N_t \pi D_{ot} B}{V_T} \tag{3.11}$$

$$S_{wm1,BT} = S_{w1,BT} \tag{3.12}$$

Disc-finned tube bundle:

$$\phi_{1,DF} = 1 - \frac{N_t}{4V_T}\left[\pi D_{ot}^2 B + N_f \pi \left(D_f^2 - D_{ot}^2\right) \delta_f\right] \tag{3.13}$$

$$S_{w1,DF} = \frac{N_t N_f}{2V_T}\left[2\pi D_{ot}\left(P_f - \delta_f\right) + 2\pi D_f \delta_f + \pi\left(D_f^2 - D_{ot}^2\right)\right] \tag{3.14}$$

$$S_{wm1,DF} = \frac{N_t N_f}{2V_T}\left[2\pi D_{ot}\left(P_f - \delta_f\right) + 2\pi D_f \delta_f \eta_f + \pi\left(D_f^2 - D_{ot}^2\right)\eta_f\right] \tag{3.15}$$

Cylindrical pin-finned tube bundle:

$$\phi_{1,CPF} = 1 - \frac{N_t}{8V_T}\left[2\pi D_{ot}^2 B + N_f N_{af} \pi \delta_f^2 \left(D_f - D_{ot}\right)\right] \tag{3.16}$$

$$S_{w1,CPF} = \frac{N_t N_f}{2V_T}\left[2\pi D_{ot} P_f + N_{af}\pi\delta_f\left(D_f - D_{ot}\right)\right] \tag{3.17}$$

$$S_{wm1,CPF} = \frac{N_t N_f}{2V_T}\left[2\pi D_{ot} P_f + N_{af}\pi\delta_f\left(D_f - D_{ot}\right)\eta_f\right] \tag{3.18}$$

All geometric parameters in the equations above are shown in Fig. 2.2 and Fig. 3.2. Because no internal inserts/augmentations exist, the internal flow stream parameters are the same for all tube bundle configurations under consideration. These parameters are given by

$$\phi_2 = \frac{N_t \pi D_{it}^2 B}{4V_T} \tag{3.19}$$

$$S_{w2} = \frac{N_t \pi D_{it} B}{V_T} \tag{3.20}$$

$$S_{wm2} = S_{w2} \tag{3.21}$$

Total volume of the unit cell:

$$V_T = \frac{\tan^{-1}\left(\frac{L_y}{2L_h}\right)\pi D_{is}^2 B}{720} + \frac{L_h L_y B}{2} - t_s L_y B \tag{3.22}$$

The volume fraction of the solid is defined as a function of the volume fraction of the fluid streams.

$$\phi_s = 1 - (\phi_1 + \phi_2) \tag{3.23}$$

3.2.2 Governing equations

The following assumptions are made for the derivation of the governing equations:

1. The working fluid is steady, incompressible, and Newtonian.
2. Conduction in the fluid is negligible since the flow has high Peclet number.
3. Solid is discontinuous in the y-direction, and the thermal conductivity of the solid material (Haynes 282) is approximately 200× higher than that of the working fluid (CO_2). Therefore, solid conduction is neglected in the y-direction.

The resulting equations for continuity and momentum for both fluid streams are given below.

Continuity equation:

$$\phi_j \left(\frac{\partial \overline{u_j}}{\partial x} + \frac{\partial \overline{v_j}}{\partial y} + \frac{\partial \overline{w_j}}{\partial z} \right) = 0 \tag{3.24}$$

where $j = 1$ for external flow and $j = 2$ for internal flow

External flow momentum equation:

$$\phi_1 \frac{\partial \overline{P}}{\partial y} = \frac{1}{2} \rho_1 f_1 S_{w1} \overline{v_1^2} \tag{3.25}$$

Internal flow momentum equation:

$$\phi_2 \frac{\partial \overline{P}}{\partial x} = \frac{1}{2} \rho_2 f_2 S_{w2} \overline{u_2^2} \tag{3.26}$$

where f_1 and f_2 and the friction factors for the external and internal fluid streams respectively, and v and u are the velocities in the y- and x-directions as shown in Fig. 3.2.

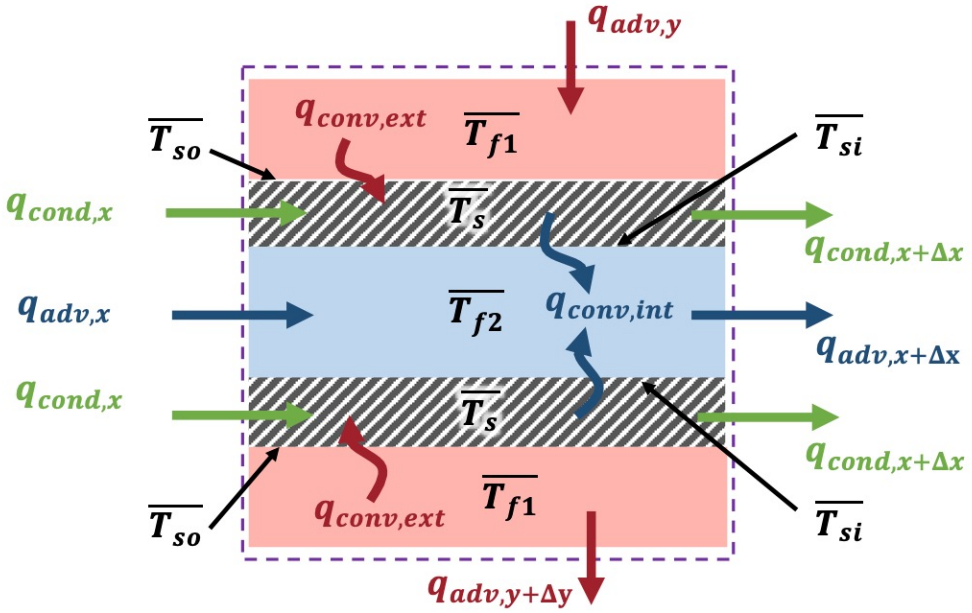

Figure 3.3: Control volume used to derive the energy equations.

The energy equations for external and internal fluid streams, and the solid phase are obtained by performing an energy balance on the control volume in Fig. 3.3 and are given by:

Fluid-phase energy equation (external flow):

$$\overline{(\rho C_p)}_1 \phi_1 \bar{v}_1 \frac{\partial T_1}{\partial y} = h_1 S_{wm1} \left(\overline{T_{so}} - \overline{T_1}\right) \tag{3.27}$$

Fluid-phase energy equation (internal flow):

$$\overline{(\rho C_p)}_2 \phi_2 \bar{u}_2 \frac{\partial T_2}{\partial x} = h_2 S_{wm2} \left(\overline{T_{si}} - \overline{T_2}\right) \tag{3.28}$$

Solid-phase energy equation:

$$\phi_s \overline{\kappa_s} \frac{\partial^2 \overline{T_s}}{\partial x^2} = h_1 S_{wm1} \left(\overline{T_{so}} - \overline{T_1} \right) + h_2 S_{wm2} \left(\overline{T_{si}} - \overline{T_2} \right) \tag{3.29}$$

where h_1 and h_2 are the heat transfer coefficients of the external and internal fluid streams respectively.

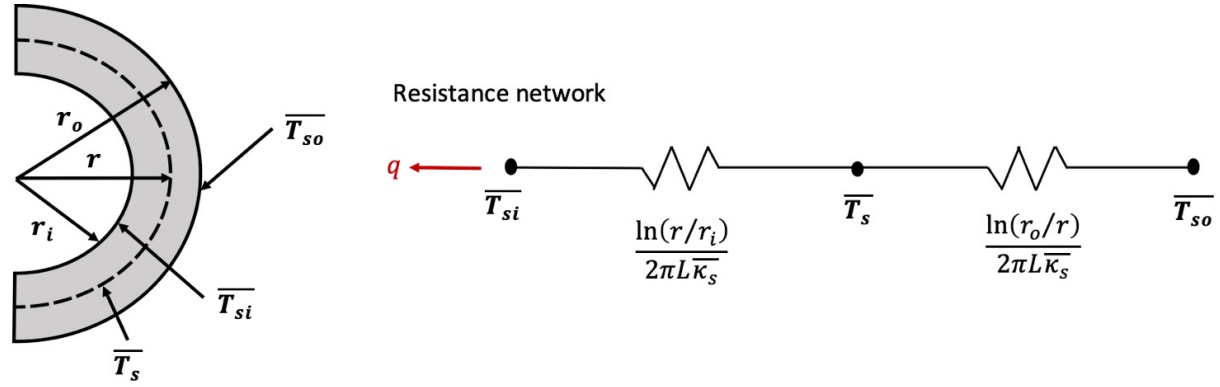

Figure 3.4: Cross-section of a half-tube (left) and resistance network to define the tube wall temperatures (right).

Bulk solid temperature, $\overline{T_s}$, is defined by means of a resistance network as shown in Fig. 3.4 and is given by

$$\overline{T_s} = \frac{ln(r/r_i)\overline{T_{so}} + ln(r_o/r)\overline{T_{si}}}{ln(r_o r_i/r^2)} \tag{3.30}$$

where $r = \frac{r_i + r_o}{2}$.

3.2.3 Flow correlations and correction factors

Closure is required to solve for the governing equations. Correlations for the friction factor and heat transfer coefficient need to be obtained for both the external and internal flow streams.

External flow

Chapter 2 reports the development of Colburn and friction factor correlations for the external flow with various tube bundle configurations. The unified form of the correlations applicable to bare, disc-finned, and cylindrical pin-finned tube banks transformed to the VAT length scale is given below.

Colburn factor:

$$j_{H_{1,VAT}} = 0.47 \left(\frac{D_h}{D_E}\right)^{0.53} \left(\frac{P_t}{D_{ot}}\right)^{-0.21} \left(\frac{P_l}{D_{ot}}\right)^{-0.19} \left(\frac{D_f}{D_{ot}}\right)^{0.12} \left(\frac{P_f - \delta_f}{P_f}\right)^{-0.38} Re_{D_{h_1}}^{-0.40} \quad (3.31)$$

Friction factor:

$$\begin{aligned} f_{1,VAT} =& 4 \times 0.54 \times Re_{D_{h_1}}^{-0.23} \left(\frac{D_h}{D_E}\right)^{0.62} \left(\frac{P_t}{D_{ot}}\right)^{0.40} \left(\frac{P_l}{D_{ot}}\right)^{-0.20} \\ & \times \left(\frac{D_f}{D_{ot}}\right)^{-0.45} \left(\frac{P_f - \delta_f}{P_f}\right)^{-0.23} \left(\frac{D_{VAT}}{D_{h1}}\right)^{3} \end{aligned} \quad (3.32)$$

Heat transfer coefficient is obtained using the following relation:

$$h_1 = j_{H1} Re_{D_{h_1}} Pr^{1/3} \frac{\kappa_1}{D_h} \quad (3.33)$$

The total pressure drop in each unit cell for external flow is a summation of the pressure drop in the tube bundle and the pressure drop in the turning region.

$$\Delta P_1 = \Delta P_{1,tbc} + \Delta P_{1,turn} \quad (3.34)$$

Pressure drop in the tube bundle is defined as

$$\Delta P_{1,tb} = \frac{1}{2} \rho_1 f_{1,VAT} \overline{v_1^2} \frac{L_y}{D_{VAT_1}} \quad (3.35)$$

Pressure drop in the turning region is calculated using the correlation developed by Bell [29].

$$\Delta P_{1,turn} = \frac{\dot{m}_1^2}{\rho_1 N_{tc} A_c A_w} \zeta_l \tag{3.36}$$

where $\dot{m}_1$ is the external fluid mass flow rate, ζ_l is the correction for baffle leakage effects, and A_w is the cross-section area of the window region as shown in Fig. 3.2.

The Colburn and friction factor correlations assume ideal perpendicular flow over the tube bundle. In an STHX, the external flow will experience bypass, leakage, and other secondary effects that influence the heat transfer coefficient and pressure drop. We employ correction factors developed by Bell [89] to account for these effects. The modified equations take the form:

$$h_{1c} = h_1 J_c J_l J_b J_s \tag{3.37}$$

where J_c is the correction for baffle configuration, J_l is the correction for baffle leakage effects, J_b is the correction for bundle bypass effects, and J_s is the correction for larger baffle spacing at the inlet and outlet unit cells.

The corrected external flow pressure drop is

$$\Delta P_{1,tbc} = \Delta P_{1,tb} \zeta_l \zeta_b \zeta_s \tag{3.38}$$

where ζ_l is the correction for baffle leakage effects, ζ_b is the correction for bundle bypass effects, and ζ_s is the correction for larger baffle spacing at the inlet and outlet unit cells.

Internal flow

In the present study, U-tubes are used in the STHX. Estimation of the heat transfer coefficient for internal flow uses the Gnielinski correlation [58] (valid for $3,000 \leq Re_{D_{it}} \leq 5 \times 10^6$ and $0.5 \leq Pr \leq 2,000$).

$$h_2 = \frac{(f_2/8)\left(Re_{D_{it}} - 1000\right) Pr}{1 + 12.7\left(f_2/8\right)^{0.5}\left(Pr^{0.67} - 1\right)} \frac{\kappa_2}{D_{it}} \tag{3.39}$$

The internal flow friction factor is obtained using Petukhov formula [57] (valid for $3,000 \leq Re_{D_{it}} \leq 5 \times 10^6$) and is given by

$$f_2 = \left(0.790 ln Re_{D_{it}} - 1.64\right)^{-2} \tag{3.40}$$

For flow in the laminar regime, the Nusselt number is $Nu_2 = 4.36$, and the friction factor is $f_2 = 64/Re_{D_{h_2}}$. The total pressure drop for internal flow in the STHX is the summation of friction losses in the straight region, contraction and expansion losses as the flow enters and leaves the tubes, and pressure losses in the u-bends of the tube.

$$\Delta P_2 = \Delta P_{2,ce} + \Delta P_{2,ub} + \sum_{1}^{2N} \Delta P_{2,st} \tag{3.41}$$

where N is the total number of unit cells. Internal pressure drop in the straight region, $\Delta P_{2,st}$, due to friction losses in one unit cell is

$$\Delta P_{2,st} = \frac{1}{2}\rho_2 f_2 \overline{u_2^2} \frac{B}{D_{it}} \tag{3.42}$$

Contraction and expansion losses, $\Delta P_{2,ce}$, are computed using correlations developed by Kays and London [64]:

$$\Delta P_{2,ce} = \frac{1}{2}\left(K_c + K_e\right)\frac{G_2^2}{\overline{\rho_2}} \tag{3.43}$$

where K_c and K_e are contraction and expansion coefficients, and G_2 is the mass velocity of internal flow. Pressure losses in the u-bends, $\Delta P_{2,ub}$, are calculated using the following correlation [100]:

$$\Delta P_{2,ub} = \frac{1}{2}\rho_2 u_2^2\left(K_b + f_2\frac{\pi R_b}{D_{it}}\right) \tag{3.44}$$

where K_b is the bend loss coefficient and R_b is the bend radius.

The performance of a heat exchanger can be quantified by its effectiveness, ϵ. The effectiveness of a heat exchanger is defined as the ratio of actual rate of heat transfer to the maximum possible heat transfer rate.

$$\epsilon = \frac{\text{Actual heat transfer}}{\text{Maximum possible heat transfer}} \tag{3.45}$$

3.2.4 STHX model algorithm

The indexing of the STHX is shown in Fig. 3.5. External fluid enters the STHX in unit cell '2N' and flows through to unit cell 'N+1' in a serpentine pattern. The fluid then turns to the second half of the STHX and follows a similar flow pattern until it reaches unit cell '1', where it exits the heat exchanger. The internal fluid enters the first unit cell and flows straight through to unit cell 'N'. The flow then encounters the U-bend and enters unit cell 'N+1' and flows through to unit cell '2N', where it exits the heat exchanger.

The transport equations given above form the basis for the computation of the temperature and flow field in the STHX. The computation is carried out with the help of a numerical

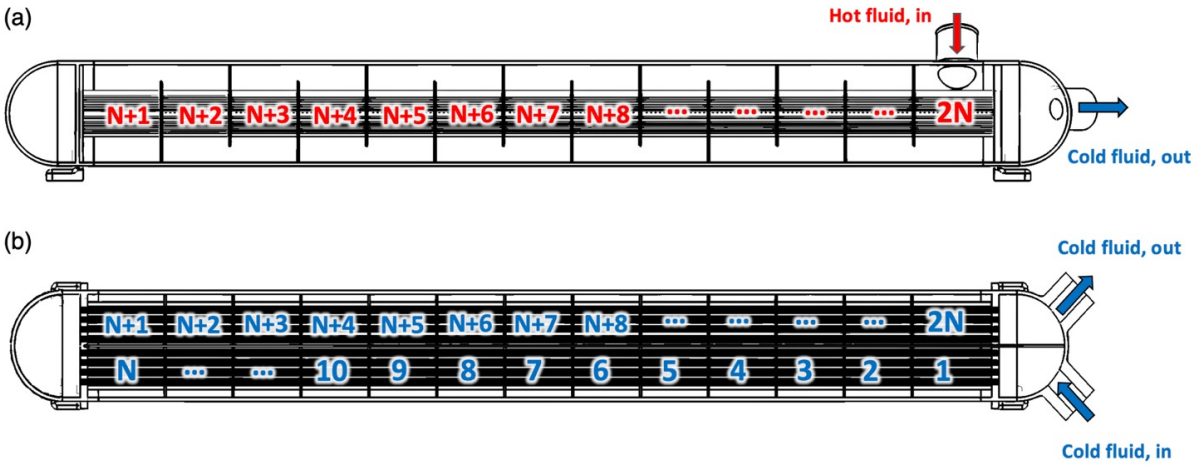

Figure 3.5: Indexing of the unit cells of the STHX. (a) Front section view and (b) top section view.

model developed using Julia programming language and attached in Appendix A [81]. The computer code solves for the temperature fields, velocity fields, and pressure drop of both streams by using the Gauss-Seidel iterative method. The discretized forms of the governing energy equations are given below.

External fluid energy equation:

$$\frac{\overline{(\rho C_p)}_1 \phi_1 \bar{u}_1 \left(T_{y+1} - T_y\right)}{\Delta \mathrm{y}} = h_1 S_{w1} \left(\overline{T_{so}} - \overline{T_1}\right) \tag{3.46}$$

Internal fluid energy equation:

$$\frac{\overline{(\rho C_p)}_2 \phi_2 \bar{u}_2 \left(T_{x+1} - T_x\right)}{\Delta \mathrm{x}} = h_2 S_{w2} \left(\overline{T_{si}} - \overline{T_2}\right) \tag{3.47}$$

Solid-phase energy equation:

$$\frac{\overline{\kappa_s} \left(\overline{T_{x-1}} - 2\overline{T_x} + \overline{T_{x+1}}\right)}{\Delta x^2} \phi_s = h_1 S_{w1} \left(\overline{T_{so}} - \overline{T_1}\right) + h_2 S_{w2} \left(\overline{T_{si}} - \overline{T_2}\right) \tag{3.48}$$

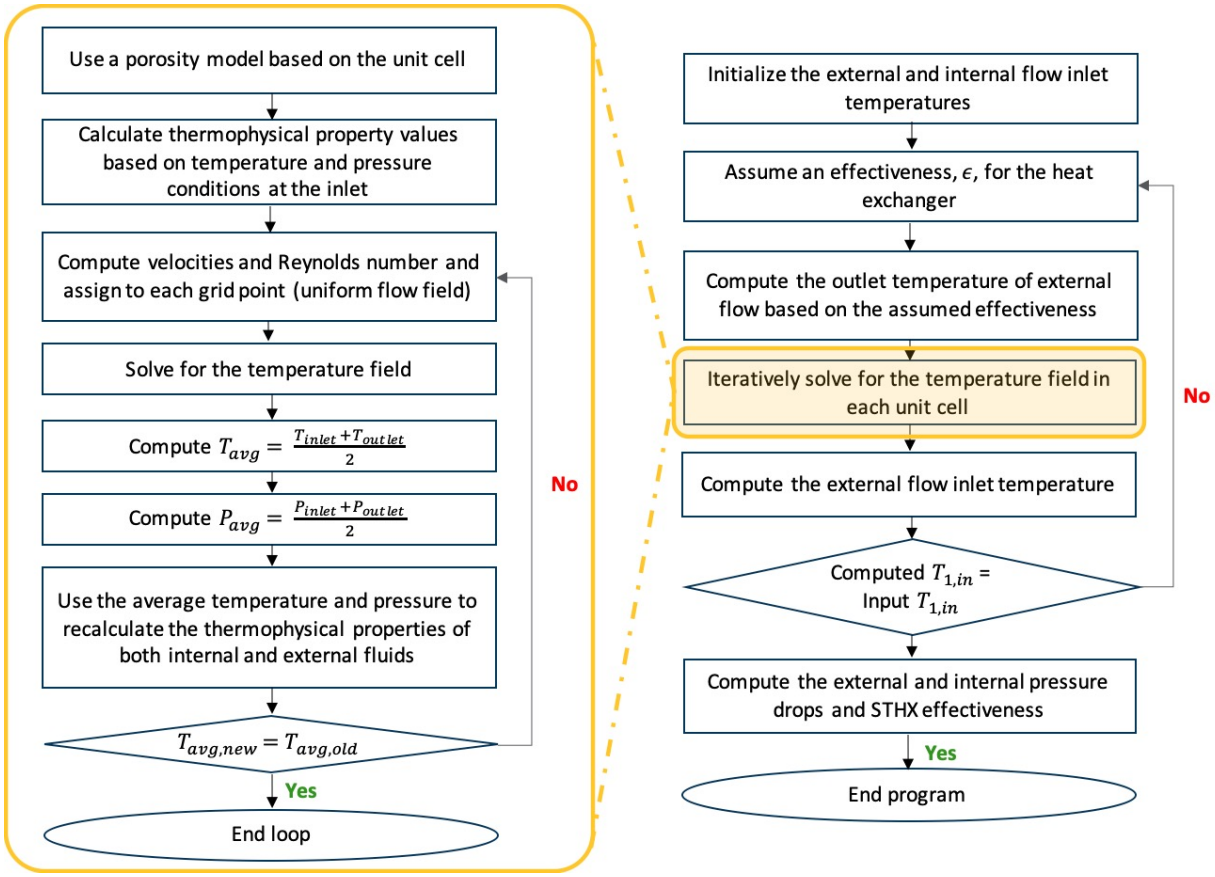

Figure 3.6: Algorithm of the computer code for the computation of temperature field, pressure field, flow field and effectiveness of the STHX.

The temperature and flow fields through the STHX are obtained by combining the unit cells serially. The temperature and velocity through each unit cell are solved completely before moving on to the next unit cell. The temperatures at the outlet on one unit cell are taken to be the inlet temperatures of the subsequent unit cell.

The algorithm for performance computation of the STHX is outlined in Fig. 3.6. With inlet temperatures of both streams as inputs, an initial effectiveness is assumed for the STHX, and the corresponding outlet temperature for the external flow stream is calculated. The temperature and pressure fields are then iteratively solved in each unit cell, and the predicted external inlet temperature is recorded. If the predicted external inlet temperature is lower

than the user-inputted temperature, an updated lower value of effectiveness is assumed (and vice-versa), and the process is repeated until a converged solution is obtained. The thermophysical properties of the fluid for both internal and external flow streams are updated during every iteration using CoolProp [101] based on the temperature and pressure at the location of the STHX. The thermal properties of the solid are obtained from the Haynes International website and calculated in the STHX code using a piecewise cubic Hermite interpolator [102]. The updating of effectiveness is carried out using a binary search algorithm to increase the efficiency of computation. The STHX model is very versatile and has the capability to handle effects of varying baffle cut, variable baffle spacing, and effect of sealing strips among other geometric and thermodynamic state inputs. Any fluid that is available in CoolProp's database can be chosen as a working fluid for the STHX [81]. The STHX numerical model can be used to predict the performance of STHXs whose tube bundle configurations lie within the applicability ranges of the correlations developed in Chapter 2 [103].

3.3 Results and Discussion

All STHX numerical model simulations in this study were performed on a computer with an Intel® Core i7-9750H processor at a clock rate of 2.60GHz. All CFD simulations in this study were performed on a computer with an Intel® Xeon® Gold 6230 processor at a clock rate of 2.10GHz.

3.3.1 Model Validation

CFD simulations were performed using ANSYS Fluent 2021 R2 to validate thermohydraulic performance predictions from the STHX numerical model. The domain used and the bound-

ary conditions applied in the CFD simulations are shown in Fig. 3.7. The mass flow rate at the external flow outlet of the unit cell is varied to achieve a range of external flow Reynolds numbers. The tube material used is Haynes 282, and the sCO_2 is the working fluid for both tube-side and shell-side flows. The interfaces between the tubes and the working fluids are coupled, and a NIST real gas model is used for thermophysical properties of the working fluid. The working fluid is assumed to be three-dimensional, steady-state, and turbulent. The k-ω shear-stress transport (k-ω SST) model with automatic wall function treatment is used to predict heat transfer and turbulent flow along the tube bundle and inside tubes. A pressure-based coupled algorithm is used, and the RMS type residual criteria for solution convergence is set to 10^{-5} for energy and momentum balances.

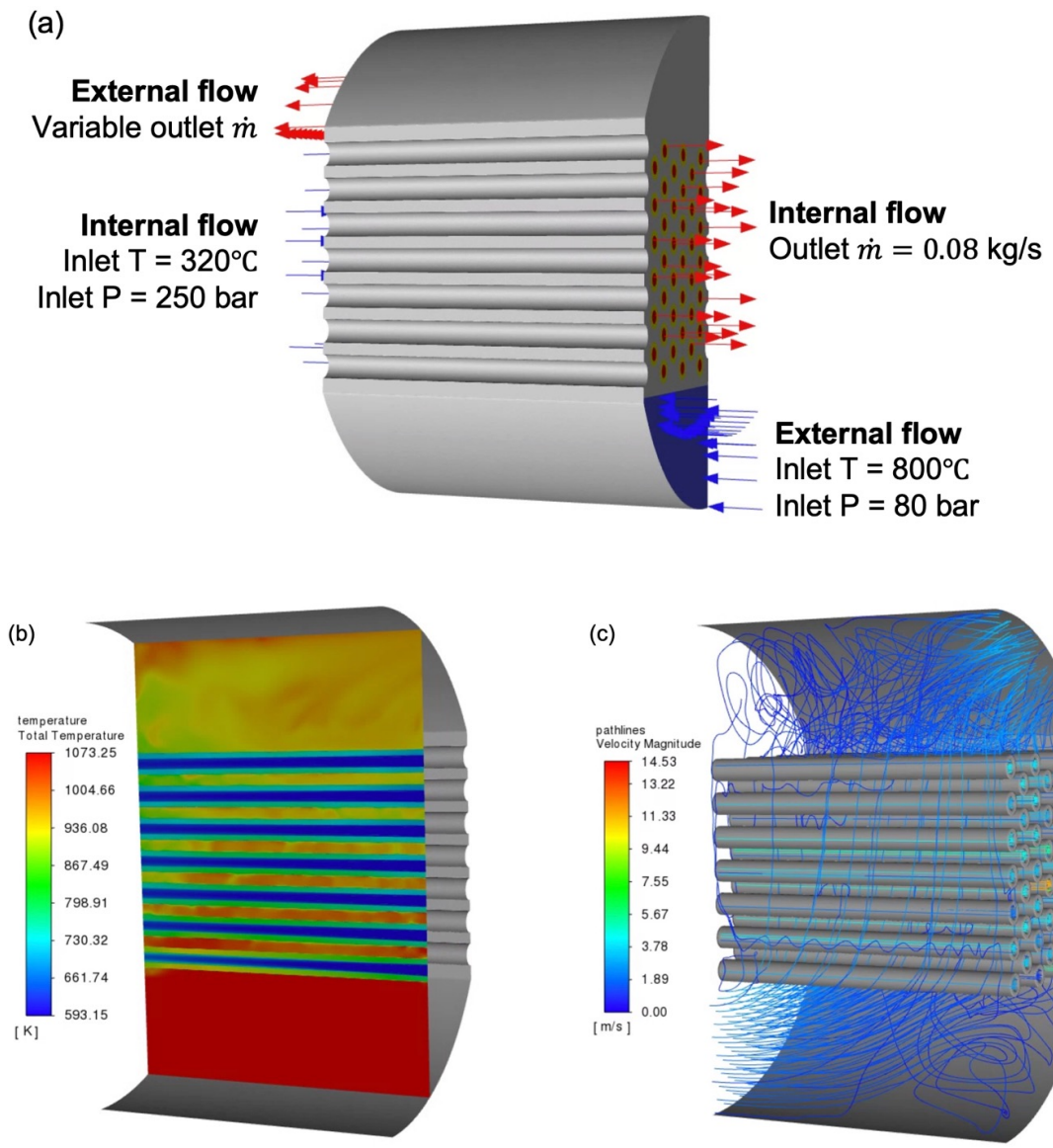

Figure 3.7: (a) Schematic of the domain and boundary conditions in the CFD model for STHX numerical model validation. (b) Temperature contours and (c) velocity pathlines of the $Re_{D_h} = 6,000$ case obtained from ANSYS Fluent.

The comparison metrics are the external heat transfer rate (HTR), internal HTR, tube bundle pressure drop, and unit cell external pressure drop. External and internal HTRs are the amount of energy lost and gained by the external and internal fluid streams respectively.

Unit cell and tube bundle pressure drops of the external flow are obtained from ANSYS Fluent by taking the difference between the pressures at the inlet and outlet of a unit cell and tube bundle respectively. These metrics were similarly calculated from the STHX numerical model and are utilized to perform a comparative analysis. A mesh refinement and grid independence study was performed on a case discussed later with $Re_{D_h} = 6,000$. The external HTR and unit cell external pressure drop of the flow is plotted as a function of the element size in Fig. 3.8. Based on the trend observed in the plot, the mesh with an element size of 0.35 mm was employed for all CFD simulations below.

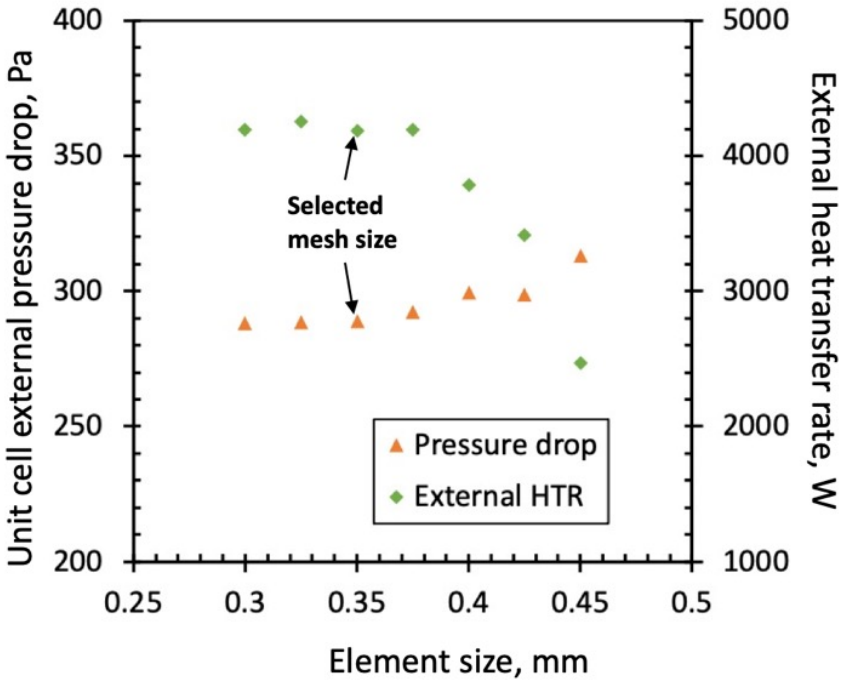

Figure 3.8: Grid size refinement study: comparison of the (a) external heat transfer rate and (b) unit cell external pressure drop as a function of the mesh element size.

Table 3.1: Comparison of performance metrics obtained from the STHX numerical model and CFD simulations.

Re_{D_h}	STHX numerical model						CFD					
	ΔP_1 [Pa]		External		Internal		ΔP_1 [Pa]		External		Internal	
	Unit cell	Tube bundle	HTR [kW]	ΔT [°C]	HTR [kW]	ΔT [°C]	Unit cell	Tube bundle	HTR [kW]	ΔT [°C]	HTR [kW]	ΔT [°C]
2,000	34.6	27.4	2.56	196.0	2.54	25.1	34.9	24.7	2.38	182.5	2.36	23.3
4,000	116.6	89.5	3.62	144.8	3.60	35.6	128.3	83.2	3.19	127.5	3.16	31.3
6,000	266.0	199.9	4.44	114.1	4.42	43.7	289.1	194.7	4.19	107.5	4.15	41.4
8,000	470.6	348.2	5.03	95.3	5.01	49.6	534.2	360.3	4.59	85.9	4.53	44.3
10,000	715.5	523.0	5.47	82.9	5.45	54.0	845.1	550.9	5.04	76.2	5.01	50.1
12,000	1008.2	729.6	5.85	73.7	5.83	57.7	1178.0	785.6	5.36	67.3	5.29	52.1

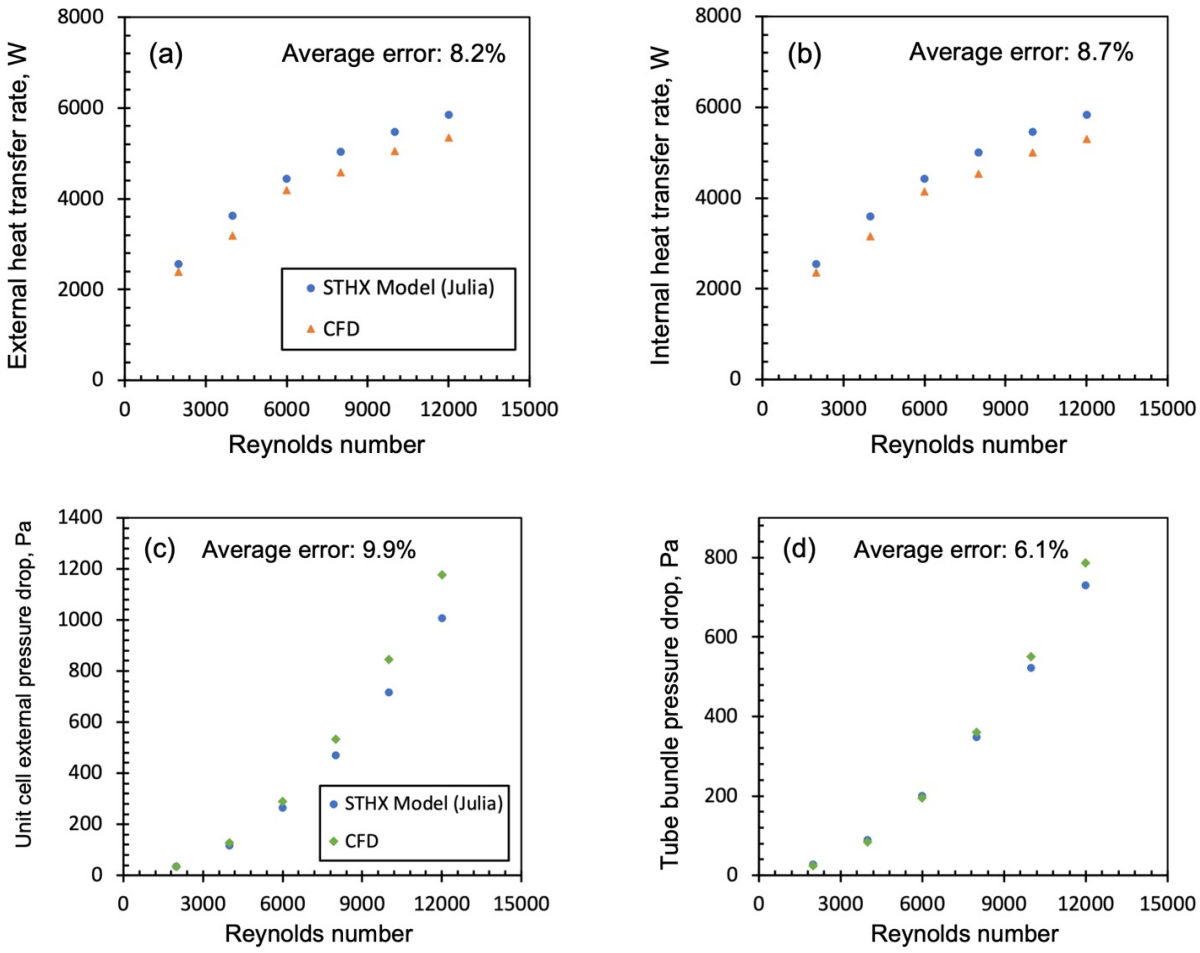

Figure 3.9: Comparison of (a) external heat transfer rate, (b) internal heat transfer rate, (c) unit cell external pressure drop, and (d) tube bundle pressure drop between CFD simulations and the STHX numerical model.

To validate the STHX numerical model and demonstrate its applicability to sCO_2 processes at extreme temperatures and pressures, CFD simulations were carried out for a geometry with 39 tubes, $D_{ot} = 3.18\ mm, P_t = 8.41\ mm, P_l = 4.76\ mm$, and $B = 45.72\ mm$. By using sCO_2 as the working fluid for both streams, six simulations were performed by varying the external outlet mass flow rate, corresponding to a Reynolds number range from 2,000 to 12,000 for the external flow stream. Figure 3.9 provides a comparison of the external HTR,

internal HTR, unit cell external pressure drop, and tube bundle pressure drop obtained from CFD and the STHX model; Table 3.1 summarizes the results. The average deviation between the STHX numerical model and CFD results for HTR and unit cell external pressure drop is less than 10% and the tube bundle pressure drop deviation is 6%, which demonstrates the accuracy of the developed STHX numerical model. Validation for flow over finned geometries would require a more advanced CFD study; therefore, the validation pertains to bare tube banks. The experimental data utilized for bare tube banks involve air flows at conditions similar to the flows over the finned tube banks. All data and correlations appear to translate well to finned tubes and therefore, the correlations and model are expected to exhibit high accuracy even for flows over finned tube banks.

3.3.2 Test case

A sample case was run to assess the outputs of the STHX model while evaluating computational efficiency.

Table 3.2: Inlet conditions and details of parameters used in the sample case.

	External fluid	Internal fluid
Working fluid	sCO_2	sCO_2
Inlet temperature [°C]	800	320
Inlet pressure [bar]	80	250
Mass flow rate [kg/s]	0.1	0.1
Tube material	Haynes 282	
Tube OD	2 mm	

	External fluid	Internal fluid
Transverse pitch	3 mm	
Longitudinal pitch	5.8 mm	
Number of U-tubes	100	
Number of shell passes	12	
HX Length	500 mm	

The inlet conditions for the external and internal flow streams and the STHX geometric parameters of the sample case are provided in Table 3.2.

Table 3.3: Grid refinement study for comparison of the accuracy of performance prediction against computation time of the STHX numerical model.

Grid	Heat transfer rate [kW]		ΔT [°C]		ΔP_1 [bar]	ΔP_2 [bar]	Computation time [s]
	External	Internal	External	Internal			
10×10	52.4	50.0	432.2	397.4	0.143	0.623	1.28
20×20	51.8	50.7	427.6	403.0	0.134	0.568	2.01
30×30	51.8	51.0	427.0	405.6	0.131	0.552	2.87
40×40	51.7	51.1	426.0	406.2	0.130	0.544	4.56
50×50	51.6	51.2	425.5	406.6	0.129	0.539	5.16
60×60	51.6	51.3	425.1	406.9	0.128	0.536	7.35
70×70	51.6	51.3	425.3	407.5	0.128	0.534	8.65
80×80	51.6	51.3	425.1	407.6	0.128	0.532	12.5
90×90	51.6	51.3	425.0	407.8	0.127	0.530	13.9

Grid	Heat transfer rate [kW]		ΔT [°C]		ΔP_1 [bar]	ΔP_2 [bar]	Computation time [s]
	External	Internal	External	Internal			
100×100	51.5	51.3	424.5	407.4	0.127	0.529	17.6

A grid refinement study was conducted by comparing the prediction accuracy against the computation time of the STHX numerical model for the sample case. Several grid sizes were investigated by varying the grid sizing from 10×10 to 100×100, and the results are summarized in Table 3.3. By refining the grid size, the accuracy of performance predictions increases, but the time taken to compute the performance also increases. The difference between the predicted flow stream pressure drops for the 60×60 and 100×100 case is less than 1.4%, but the 60×60 case is 2.4 $\times$ more computationally efficient than the 100×100 case. The performance prediction is effectively grid independent after the 60×60 case and executes in about 7 seconds.

The temperature and pressure fields within the STHX and the thermohydraulic performance of the STHX are evaluated using the numerical code. Temperature contours within the STHX obtained from the numerical model are shown in Fig. 3.10. Pressure profiles of internal and external flow through the STHX are given in Fig. 3.11.

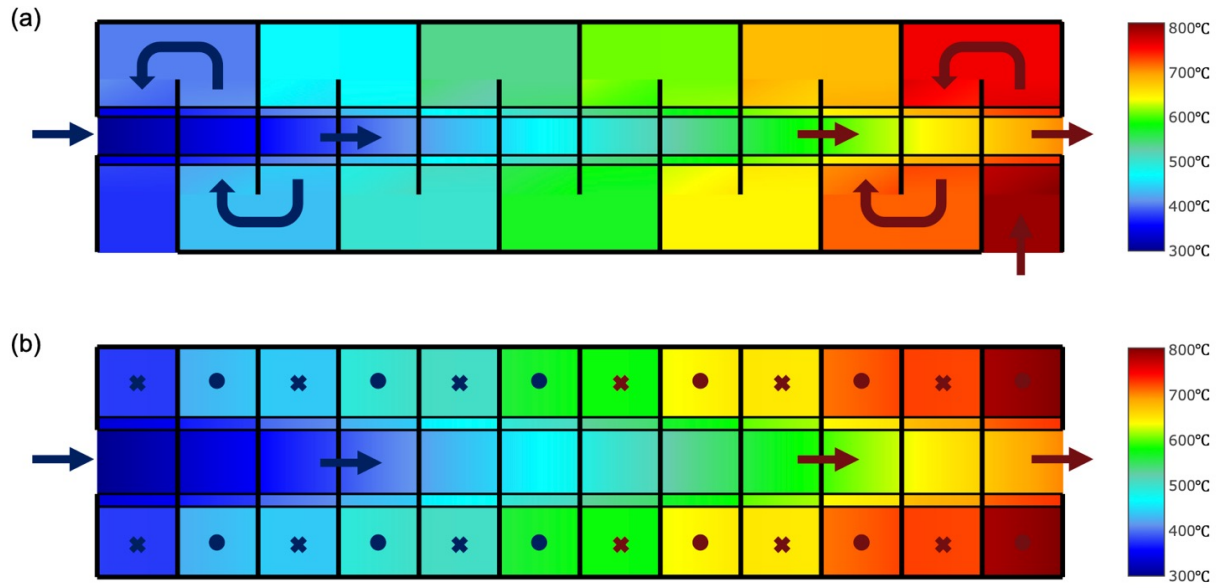

Figure 3.10: (a) Front view and (b) top view of the temperature contours within the STHX obtained from the STHX numerical model for the sample case.

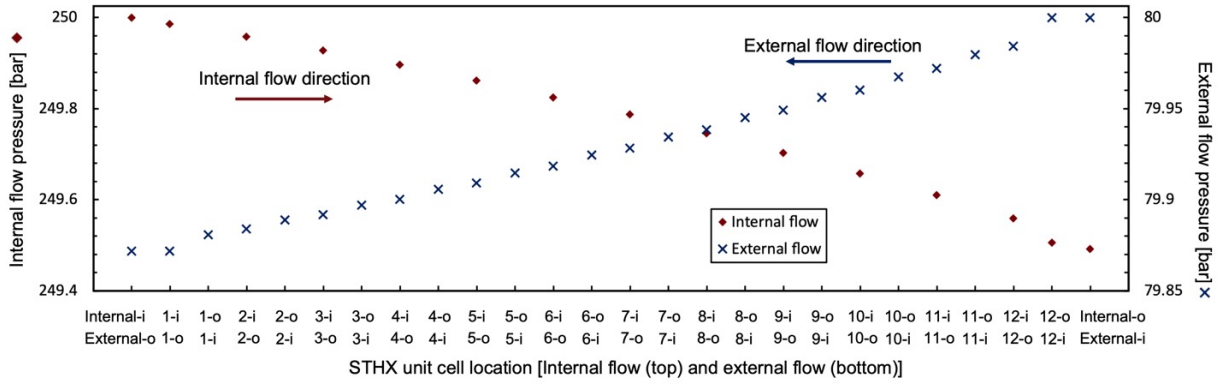

Figure 3.11: Pressure profiles for external and internal flow streams through the STHX for the sample case. The naming convention for the x-axis is: Unit cell number – inlet (i) or outlet (o).

3.3.3 Weight optimization study

To establish a pathway for achieving an optimal HX design, a preliminary optimization study with minimizing the STHX weight as the objective function was performed. The objective of the study is to demonstrate the minimization of STHX weight by selecting five parameters (STHX length, number of tubes, longitudinal pitch, transverse pitch, and number of baffles) as the variable design parameters. A discretized parameter search space is used in this study as shown in Table 3.4. STHX weight is calculated as the summation of the header, shell, tube, and baffle masses. The tube outer diameter is set to 1 mm to achieve attractive power density, and the thicknesses of tube and shell walls are set to be 20% of the outer diameter. TEMA standards were followed in defining the baffle cut, baffle spacing, and minimum tube pitch (among other parameters) while selecting the design space [50, 104]. TEMA is an industry standard based on existing technologies, while microtubes are becoming an increasingly popular option for STHXs. The boundary conditions are given in Table 3.2, and constraints on HX effectiveness ($\epsilon = 0.8$) and HX power (=50 kW) are applied. The length of the STHX is a floating geometric parameter that helps constrain the effectiveness and power to 0.8 and 50 kW respectively.

Table 3.4: Discretized search space for the various geometric design parameters.

	Search space
Number of U-tubes	130, 150, 170, 190
Number of baffles	6, 8, 10, 12
Transverse pitch to tube OD ratio, P_t/D_{ot}	1.5, 1.9, 2.3, 2.7

	Search space
Longitudinal pitch to tube OD ratio, P_l/D_{ot}	1.5, 1.9, 2.3, 2.7

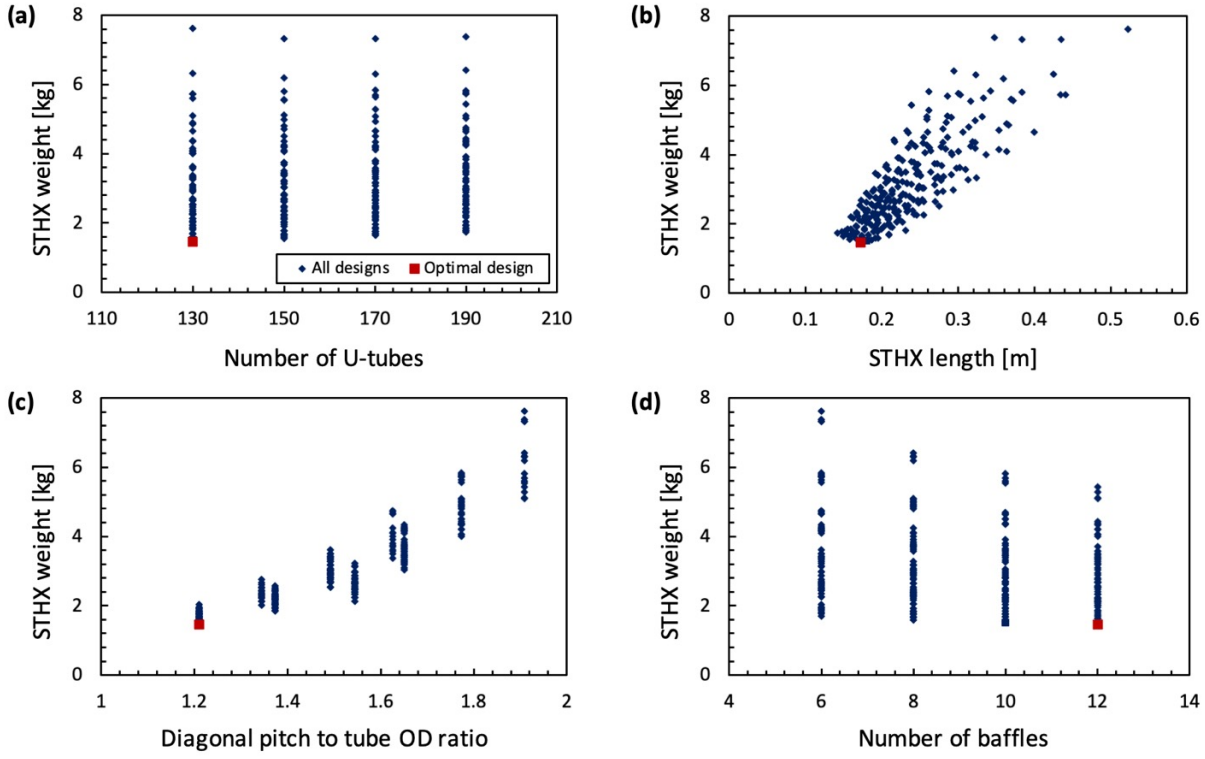

Figure 3.12: Effects of individual geometric parameters on the weight of various STHX designs.

The results from this study help understand the effects of the various geometric parameters on performance metrics, demonstrate the ability of the STHX numerical model [81] to survey the parameter space, and narrow the design space. Figure 3.12 illustrates the variation in STHX weight as a function of the individual parameters obtained for the simulations conducted on various STHX geometries that satisfy the performance metrics. The optimal sCO_2 STHX design has a longitudinal pitch of 1.5 mm, transverse pitch of 1.9 mm, STHX

length of 171.9 mm, 12 baffles (14 external passes), 130 U-tubes, and has a weight of 1.46 kg. This work demonstrates the capability of optimizing the design of the STHX to meet various performance requirements. The developed STHX model provides the possibility to perform more rigorous optimization studies using optimization techniques such as Particle Swarm Optimization and Genetic Algorithm. In addition, minimization of STHX cost can be adopted as a more suitable objective function to find an optimal STHX design that meets aggressive techno-economic metrics.

Air is one of the most common working fluids in the heat exchanger industry. The geometric parameters from the optimal design were used to perform a comparative analysis between STHXs with air and sCO_2 as the working fluids. The STHX length was utilized as a floating parameter in order to maintain a power rating of 50 kW for both heat exchangers. The geometric and performance parameters obtained from the numerical model are summarized in Table 3.5.

Table 3.5: Geometric and performance parameters of the optimal STHX design using sCO_2 and air as the working fluids.

STHX Working fluid	sCO_2	Air
Number of U-tubes	130	
Number of baffles	12	
Transverse pitch [mm]	1.9	
Longitudinal pitch [mm]	1.5	
STHX length [mm]	171.9	182.8
STHX power [kW]	50	

STHX weight [kg]	1.46	1.54
STHX volume [m3]	0.000274	0.000289

The sCO_2 STHX weighs 6.3% less and is 5.5% more compact than the STHX with air as the working fluid for the same power rating. This result indicates the benefit of using sCO_2 as the working fluid and implies that highly compact and efficient power cycles could be achieved by utilizing sCO_2 for future applications.

3.4 Conclusion

This chapter reports a computationally efficient and accurate numerical model developed in Julia programming to predict the performance of STHXs. The geometry of the heat exchanger is modeled using the concept of volume averaging. Highly accurate correlations for external flow and existing correlations for internal flow are utilized to predict the thermohydraulic behavior of flow over and inside the tube banks. The model has the following attributes:

1. The model is highly accurate ($< 10\%$ error for STHX heat transfer rate and pressure drop predictions) and computationally efficient (< 7s per case).

2. The model can predict performance for bare, disc-finned, and pin-finned STHX and is capable of accounting for effects of various geometric parameters.

3. The model is validated against CFD data with sCO_2 as the working fluid for both internal and external flows. The validated operating temperature and pressure are as

high as 800 °C and 250 bar. In principle, the model can predict the performance of STHXs using any working fluid available in the CoolProp database.

This study provides a necessary basis for STHX design with various working fluids and operating conditions. Multi-parameter optimization can be conducted for compact sCO_2 HXs and the optimal design with superior energy density or lowest capital cost can be efficiently obtained from a large design search space.

Chapter 4: Thermohydraulic experiments and model validation

4.1 Introduction

Due to growing interest in MT-STHXs, multiple modeling efforts have been reported to characterize their complex thermohydraulic behavior and to provide a design basis for such HXs. Jiang et al. [43] used similar correlations to those in ref. [51] to develop a MT-STHX design model and optimal designs for recuperative HXs (recuperators) in a 10MWe sCO_2 Brayton cycle. A 2D numerical model for a sCO_2 MT-STHX was developed by Cai et al. [105], and their work proposed a corrected Dittus-Boelter correlation that agrees with the numerical results. Chapter 2 provides original correlations for multiple tube bank configurations and the developed numerical model for designing and optimizing MT-STHXs with sCO_2 is provided in Chapter 3. All these modeling studies provide important insights for developing MT-STHX technologies. However, unlike PCHXs, experimental data for tubular HXs with sCO_2 as a working fluid remain scarce, and new test data are needed to characterize the thermohydraulics of such HX configurations. The objective of this study is to provide experimental datasets for sCO_2 MT-STHXs and to validate related modeling efforts.

This chapter introduces a fabricated MT-STHX with thirty-nine microtubes (ID = 1.75mm) and an integrated experimental system that quantifies HX thermohydraulic performance with sCO_2 and air as the working fluids. The performance parameters for multiple sCO_2 and air

A large portion of this chapter created the paper by K. Jin, A. B. Krishna, P. S. Ayyaswamy, I. Catton, and T. S. Fisher, titled "Thermohydraulic experiments on a supercritical carbon dioxide - air microtube heat exchanger" that is currently under review.

flow rates are obtained, and entrance and exit effects for shell-side flow are discussed. The numerical model from Chapter 3 and Appendix A is used to predict performance for all experimental cases [81, 82, 103]. We compare the numerical results with the experimental data to demonstrate the validity of the model and relevant correlations.

4.2 Experimental setup

4.2.1 sCO_2 heat exchanger experimental system

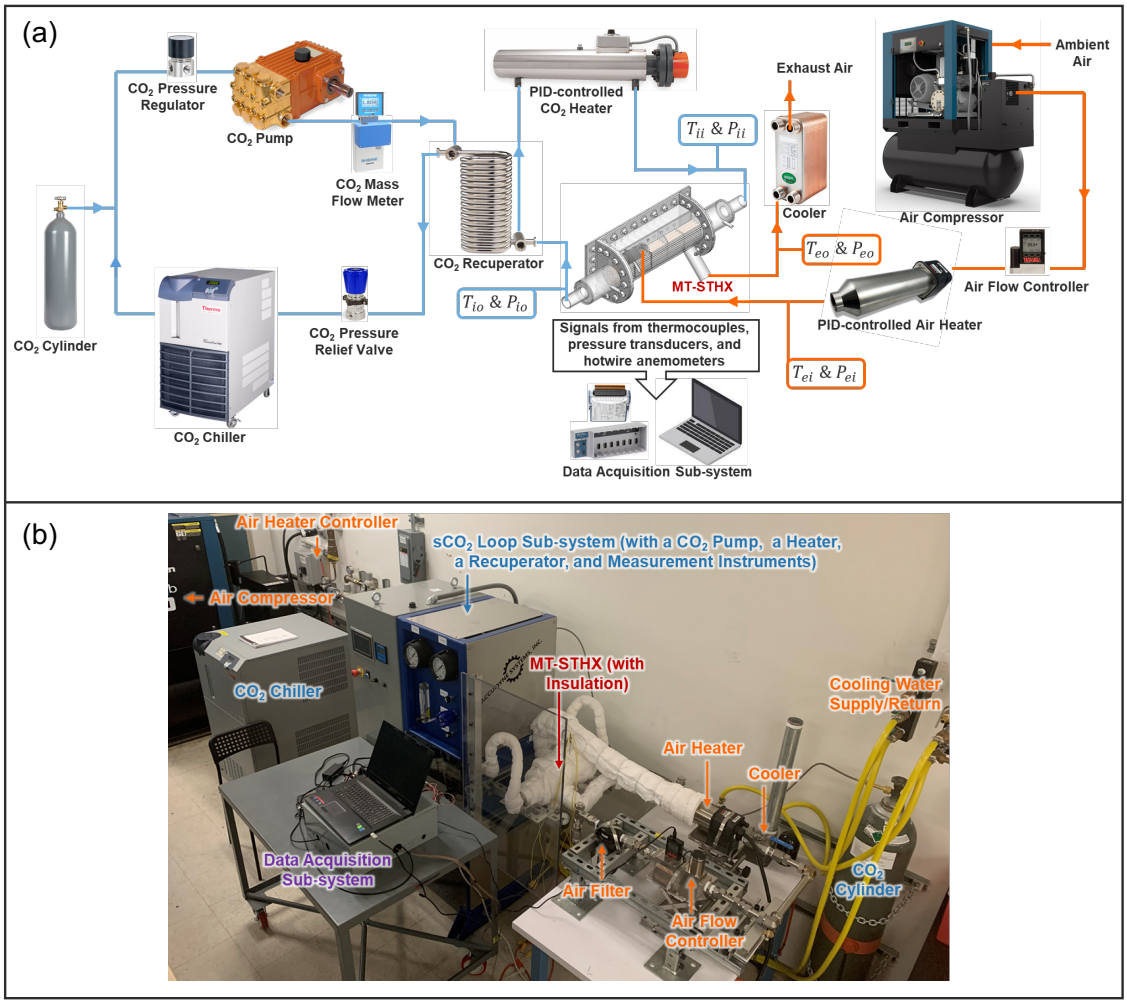

Figure 4.1: (a) Schematic and (b) picture of the integrated test system for the sCO_2-air MT-STHX.

A rig was developed to perform high-temperature thermohydraulic tests on sCO_2 HXs. As shown in Fig. 4.1, the system consists of a closed sCO_2 loop manufactured by Accudyne System, Inc. (components connected by blue pipelines), an air loop (components connected by orange pipelines), a fabricated MT-STHX, and a data acquisition sub-system. The sCO_2 loop provides the test section with sCO_2 flow at 100 bar using a 1kW CO_2 pump assisted by a CO_2 pressure regulator and relief valve. The flow rate can be varied from 12 to 25 g/s and is controlled by the pump speed. The pressurized CO_2 flow is heated by a 2.5 kW PID-controlled heater. The heater outlet temperature can be controlled between 50 and 200 °C within ±0.1°C, thus maintaining the CO_2 at the supercritical state. A commercial recuperator is installed to preheat the sCO_2 flow and minimize the required heater power. The heated flow is cooled down by a 7.5kW chiller before returning to the CO_2 pump to prevent cavitation. Within the air loop, flow is provided by a rotary air compressor, and the flow rate is controlled by a controller ranging from 5 to 45 g/s. A 6 kW air heater can heat the flow up to 300 °C before entering the HX. During an experiment, the system simultaneously provides the heated sCO_2 and air flows at various flow rates. All measured data are post-processed by a data acquisition setup consisting of voltage input modules obtaining temperature and pressure signals, a module chassis, and a laptop with a custom data reading and storage program. Steady-state data, which is the average value of 600 signals in 10 minutes after all temperatures and pressures are stable, for each measurement are collected and saved by this system. Detailed information on specific instruments is provided in section 4.2.3.

4.2.2 Fabricated MT-STHX

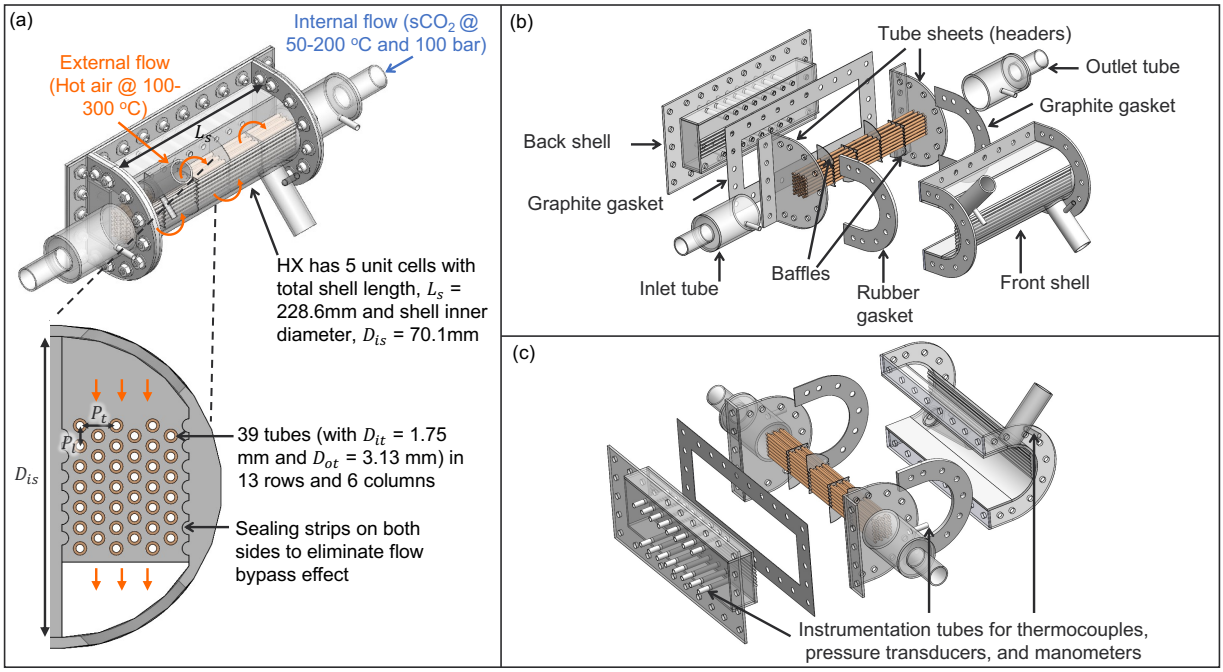

Figure 4.2: Schematic of the designed and fabricated MT-STHX: (a) 3D schematic of the HX assembly, (b) picture of the HX assembly, (c) 3D schematics in exploded view.

The MT-STHX consists of a staggered tube bundle with 39 microtubes (inner diameter = 1.75mm) over 13 rows and 6 columns, as shown in Fig. 4.2(a). The internal (tube-side) flow is sCO_2 (up to 200 °C and 100 bar) and the external (shell-side) flow is pressurized air (up to 3 bar and 300 °C). Stainless Steel 304 was selected as the HX material because it has very similar thermal conductivity to many high-temperature alloys for sCO_2 containment, such as Inconel 625, 718, and Haynes 282. The HX geometry imitates half of the geometry of a standardized U-tube configuration (namely CFU configuration) from TEMA [50]. On both sides of the tube bundle, half-round sealing strips are utilized to minimize flow bypass effects [106, 107].

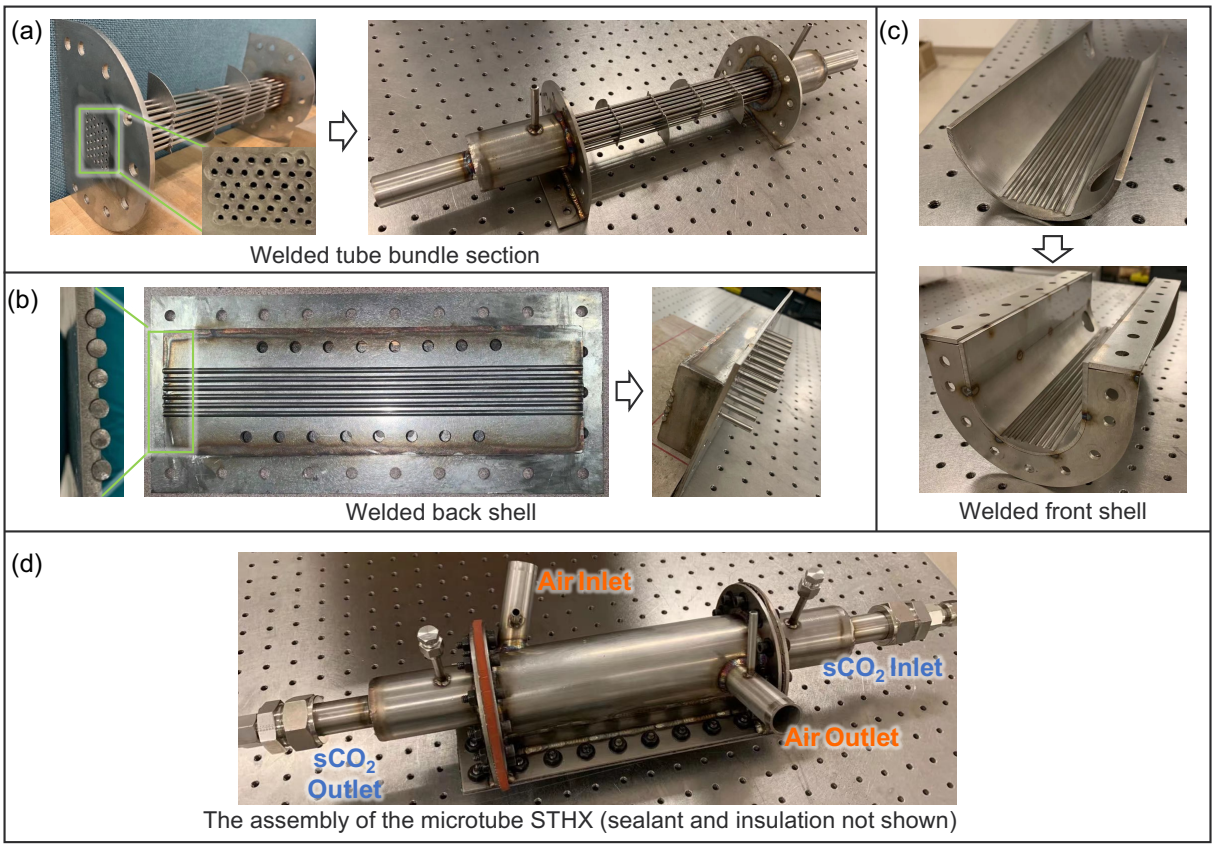

Figure 4.3: Process flowchart for fabricating (a) the tube bundle section, (b) the back shell, (c) the front shell, and (d) assembling the MT-STHX.

Figure 4.2(b) and 4.2(c) contain exploded views of the HX assembly and present the main components within this sCO_2-air HX. The microtubes are arc-welded from the two tube sheets and form the tube bundle section of the STHX. Four segmenting baffles are evenly distributed in the tube bundle region to provide five flow passes for the external flow. The front (curved) and back (straight) shells with sealing strip structures [106, 107] are designed to maintain the shape of cross-section. Flange plates and inlet and outlet tubes are welded to shells and tube sheets. High-temperature graphite and rubber gaskets are used to seal the mating surfaces, with high-temperature metal sealant, bolts, nuts, and washers. Multiple instrumentation tubes are available to measure temperature and pressure at the inlet, outlet,

and local positions within the HX. Swagelok® compression fittings are used to connect the HX with the integrated test system and necessary instruments. Multiple hydrostatic pressure tests up to 110 bar were completed for the tube bundle section to prove that the tube side of the HX can withstand high pressure sCO_2 flow without leakage. Insulation blankets made of ceramic fibers are wrapped around the HX to minimize heat loss during experiments. Critical design details are shown in Figure 4.3 and Table 4.1, respectively.

Table 4.1: Critical design parameters for the MT-STHX.

Parameters	Current MT-STHX	TEMA standards for conventional STHXs [36]	Design consideration
Tube ID, D_{it} [mm]	1.75	> 4.9	The selected tube is a microtube
Tube wall thickness, δ_t [mm]	0.71	> 0.4	The selected wall thickness is $> 33\%$ of the tube ID to provide sufficient creep and fatigue resistance for extreme conditions in commercial sCO_2 MT-STHXs
Longitudinal pitch/ tube OD, P_l/D_{ot}	1.50	> 1.25	
Transverse pitch/ tube OD, P_t/D_{ot}	2.65	> 1.25	All selected pitch ratios follow the TEMA standards [50] and are close to limit values for fabricating the tube sheets in commercial sCO_2 MT-STHXs
Diagonal pitch/ tube OD, P_d/D_{ot}	1.52	> 1.25	

Parameters	Current MT-STHX	TEMA standards for conventional STHXs [36]	Design consideration
Number of tube rows, N_{tr}	13	> 12	The selected numbers of tube rows and columns are sufficiently large to be representative and minimize the HX shell ID
Number of tube columns, N_{tc}	6	> 3	
Baffle spacing to shell ID ratio	0.67	0.2-1.0	The selected baffle spacing follows the TEMA standard and enables a large external Reynolds number ranging from 1,500 to 12,000
Baffle cut to tube diameter ratio	0.25	0.15-0.45	The selected baffle cut follows the TEMA standard and a moderate value is selected
Shell ID, D_{is} [mm]	70.1	-	The selected shell ID is the minimum value to accommodate the tube bundle

Parameters	Current MT-STHX	TEMA standards for conventional STHXs [36]	Design consideration
Shell (tube) length, L_s [mm]	228.6	-	The shell (tube) length is 5 times the baffle spacing because the HX has 5 flow paths

4.2.3 Instrumentation

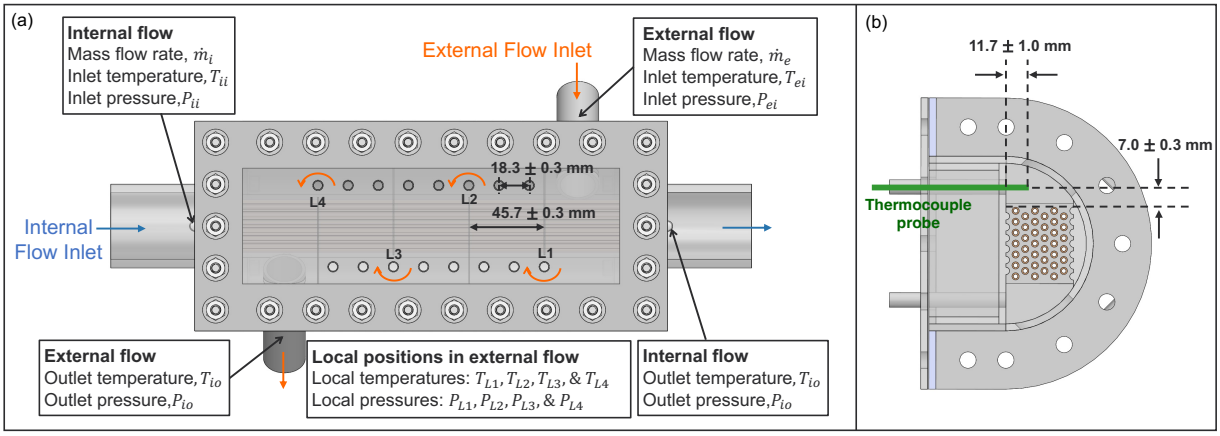

Figure 4.4: Measured parameters and their locations in the MT-STHX: (a) front view and (b) side view.

Figure 4.4(a) indicates the instrumentation locations and all measured parameters for internal (sCO_2) and external (air) flows during the thermohydraulic tests. The mass flow rates for internal flow ($\dot{m}_i$) and external flow ($\dot{m}_e$) are measured by flow meters or mass flow controllers before they enter the HX. Four thermocouple probes and pressure transducers are installed with Swagelok® compression fittings to measure the inlet and outlet temperatures (T_{ii}, T_{io}, T_{ei}, and T_{eo}) and pressures (P_{ii}, P_{io}, P_{ei}, and P_{eo}), at inlet and outlet ports (2.54 cm away from the entrance and exits on both flow sides). The thermocouple probes are K-type, with outer diameter of 1.59 mm (1/16 inches). Multiple pressure transducers measure the static pressure of high-temperature flow with ±1% accuracy. Both instruments are calibrated by vendors, following the National Institute of Standards and Technology (NIST) standards. In addition, local temperatures and pressures in the external flow are measured through the instrumentation tubes on the back shell. Measured data for four locations, L_1 to L_4, are reported here because they are the inlets and outlets for the 2nd, 3rd, and 4th unit cells.

All thermocouple probe tips are located at the center of mass in the flow cross-sections as shown in Fig. 4.4(b). During an additional hydraulic test (no heat input), high accuracy ($\pm 0.5\%$) manometers measure the pressure drops in 1st to 5th unit cells (between external inlet and L1, L1 and L2, ..., L4 and external outlet) at turns. The manometer data match well with calculated pressure differences using pressure transducer data but generally have less uncertainties.

4.3 Data reduction and error analysis

Utilizing temperature and pressure measurements, flow enthalpies (h) are obtained from the CoolProp database [101] to calculate internal thermal power, Q_i, the external power, Q_e, and the ideal HX power, Q_{ideal} as shown below:

$$Q_i = \dot{m}_i \left[h_{io} \left(T_{io}, P_{io} \right) - h_{ii} \left(T_{ii}, P_{ii} \right) \right] \tag{4.1}$$

$$Q_e = \dot{m}_e \left[h_{ei} \left(T_{ei}, P_{ei} \right) - h_{eo} \left(T_{eo}, P_{eo} \right) \right] \tag{4.2}$$

$$Q_{ideal} = min \left\{ \dot{m}_e \left[h_{ei} \left(T_{ei}, P_{ei} \right) - h_{eo,min} \left(T_{ii}, P_{eo} \right) \right], \ \dot{m}_i \left[h_{io,max} \left(T_{ei}, P_{io} \right) - h_{ii} \left(T_{ii}, P_{ii} \right) \right] \right\} \tag{4.3}$$

For the MT-STHX, Q_i theoretically equals to the HX power (namely HX capacity), while Q_e is the sum of the HX power and heat loss through the insulation. Therefore, HX effectiveness is derived as:

$$\epsilon = \frac{Q_i}{Q_{ideal}} \tag{4.4}$$

The HX thermal conductance, UA, is calculated using the power and log-mean temperature difference:

$$UA = \frac{Q_i}{\Delta T_{lm}} \tag{4.5}$$

$$\Delta T_{lm} = \frac{(T_{io} - T_{ei}) - (T_{ii} - T_{eo})}{\ln \frac{T_{io} - T_{ei}}{T_{ii} - T_{eo}}} \tag{4.6}$$

Pressure drops and HX power are important performance metrics and are calculated from temperature and pressure data. The total external pressure drop, ΔP_{tot}, and single unit cell (1st to 5th unit cell) pressure drops, ΔP_k ($k = 1,\ 2, \ldots 5$), are used to quantify flow friction in the fabricated STHX, as defined by:

$$\Delta P_{tot} = P_{ei} - P_{eo} \tag{4.7}$$

$$\Delta P_1 = P_{ei} - P_{L1} \tag{4.8}$$

$$\Delta P_k \, (k = 2, 3, 4) = P_{Lk} - P_{Lk-1} \tag{4.9}$$

$$\Delta P_5 = P_{L4} - P_{eo} \tag{4.10}$$

Local pressure drop data on the shell-side are used to estimate the tube bundle pressure drop $\Delta P_{tb,k}$ and the average friction factor f_k for the kth unit cell (valid for k=2, 3, and 4) [64] for flow over the tube bundle:

$$\Delta P_{tb,k} = \Delta P_k - \Delta P_{uw,k} - \Delta P_{lw,k} \tag{4.11}$$

$$f_k = \frac{\Delta P_{tb,k}}{\frac{1}{2}\rho_{k,avg} u^2_{max,k} \frac{4X_l}{D_h}} \tag{4.12}$$

In these equations, $\Delta P_{tb,k}$ is the overall pressure drop of the kth unit cell less the pressure drops in the upper window regions ($\Delta P_{uw,k}$) and bottom ($\Delta P_{lw,k}$) of the tube bundle. These window region pressure drops are calculated from ref. [46]:

$$\Delta P_{uw,k} = \frac{\dot{m}_e^2}{\rho_{Lk-1} A_s A_w} \tag{4.13}$$

$$\Delta P_{lw,k} = \frac{\dot{m}_e^2}{\rho_{Lk} A_s A_w} \tag{4.14}$$

where A_s is the interspace front plane area through the tube bundle and A_w is the cross-sectional area of the window inlet/outlet. ρ_{Lk-1} and ρ_{Lk} are the densities of external flow at the locations Lk-1 and Lk (k=2,3, and 4), respectively, as shown in Fig. 4.4. They are obtained from the CoolProp database [101] using measured temperatures and pressures at these locations.

All measured data is collected at steady state and has negligible precision uncertainty. The main experimental errors are bias errors caused by device inaccuracies. The propagated errors of calculated parameters are estimated using [108]:

$$\frac{\delta y}{y} = \sqrt{\sum_{i=1}^{n} \left(\frac{\partial y}{\partial x_i} \delta x_i \right)^2} \tag{4.15}$$

where $y = f(x_1,\ x_2, \ldots, x_n)$ represents any calculated parameters and $x_1, x_2, \ldots, x_n$ are measured parameters such as temperature and pressures. All errors are listed in Table 4.2.

Table 4.2: Bias errors of measured parameters and calculated performance metrics.

Measured Parameters		Calculated Performance Metrics	
Parameter	Error	Parameter	Error
Temperature [K]	± 0.8%	sCO_2 flow power, W_i [W]	± 1.8%
sCO_2 pressure [MPa]	± 1.0%	Air flow power, W_e [W]	± 1.9%
sCO_2 mass flow rate [kg/s]	± 0.5%	Effectiveness, ϵ	± 2.7%
Air pressure [kPa]	± 1.0%	ΔT_{lm} [°C]	± 2.1%
Manometer [kPa]	± 0.5%	UA [W/K]	± 2.8%
Air mass flow rate [kg/s]	± 0.8%	Transducer [kPa]	± 1.4%

4.4 Results and discussion

Multiple experiments were completed with the MT-STHX test system, and steady-state data were recorded. Critical HX performance metrics were calculated and compared with numerical predictions from the model developed in Chapter 2.

4.4.1 Thermohydraulic tests

Thirty-six experimental cases with varying rates of external (air) and internal (sCO_2) flows were performed for the MT-STHX. Nine air flow rates (5, 10, . . . , 45 g/s) and four sCO_2 flow rates (12, 15, 18, and 21 g/s) were selected. In each case, the air flow inlet temperature was influenced by the air heater capacity and therefore varied from 166 to 108 °C with increasing flow rate. Given that the air flow loop was open, the air inlet pressure was dominated by the external pressure drop of STHX and the cooler. The inlet conditions for sCO_2 flow were

controlled by the sCO_2 loop system with the inlet pressure at around 100 bar. The inlet temperature was set to be 70 or 60 °C to maintain the supercritical state and to provide sufficient temperature difference between two flow streams. The full data sets are shown from Table B.1 to Table B.4 in Appendix B.

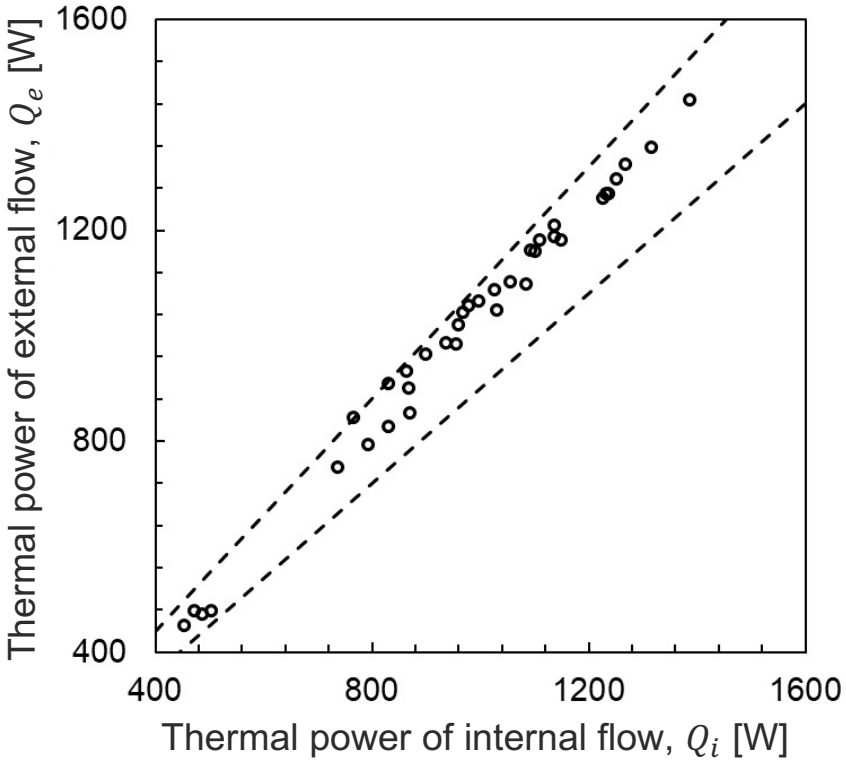

Figure 4.5: Comparison of thermal power between the internal (sCO_2) and external (air) flow.

Figure 4.5 shows the thermal power comparison between internal and external streams for all 36 test cases. The results indicate that the deviation between the sCO_2 and air power is within ± 10% (average deviation = 4.4%) and implies that all tests reached steady state with an acceptable heat balance. Most cases have slightly higher air flow power because the air flow is on the external side and encounters a small environmental heat loss.

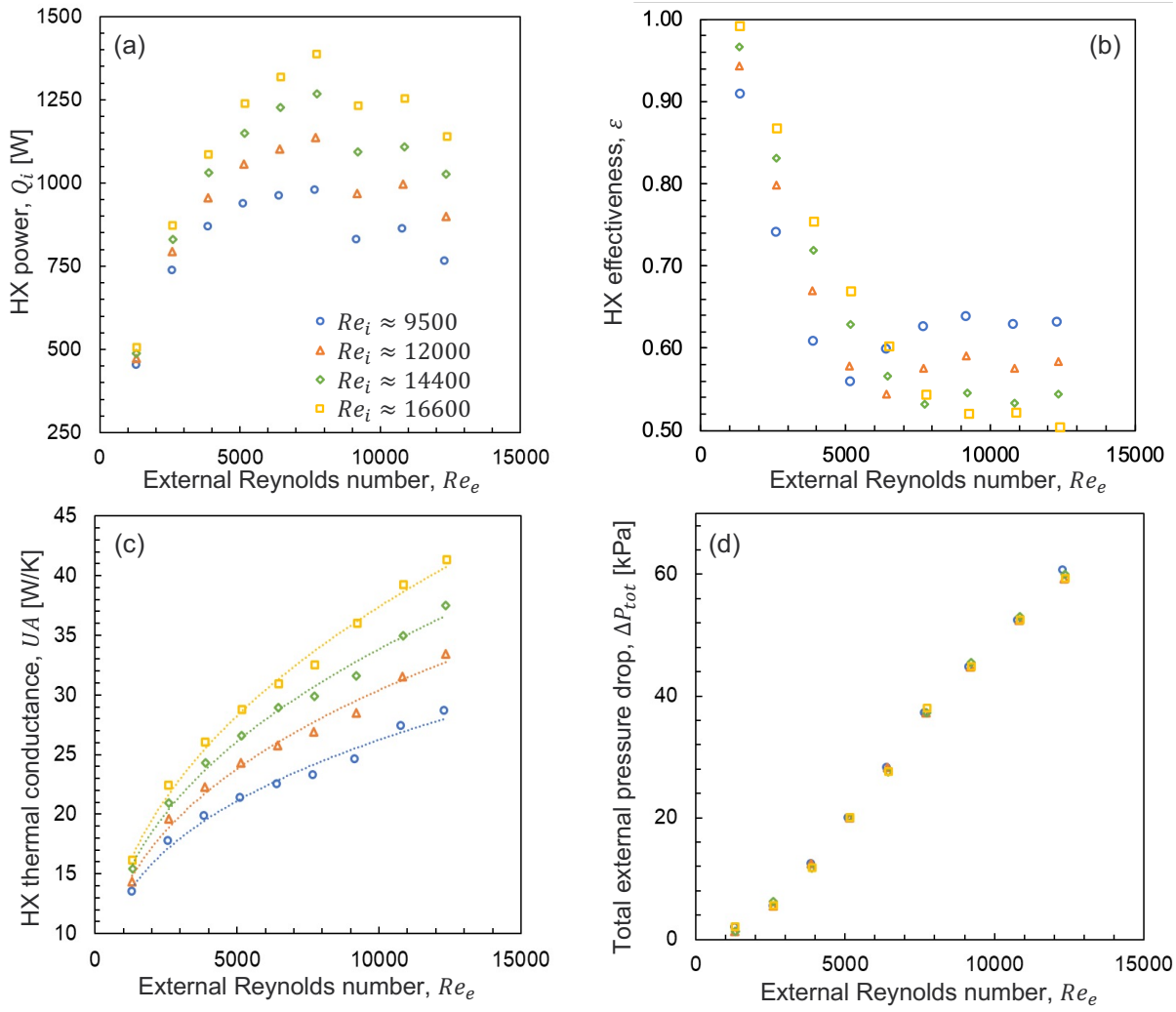

Figure 4.6: Heat exchanger (a) power (HX capacity), (b) effectiveness, (c) thermal conductance, and (d) total external pressure drop in thermohydraulic tests.

The variations of critical performance metrics are plotted in Fig. 4.6 as functions of external Reynolds number. Fig. 4.6(a) shows the heat exchanger capacity from thirty-six thermohydraulic tests. The capacity increases with Re_e from 1000 to 8000 because the air heat transfer rate increases, and the inlet temperatures (or heater outlet temperature) are maintained above 150 °C. When $Re_e > 8000$, the air heater reaches full power, and its temperature output cannot be maintained with increasing Reynolds number. Therefore, the

set temperature of the air heater outlet is reduced to protect the heater from overloading, causing significant drops and complex variations for the HX inlet temperature and capacity.

Fig. 4.6(b) shows heat exchanger effectiveness and indicates the selected flow rates cover a wide effectiveness range. At low Re_e, ϵ is relatively high because the external flow outlet temperature is similar to the internal flow inlet temperature. In this scenario, ideal HX power, Q_{ideal}, is calculated based on the external flow and is very close to the actual HX power, Q_i. With Re_e increasing from 0 to 5000, both Q_{ideal} and Q_i rise while Q_{ideal} has a higher increment, which results in a reduction of ϵ. On the other hand, when Re_e becomes sufficiently large, Q_{ideal} is calculated from the internal flow, reversing the trend of Q_{ideal} and ϵ. Effectiveness first increases and then decreases with increasing Re_e in most cases. When the internal flow rate is relatively high, this trend is not apparent because ϵ is also affected by the heater outlet temperature, which decreases with Re_e for $Re_e > 8000$.

The variation of the HX conductance UA and the relevant trend lines of are presented in Fig. 4.6(c). UA increases with both internal and external flow rates with a power-law Reynolds number dependence. The total air flow pressure drop on the external side increases linearly with external Reynolds number, as shown in Fig. 4.6(d). Data for various internal flow rates fall on top of each other because variations in internal flow rate at a given external flow rate affects only the external flow temperature profile and air properties, which have negligible effects on external pressure drops. The total external pressure drop is relatively complex and consists of contributions from all unit cells. In each unit cell, pressure drop occurs in both the tube bundle and window regions. To better understand the characteristics of pressure drops on the external side of the MT-STHX, additional tests with no heat input were performed and are described in the next section.

4.4.2 Additional hydraulic tests

Given that the temperature and property variations do not significantly affect the pressure drop trend, additional hydraulic tests for external flow were performed without any heat input. Temperatures and pressures of inlet and outlet planes of each unit cell are measured in sequence to obtain density and viscosity data for Reynolds number calculations. High-accuracy manometers were utilized to measure pressure drops in each unit cell to achieve less bias error. The measured data are shown in Table B.5 in Appendix B.

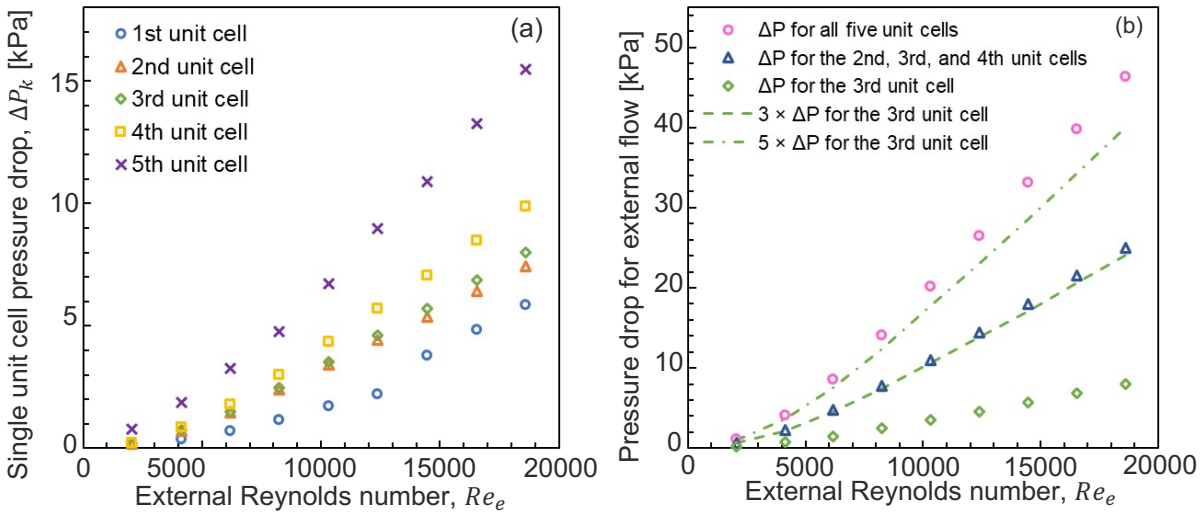

Figure 4.7: Results from additional hydraulic experiments: (a) single unit cell pressure drops (b) pressure drop comparison among all five cells, central three cells, and the central unit cell.

Figure 4.7(a) compares the external pressure drop of each unit cell for Reynolds number ranging from 2000 to 18000. Unit cell pressure drops increase in sequence because the flow density decreases and velocity increases along the flow path. However, the pressure drop in the 5th unit cell is much larger than other cells, indicating that the external flow outlet

port causes additional pressure drop due to sudden contraction of the flow cross-sectional area when flow exits the last unit cell. In addition, the pressure drop in the 1st unit cell is also affected by the entrance port and is significantly lower than other cells. Both entrance and exit effects can be different for various wrap configurations of HXs and therefore is not further considered in this study. Pressure drops of all cells, the central three cells, and the 3rd unit cell are plotted together in Figure 4.8(b). The total pressure drop is found to be significantly higher than 5 times the 3rd unit cell pressure drop, which is mainly caused by flow exit effects. When neglecting the 1st and the 5th unit cells, the pressure drop of the central three cells is very close to 3 times the 3rd unit cell pressure drop. This observation implies that the central three cells encounter much less effect of the exit and entrance and are relatively more representative.

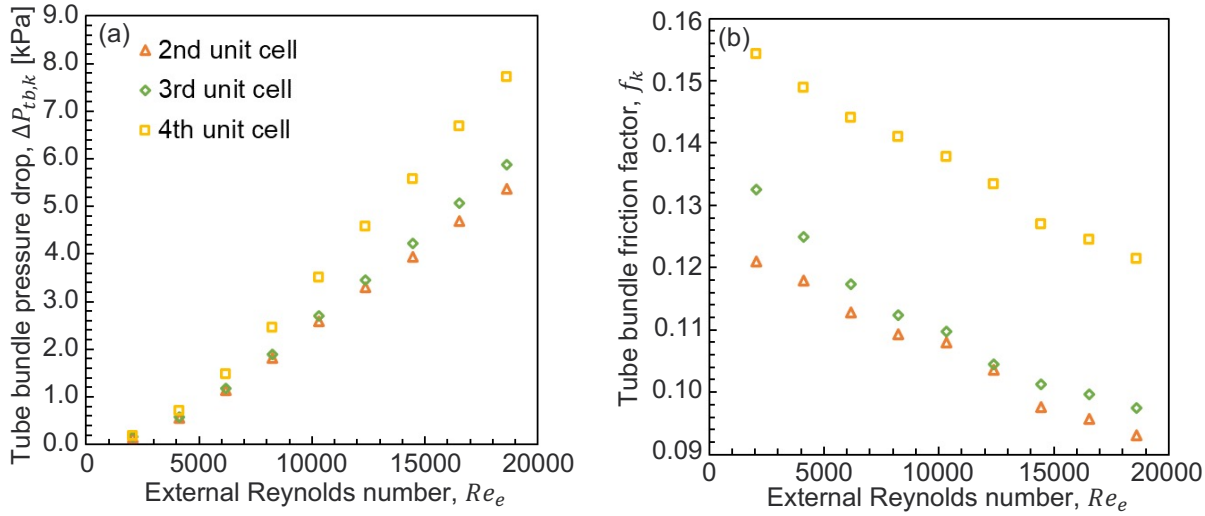

Figure 4.8: Results from additional hydraulic experiments: (a) tube bundle pressure drops and (b) friction factors for 2nd, 3rd, and 4th unit cells.

4.4.3 Comparison with model predictions

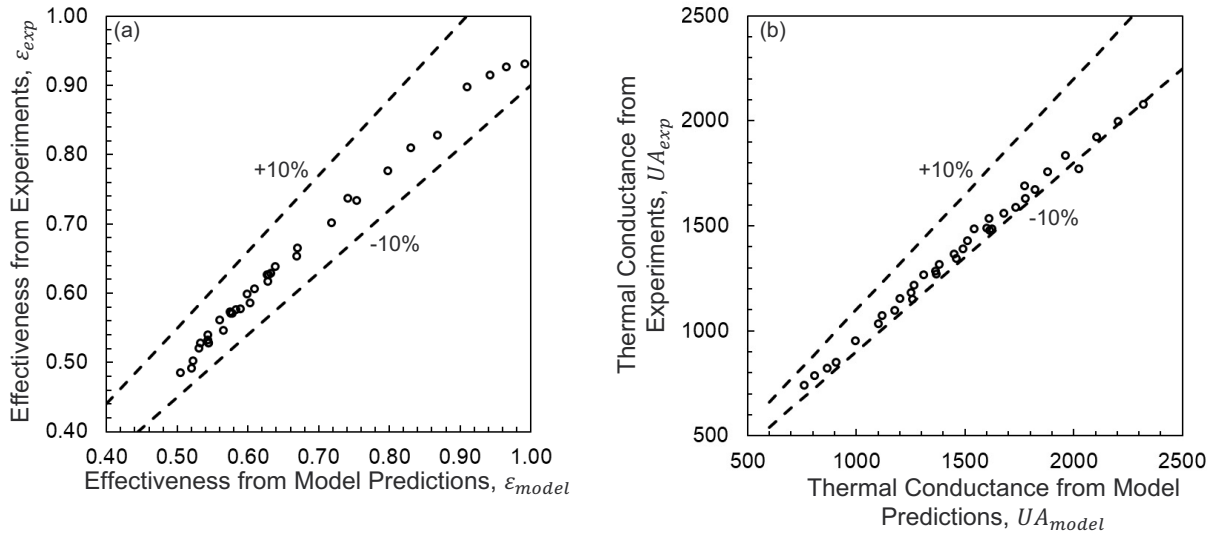

Figure 4.9: Comparison between experimental and model predictions for (a) HX effectiveness and (b) overall heat transfer coefficient.

To obtain the model predictions for all tested cases, the inlet flow rates, temperatures, and pressures of both streams in the experiments are input to the model, and relevant HX performance metrics are calculated as model outputs. Figure 4.9(a) illustrates a comparison of HX effectiveness obtained from experimental results and model predictions. The maximum and average deviations (absolute difference) for all 36 cases are 6.1% and 2.1%, respectively. All compared cases have deviations within ±10%, indicating that the model accurately predicts the effectiveness of this STHX. The overall heat transfer coefficients from experiments and model predictions are plotted in Figure 4.9(b). The maximum and average deviations for all 36 cases are 12% and 6.6%, respectively. In total, thirty-four cases exhibits good agreement with model predictions within 10% deviation.

These results in this section provide a thorough validation for using this numerical model to predict the heat transfer performance of the MT-STHXs with different working fluids. All predictions slightly underestimate the heat transfer coefficients in the HX, and the mismatch increases with the increasing internal Reynolds number. The primary cause is that the model does not account for heat loss from the external flow and predicts higher ΔT_{lm} (inversely proportional to heat transfer coefficient) than the experimental results. In future scaled-up MT-STHXs with less heat loss, the temperature difference between the two streams may be larger, and the model agreement is expected to improve even further.

Comparison data for total external pressure drop obtained from the thermohydraulic and additional hydraulic experiments are plotted in Figure 4.10(a) and 4.10(b). The maximum and average deviations between the experimental and model results for both datasets are 13% and 8.0%, respectively. The deviations increase when the Reynolds number and pressure drop increases. This trend might be caused by entrance and exit effects which are more prominently evident at higher Reynolds numbers. To avoid these effects, Figure 4.10(c) compares the pressure drop between the 2nd and 4th unit cells in the additional hydraulic tests with the model predictions. The maximum and average deviations are found to be 8.2% and 3.3% respectively, which is much less than the deviation for the total external pressure drop. In addition, the pressure drop comparison for the representative (3rd) unit cell shows an even closer agreement (4.3% for the maximum deviation and 1.4% for the average), as shown in Figure 4.10(d). This finding supports the previous assertion that exit and entrance effects are the main cause for the total pressure drop mismatch. Regardless, the model can accurately predict the pressure drop for the representative unit cell in this study and should have sufficient accuracy for estimating the hydraulic performance of industrial-scale

MT-STHXs, in which most unit cells will behave in a representative manner without exit or entrance effects.

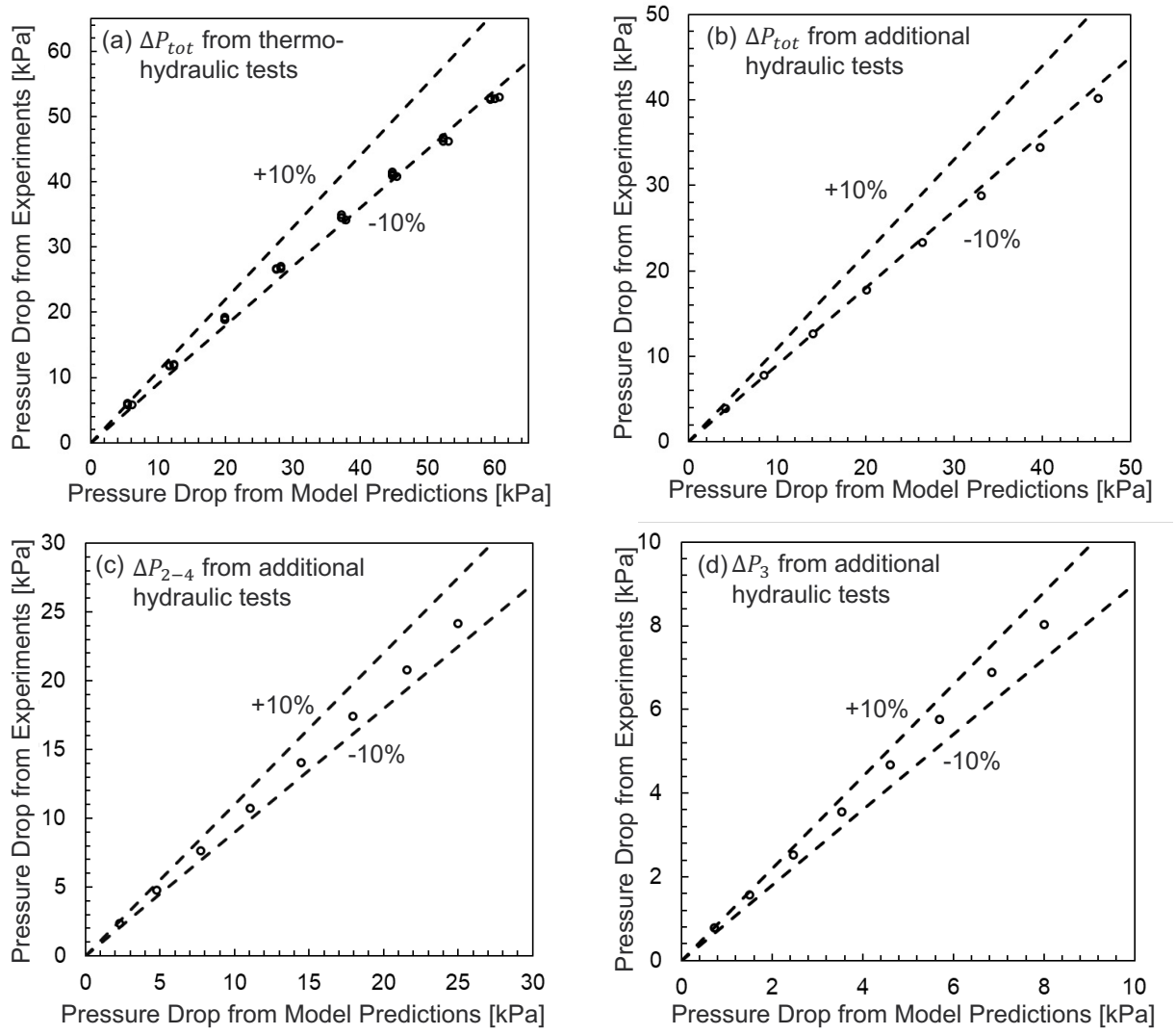

Figure 4.10: Comparison between experiments and model predictions for (a) total pressure drop in thermohydraulic experiments, (b) total pressure drop in additional hydraulic experiments, (c) pressure drop from 2nd to 4th unit cells in additional hydraulic experiments, and (d) 3rd unit cell pressure drop in additional hydraulic experiments.

More detailed calculation and comparisons have been conducted for the representative (2nd and 3rd) unit cells in this study. Figure 4.11(a) and 4.11(b) show average friction factors

of tube bundles in the 2nd and 3rd unit cells from the experiments and model predictions. Deviations for all cases are within ±10%, and the average deviation is 3.1%, indicating that the developed friction factor correlation in the model is highly accurate, and the method used to calculate the pressure drops in window and tube bundle regions is appropriate. In brief, the current analysis qualitatively and quantitatively proves the validity of the selected model and correlations and provides sufficient confidence for using these tools in future design and optimization studies of MT-STHXs.

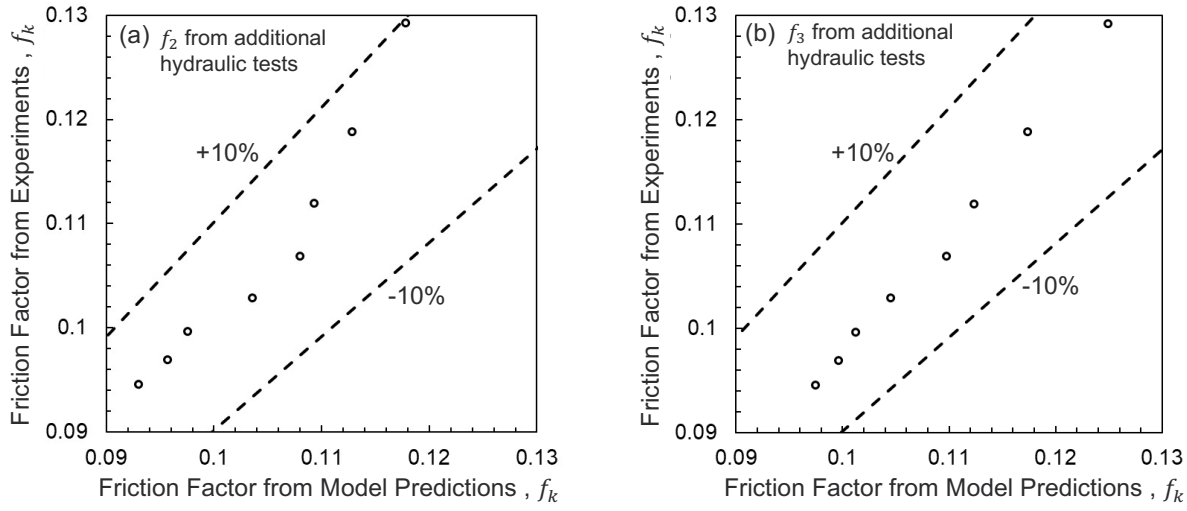

Figure 4.11: Comparison between experiments and model predictions for (a) 2nd unit cell friction factor (b) 3rd unit cell friction factor.

4.5 Conclusion

In this study, a five-unit-cell MT-STHX is fabricated, and an integrated experimental system uses sCO_2 and air as working fluids. Multiple sets of thermohydraulic experiments are reported over an extensive range of tube-side and shell-side Reynolds numbers. The main conclusions are summarized as:

1. The fabricated MT-STHX contains representative design features for the same type of sCO_2 HXs at commercial scales and provides a basis for design and fabrication.

2. The performed experiments provide thermohydraulic performance datasets for MT-STHXs with sCO_2 and air as working fluid. The sCO_2 Reynolds number varies from 9,000 to 17,000, and the air Reynolds number ranges from 2,000 to 18,000.

3. The 1st, 4th, and 5th unit cells in the fabricated MT-STHX have non-negligible entrance and exit effects at high Reynolds numbers. Conversely, the 2nd and 3rd cells exhibit similar performance characteristics and can be considered representative unit cells that have similar behavior to cells in scaled-up MT-STHXs.

4. Experimental results in this chapter provide a comprehensive validation for the correlations developed in Chapter 2 and the numerical model to predict the thermohydraulic performance of a sCO_2 MT-STHX detailed in Chapter 3.

Chapter 5: Technoeconomic optimization using particle swarm optimization

5.1 Introduction

The need to achieve enhanced component designs has produced numerous methodologies to optimize heat transfer processes. Graphical analysis of the search space [109, 110], phase-changing optimization design [111], and simulated annealing are among the many methods reported in the past. CFD may be an accurate option to perform optimization studies, but the time costs are heavy [112, 113]. Genetic Algorithms (GAs) are frequently used to optimize thermal devices. Caputo et al. [114] computed total cost as a function of capital cost and energy expenditure and performed an economic optimization using a GA. Enforcing pressure drop as a constraint, Selbaş et al. [47] used a GA to obtain optimal design parameters for an STHX. Hilbert et al. [113] performed a GA optimization using direct numerical simulations with multiple objective functions - maximizing heat transfer and minimizing pressure loss.

Though GAs are common, other methods have been reported to overcome the dependence of GAs' optimal solutions on initial conditions. The artificial bee colony algorithm was shown by Sahin et al. [115] to converge much faster than the conventional GA and trial-and-error methods, but this method requires optimal control parameters to avoid premature convergence. Rao et al. [116] and Rao and Patel [117] proposed a teaching-learning based optimization algorithm to decrease the reliance on manual adjustment of parameters. Hadidi

A large portion of this chapter created the paper by A. B. Krishna, K. Jin, P. S. Ayyaswamy, I. Catton, and T. S. Fisher, titled "Technoeconomic optimization of superalloy supercritical CO_2 microtube shell-and-tube-heat exchangers" that is currently under review.

et al. [118] developed a design method based on the imperialist competitive algorithm, and later, Hadidi and Nazari [119] developed an approach based on a biology-based algorithm, namely, the biogeography-based optimization algorithm (BBO). Variants of Particle Swarm Optimization (PSO) [120, 121] are reliable techniques to perform these optimization studies. Unlike gradient-based algorithms such as the gradient-descent method, PSO is a gradient-free method that does not require gradient information at any point in time. This feature eliminates the need for storage of information that specifies a zero gradient at the saddle point, and thus, PSO is unaffected by discontinuities of the objective function [122, 123].

Optimizing the design parameters of HXs to achieve superior performance metrics or targets is critical to the advancement of technology in industrial and aerospace applications. These targets are represented by an objective function and are most commonly the minimization of cost or maximization of heat transfer. Optimization procedures are carried out by defining the objective, a geometric parameter search space, and a set of design constraints [88, 124–126]. Common constraints in STHX design ensure that pressure drop does not exceed a given limit and prescribe a minimum value for effectiveness. Then, an iterative trial-and-error computation is performed until a set of optimal design values for the geometric parameters of the heat exchanger is obtained by minimizing or maximizing the objective function within the parameter search space.

Entropy generation [127], entransy generation [128], and field synergy number [129] have been used as objective functions in the past, but the most commonly investigated approach involves the minimization of total cost due to its importance in achieving relevant designs for industrial and aerospace applications [47, 115, 119]. Estimation of capital cost of STHXs is

commonly predicted using the Hall equation, which was developed using the detailed costing procedure for heat exchangers provided by Purohit as a baseline [130]:

$$C_{cap} = a_1 + (a_2 \times A_{HT}^{a_3}) \tag{5.1}$$

where A_{HT} is the heat transfer area of the heat exchanger.

However, the Hall equation was developed for STHXs utilizing carbon steel, stainless steel, and titanium as the solid materials. Other costing methods include, but are not limited to, the Pikulik method [131], which can be used for large kettle-type heat exchangers and fixed tube-sheet heat exchangers, the Guthrie method [132] which utilizes heat exchanger surface area to determine capital cost, and the Corripio method [133] which utilizes operating pressure, material used, type of heat exchanger, and surface area to calculate capital cost [134].

An accurate, efficient, and versatile numerical model is essential to conduct optimization studies with multiple parameters. This paper utilizes the correlation-based numerical model developed by Krishna et al. [81, 82, 103] to predict thermohydraulic performance of MT-STHXs. The model is capable of utilizing any working fluid in the CoolProp database [101] and can accurately obtain thermophysical properties of these working fluids and various temperatures and pressures. Any solid material of the user's choice for the MT-STHX can be utilized, and the model has a large application scope. Current cost models are either applicable to devices with steel as the solid material or are not comprehensive enough to account for the various components of heat exchangers. The objective of this study is to develop a constrained optimization methodology for MT-STHX design and a related cost model, the form of which can be adapted to MT-STHXs with various configurations and dif-

ferent solid materials. Two separate optimization studies are carried out with minimization of capital cost and maximization of power density as objectives. A comparative analysis between cost optimized and power-density optimized MT-STHXs for various MT-STHX capacities is performed to emphasize trade-offs between cost and power density while optimizing within MT-STHX constraints. An additional cost-constrained optimization study is conducted with maximization of power density as the objective to provide a baseline for optimization of future aerospace devices.

5.2 Particle swarm optimization

PSO is a metaheuristic, gradient-free algorithm initially developed by Kennedy and Eberhart [135, 136] and is generally used to optimize non-linear functions. PSO is an evolutionary computation algorithm developed with inspiration from the navigation and foraging of fish schools, bird flocks, and insect swarms [120]. Each individual, known as a particle, interacts with the other particles in the swarm to share essential information and perform complicated tasks collectively or in this case find optimal solutions based on a given objective [137]. Each particle represents a potential solution in an n-dimensional space, where n represents the number of parameters to be optimized [137, 138].

In the PSO algorithm, minimum and maximum values of a given parameter are utilized as inputs and an n-dimensional space comprising these parameters is defined as the search space of the problem. The fitness of a particle is defined as the value of the objective function which in this study is either the MT-STHX cost or the reciprocal of MT-STHX power density. Other inputs include the total number of iterations and the population size corresponding to the total number of particles in the swarm. Upon definition of these inputs, each particle

in the swarm is initialized at random within the search space, and each particle is given an initial position and velocity value. Solving for the objective function provides a fitness for each particle in the population for the given iteration.

Each particle's velocity and position are updated in the subsequent iteration by utilizing key information from its personal and the population's (global) experience. pb_i is the minimum value of fitness achieved by the given particle (personal best) until the current iteration, and gb is the minimum value of fitness achieved in the entire population (global best) through the current iteration. The velocity of each particle in the subsequent iteration is determined by three factors.

Particle velocity:

$$v_i(t+1) = c_1 r_1 \left[pb_i(t) - x_i(t)\right] + c_2 r_2 \left[gb(t) - x_i(t)\right] + w v_i(t) \tag{5.2}$$

Particle position:

$$x_i(t+1) = x_i(t) + v_i(t+1) \tag{5.3}$$

where t is the current iteration number and i is the particle number. The 1st term in the right side of Eq. 5.2 is the exploitation term which helps the particles move towards the local minimum. In other words, this term helps calculate how much the particle should move towards the individual's current best location based on personal experience. The 2nd term in Eq. 5.2 is the exploration term which helps the particles move towards the global minimum. In other words, this term helps calculate how much the particle should move towards the current global best location based on the experience of its peers. The 3rd term in Eq. 5.2 is the momentum of the current particle.

w, c_1, and c_2 in Eq. 5.2 are the key control parameters in the PSO algorithm. w is the inertia weight of the particle and a value of $w > 1$ typically indicates that the particle explores (searches globally) the search space, while a lower value ($w << 1$) means that the particle exploits (searches locally) the search space. In the past, researchers typically utilized a constant value of $w = 1$. More recently, others have shown that gradually decreasing w from 0.9 to 0.4 as the iteration number increases produces globally optimal solutions [139, 140]. In this paper, inertia weight linearly decreases as a function of iteration number from 0.9 to 0.4:

$$w_t = \left[(w_{max} - w_{min}) \times \frac{(t_{max} - t)}{(t_{max})}\right] + w_{min} \tag{5.4}$$

The values of acceleration constants, c_1 and c_2, govern the extent to which a particle moves towards the personal best or global best. c_1 and c_2 modulate the contributions of the social and cognitive terms, and $c_1 = c_2 = 2$ works well for most applications [135, 139, 141]. Careful selection of these parameters (w,c_1, and c_2) and maintaining an adequate population size and total number of iterations will ensure that the PSO algorithm reliably predicts a globally optimal solution. This paper utilizes $c_1 = c_2 = 2$, a population size of $N = 50$, and a total number of iterations of $t_{max} = 1000$. A flowchart of the PSO routine for minimization of an objective function is provided in Fig. 5.1.

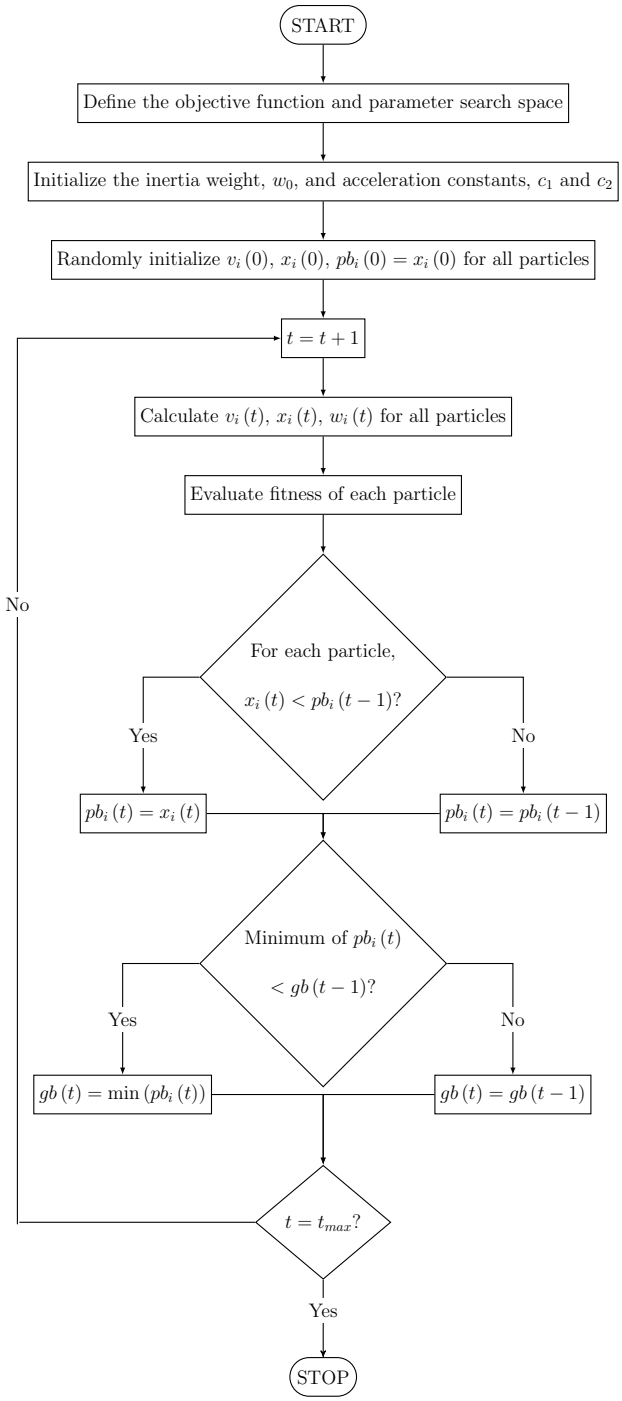

Figure 5.1: Flowchart of particle swarm optimization algorithm for minimization of an objective function.

5.3 Cost model

Accurate capital cost estimates of thermal components in the design stages is essential in predicting the feasibility of the component. Modeling of capital costs for MT-STHXs involves labor and procurement costs of various subcomponents. The form of the cost model developed in this paper is:

$$C_{cap} = [\text{A} \times \text{HX weight [kg]}] + \left[\text{B} \times \frac{\text{\# of U-tubes}}{\text{Tube OD [mm]}}\right] + [\text{C} \times \text{\# of U-tubes}] + \left[\text{D} \times \frac{\text{\# of U-tubes}}{\text{HX length [m]}}\right] + [\text{E} \times \text{\# of baffles} \times \text{\# of U-tubes}] + \text{F} \quad (5.5)$$

In Eq. 5.5, the 1st term on the right side represents the total cost of raw materials which is a function of total MT-STHX weight. The 2nd term provides the cost of tubes; this cost is inversely proportional to the tube OD because the manufacturing cost of tubes of larger diameters is less expensive than that of microtubes. The 3rd, 4th, and 5th terms on the right side of Eq. 5.5 represent the labor cost of manufacturing or assembly of various components of the MT-STHX. The 3rd term provides the cost of assembling and joining the tubes to the header, while the 5th term involves the labor cost of slotting the tubes into the baffles. The 4th term provides an estimate for the labor cost of bending the U-tubes while the 6th term captures the fixed costs of manufacturing the shell, longitudinal baffle, sealing strips, manifolds, and ports of the MT-STHX.

The coefficients A through F depend on the configuration of MT-STHX, solid material, and joining processes utilized. Eq. 5.5 provides a generic form of the cost function to compute capital cost of MT-STHXs, and careful selection of the coefficients can help estimate the cost with reasonable accuracy. The configuration of the MT-STHX shown in Fig. 3.1 is selected

here, and Haynes 282 is utilized as the solid material with supercritical CO_2 as the working fluid for both streams. For this work, the following values for the coefficients are used to compute MT-STHX total capital cost: A = 255 \$/kg, B = 5 \$·mm, C = 14 \$, D = 2 \$·m, E = 2 \$, and F = 4,000 \$.

5.4 Results and Discussion

Heat exchangers designed for use in aerospace applications are optimized with two key objectives in mind: minimization of cost and maximization of power density. Power density is a measure of the waste heat recovered by the HX per unit mass and is given by:

$$\text{HX power density} = \frac{\text{HX capacity [kW]}}{\text{HX weight [kg]}} \tag{5.6}$$

The total weight of MT-STHXs is computed as a summation of individual components such as the U-tubes, headers, baffles, shell, manifolds, ports, and longitudinal baffle. By utilizing the cost model, two sets of optimization studies have been performed using a PSO routine with minimization of cost (cost optimized) and maximization of power-density (PD-optimized) as the objectives. Optimal designs are obtained for eight MT-STHX capacities ranging from 50 kW to 3 MW. Five design parameters are optimized, and the search space of the problem is provided in Table. 5.1. The mass flow rate is varied to achieve different MT-STHX capacities, and constraints are set to ensure that the pressure drops for both flow streams do not exceed 2% of the inlet value. In order to achieve a given MT-STHX capacity, the MT-STHX length is treated as a floating parameter. With $N = 50$ and $t_{max} = 1,000$ as the PSO control parameters, 50,000 MT-STHX designs are searched for each MT-STHX capacity to optimize a given objective before the optimal design is obtained.

Table 5.1: Parameter search space for the optimizations.

Parameter	Search space
Tube OD [mm]	1.0 - 5.0
Transverse pitch/Tube OD	1.5 - 6.0
Longitudinal pitch/Tube OD	1.5 - 6.0
Number of U-tubes	20 - 12,000
Number of baffles	0 - 16

A demonstration of the PSO process is provided in Fig. 5.2 for the 3 MW power-density optimization case. The figure illustrates the exploration of particles over the entire search space, and as the iterations increase, the particles exploit the search space more locally (closer to the global optimum) in search of the optimal design. A similar trend appears for all the optimization cases and MT-STHX capacities in this study. The search space of all parameters is generally searched continuously except for the number of baffles, which is searched discretely in multiples of 2 due to the MT-STHX configuration adopted in that a baffle on one side of the MT-STHX has an accompanying pair on the other side of the MT-STHX.

Solution convergence of the various MT-STHX capacities for both the power density and cost optimization is shown in Fig. 5.3. All solutions generally converge well with the optimal design not having changed for approx. 300 iterations or more. Geometric details, cost estimate, and performance metrics of the optimal MT-STHX designs for both cost and power-density optimized cases are summarized in Tables 5.2 and 5.3. As the capacity of the

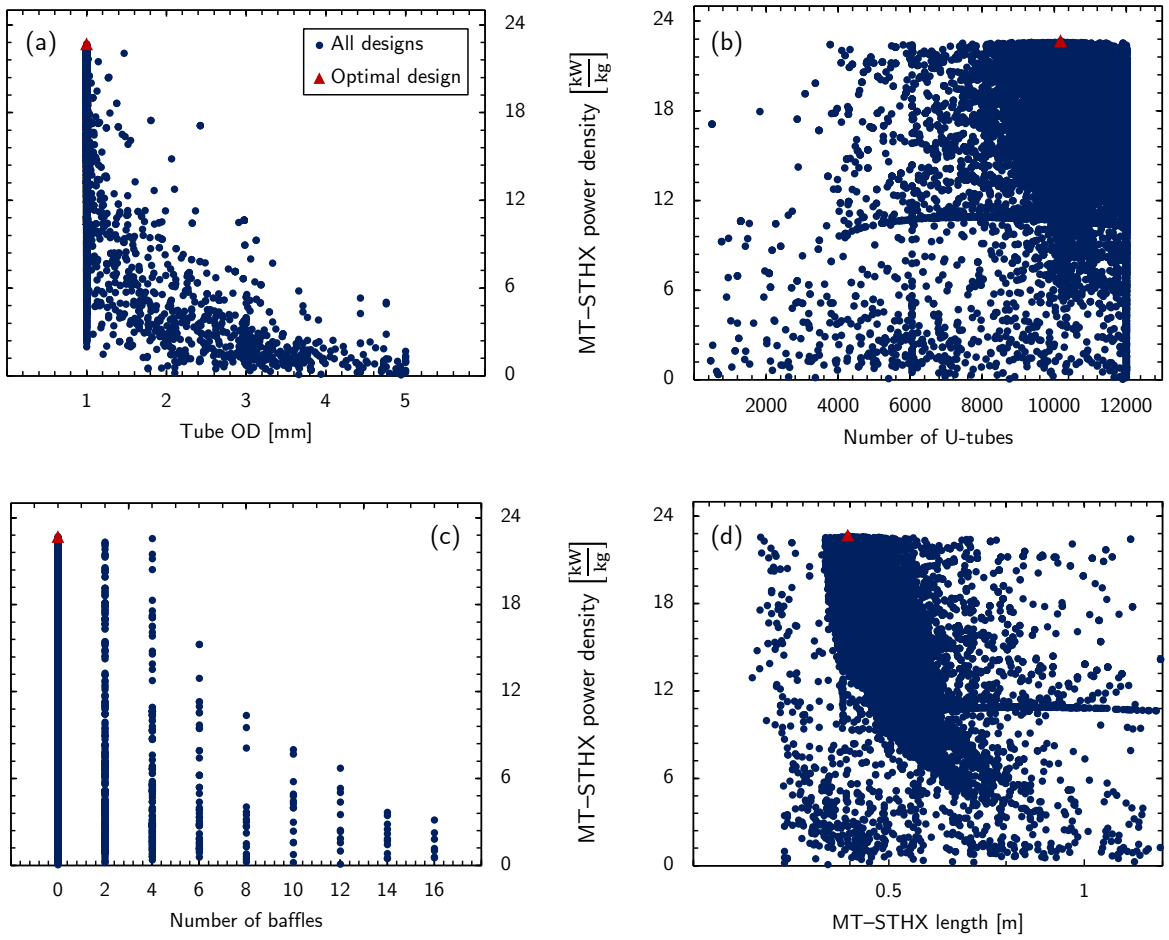

Figure 5.2: Demonstration of particle motion in the PSO routine for the 3 MW power-density optimization case.

MT-STHX increases, its estimated capital cost also increases. In order to compare the costs of optimal MT-STHX designs with varying capacities, the cost is normalized by the thermal conductance of the MT-STHX, UA, in units W/K. Conductance is a measure of the ability of the heat exchanger to transfer heat and is a function of the temperatures of both flow streams and the heat transfer rate between the solid material and the two fluid streams.

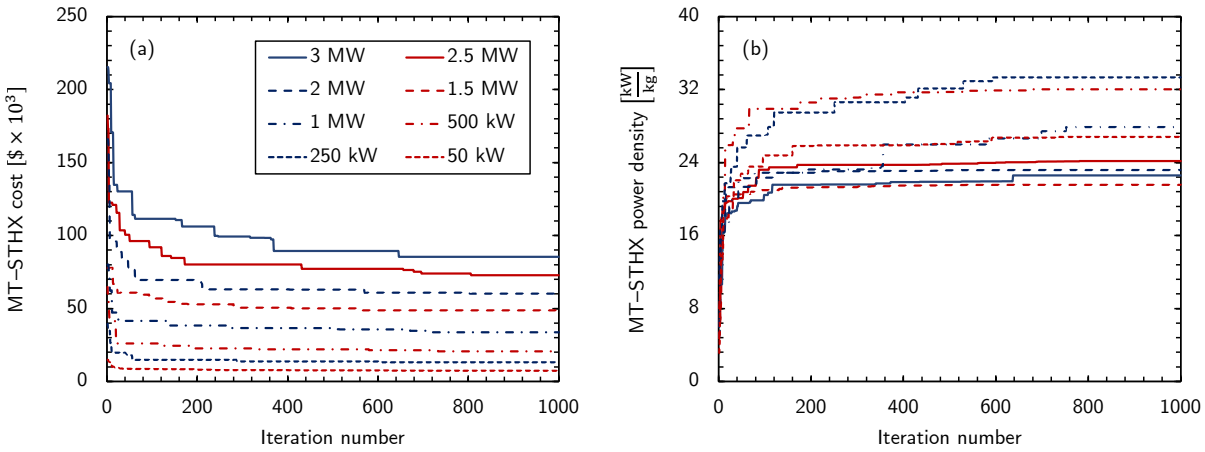

Figure 5.3: Convergence of solution for (a) cost optimized and (b) power-density optimized MT-STHX designs.

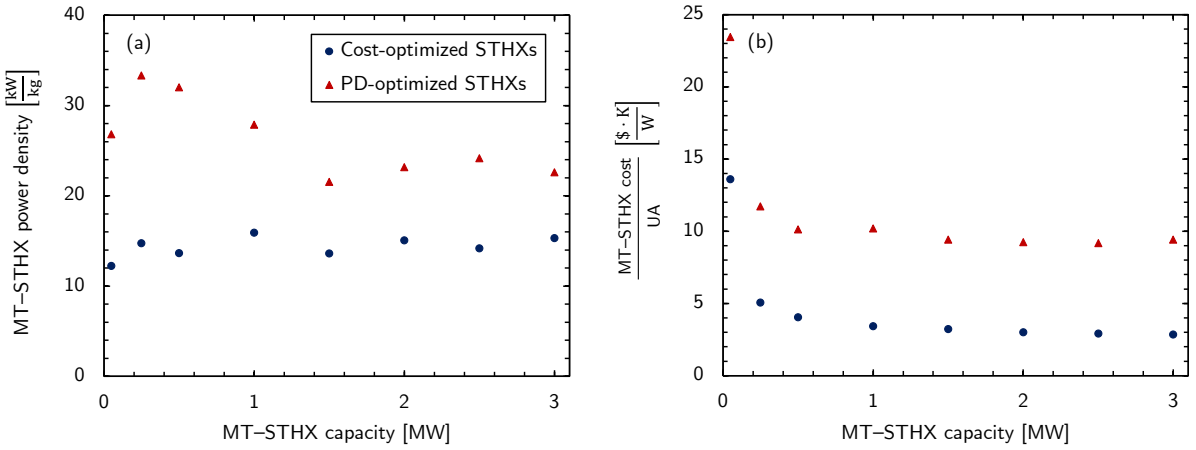

Figure 5.4: (a) MT-STHX power density and (b) MT-STHX total cost per UA of the cost optimized and power-density optimized designs as a function of MT-STHX capacity.

Table 5.2: Design details of the cost optimized MT-STHXs.

Capacity	Tube OD [mm]	Number of U-tubes	MT-STHX length [m]	Number of baffles	Power density [kW/kg]	Cost [$]
50 kW	1.892	36	0.55	14	12.2	6,795
250 kW	2.235	138	0.678	6	14.7	12,684
500 kW	2.32	252	0.772	4	13.6	20,195
1 MW	2.288	520	0.737	4	15.9	34,197
1.5 MW	2.468	730	0.888	2	13.6	48,521
2 MW	2.439	981	0.872	2	15.0	59,986
2.5 MW	2.615	1071	0.944	2	14.2	72,765
3 MW	2.472	1408	0.889	2	15.3	85,417

Table 5.3: Design details of the power-density optimized MT-STHXs.

Capacity	Tube OD [mm]	Number of U-tubes	MT-STHX length [m]	Number of baffles	Power density [kW/kg]	Cost [$]
50 kW	1	162	0.206	8	26.8	11,726
250 kW	1	666	0.248	4	33.3	29,283
500 kW	1	1410	0.275	2	32.0	50,674
1 MW	1	2926	0.272	2	27.9	101,998
1.5 MW	1	5063	0.436	0	21.5	141,260
2 MW	1	6650	0.411	0	23.2	184,864

Capacity	Tube OD [mm]	Number of U-tubes	MT-STHX length [m]	Number of baffles	Power density [$^{kW}/_{kg}$]	Cost [$]
2.5 MW	1	8264	0.396	0	24.2	229,353
3 MW	1	10171	0.395	0	22.6	282,852

Fig. 5.4 provides a comparison of the power density and cost for the various MT-STHX capacities of the power density and cost optimized designs. Table. 5.3 indicates that all power-density optimized designs have a tube OD of 1 mm. As the tube diameter decreases, the volume and weight of the MT-STHXs decreases for a given MT-STHX capacity. Due to the inverse relationship of weight with power density for a given MT-STHX capacity, the power density of the MT-STHX increases. To achieve the same MT-STHX capacity with smaller tube diameters, the number of U-tubes in the MT-STHX must increase to create sufficient area of heat transfer. Increased power density is not always preferred, as the increase in number of tubes corresponds to higher tube manufacturing, procurement, and joining costs. This trend is apparent for both the cost and power-density optimized designs as the number of U-tubes in the optimal designs increase with an increase in the MT-STHX capacities.

The tube diameter of the cost optimized designs is larger than that for the power-density optimized designs. When optimizing for minimization of MT-STHX cost, the expenses incurred by manufacturing, procuring, and joining these tubes need to be minimized. This increase in tube diameter corresponds to a reduction in the number of U-tubes of the optimal MT-STHX of a given thermal capacity as heat transfer area is directly proportional to both

tube diameter and number of tubes. A trend common to both sets of optimized designs is that the number of baffles decreases as MT-STHX capacity increases. The power-density optimized designs for MT-STHXs with 1.5 MW capacity and higher have no baffles in the flow stream but contain only one longitudinal baffle. This implies that the external flow has only two shell-side passes - one flow pass perpendicular to the tube bundle on one side of the MT-STHX and another flow pass on the opposite side of the MT-STHX.

The power density of the cost optimized designs is around 12-16 kW/kg, with the 1 MW optimal design having the highest power density of 15.9 kW/kg and the 50 kW design having the lowest power density of 12.2 kW/kg. No trend is apparent in the power density of the 50 kW to 1 MW power-density optimal designs, but the power density of the 1.5 MW to 3 MW optimal designs is 21-24 kW/kg. Among the power-density optimal designs, the 250 kW MT-STHX has the highest power density of 33.3 kW/kg, and the 1.5 MW MT-STHX has the lowest power density of about 21.5 kW/kg.

Figure 5.4 shows that the optimal MT-STHX cost per conductance follows almost an inverse relationship with MT-STHX capacity for both the cost and power-density optimized designs. The curves peak at the limit case of 50 kW, with the cost optimal design having a MT-STHX cost per conductance of about 14 $\$ \cdot \mathrm{K/W}$ and the power-density optimal design having a value of about 23 $\$ \cdot \mathrm{K/W}$. The MT-STHX cost per conductance for the larger MT-STHX capacities and asymptotes around a specific value for both the cost and power-density optimization cases. This value is around 3 $\$ \cdot \mathrm{K/W}$ for the cost optimized designs and 9.5 $\$ \cdot \mathrm{K/W}$ for the power-density optimized designs.

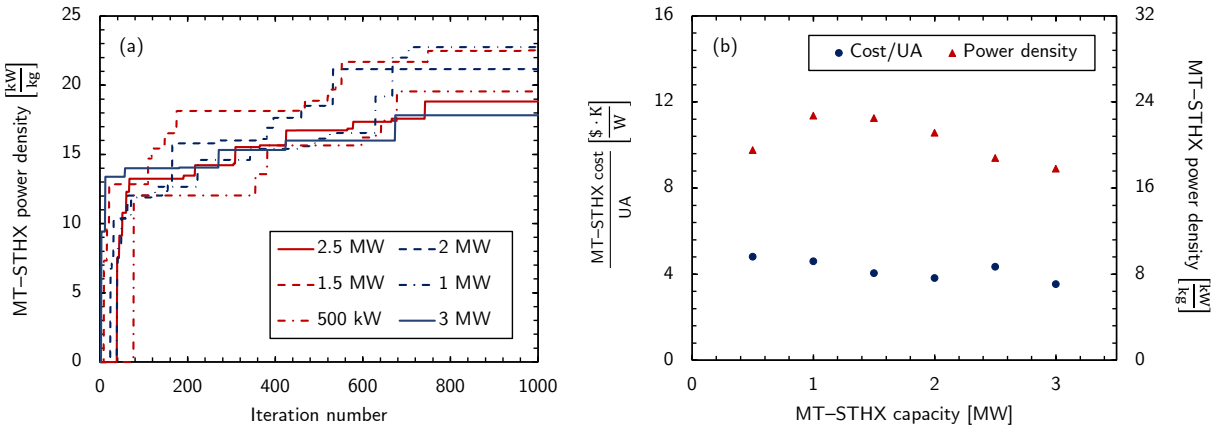

Figure 5.5: (a) Convergence of solution for PDTC-optimized MT-STHX designs and (b) MT-STHX power density of the PDTC-optimized designs as a function of MT-STHX capacity.

Table 5.4: Design details of the PDTC-optimized MT-STHXs.

Capacity	Tube OD [mm]	Number of U-tubes	MT-STHX length [m]	Number of baffles	Power density [kW/kg]	Cost [$]
500 kW	1.8	470	0.497	4	19.5	24,106
1 MW	1.654	1215	0.462	2	22.7	46,021
1.5 MW	1.618	1625	0.5	2	22.5	60,767
2 MW	1.718	1968	0.542	2	21.2	76,574
2.5 MW	1.655	2833	0.5	2	18.8	108,790
3 MW	1.888	2479	0.616	2	17.8	106,217

Eventhough the power density of the power-density optimized designs are about 2 × the cost optimized designs, their capital cost is also 2 to 3 × higher. Aerospace applica-

tions require highly compact HXs of large capacity, and HXs for any application require low cost. This calls for the simultaneous optimization of power density and cost of HXs. To address this issue and to provide a sample optimization to meet this combined objective, a MT-STHX cost per conductance less than5 $\$ \cdot \mathrm{K/W}$ constraint was set and the MT-STHX designs were optimized with maximization of power density as the objective function. With $N = 50$ and $t_{max} = 1,000$, about 50,000 MT-STHX designs were searched, and cost-constrained power-density optimized (PDTC-optimized) designs were obtained for MT-STHX capacities varying from 500 kW to 3 MW. The MT-STHXs with 50 kW and 250 kW capacity are excluded from this case as even the cost optimal designs for these capacities have an MT-STHX cost per conductance $> 5\,\$ \cdot \mathrm{K/W}$.

Fig. 5.5 illustrates the solution convergence of the PDTC-optimization case and provides comparisons among the MT-STHX cost per conductance and MT-STHX power density for the various MT-STHX capacities. The MT-STHX cost per conductance is approximately $5\,\$ \cdot \mathrm{K/W}$ for all optimal designs. As implied from the previous optimization cases, the power density of the MT-STHX is inversely proportional to cost. With maximization of power density as the objective, the optimization routine finds the best MT-STHX design at the limit of the MT-STHX cost per conductance constraint. The power densities for all optimal designs fall around 18-23 kW/kg, with the 1 MW MT-STHX having the highest power density of 22.7 kW/kg and the 3 MW MT-STHX having the lowest power density of 17.8 kW/kg. The high values of power density obtained in this paper can be attributed to the utilization of microtubes and sCO_2 as the working fluid.

Table 5.4 provides the geometric details, cost estimates, and performance metrics of the PDTC-optimized MT-STHX designs. Importantly, geometric parameters such as tube

OD, number of U-tubes, and MT-STHX length of the PDTC-optimized MT-STHX designs lie in between those of the PD-optimized and cost optimized MT-STHX designs. Due to the relatively stable value of tube OD near 1.7 mm for all optimal designs, the number of tubes increases with increasing MT-STHX capacity. This trend is maintained to prevent the violation of the pressure drop constraint of the internal flow stream. Aside from the 500 kW design, which consists of four baffles in the flow stream, all other optimal designs have only two baffles and thus a total of four shell-side passes for the external flow stream.

5.5 Conclusion

This chapter provides a promising constrained, multivariate optimization methodology and a generalized equation form to estimate the capital cost of various configurations of micro-tube shell-and-tube heat exchangers. An accurate and computationally efficient numerical model to predict MT-STHX thermohydraulic performance is utilized in conjunction with the developed cost model to perform multiple optimization studies with minimization of cost and maximization of power density as the objectives on MT-STHXs utilizing Haynes 282 as the solid material and supercritical CO_2 as the working fluid. MT-STHX designs with power density as high as 33.3 kW/kg for the power-density optimized designs and MT-STHX conductance per UA as low as 2.8 $\$ \cdot K/W$ are obtained. Despite these promising values, aerospace applications demand HXs to be optimized simultaneously for minimization of cost and maximization of power density. An optimization study is performed by constraining MT-STHX conductance per UA with maximization of power density as the objective. Power densities for these optimal designs are as high as 22 kW/kg when the MT-STHX conductance per UA was constrained to be less than 5 $\$ \cdot K/W$. This study provides

a necessary basis for cost evaluation and optimization of MT-STHXs for utilization in future applications in the aerospace industry.

Chapter 6: Closure

This thesis presents a detailed methodology for the design and optimization of sCO_2 micro-tube shell-and-tube heat exchangers. Highly accurate correlations are developed in Chapter 2 and utilized in Chapter 3 to develop a high-fidelity, computationally efficient performance prediction numerical model. The correlations and the model are both validated using CFD simulations. To provide further confidence in the model, an MT-STHX is fabricated and thermohydraulic experimental data is obtained with sCO_2 as the internal fluid and air as the external fluid. The experimental results provided in Chapter 4 show great agreement with the model predictions, further validating the model. A generalized cost model to estimate MT-STHX capital cost is developed in Chapter 5 and utilized to provide a potentially promising cost-constrained optimization methodology for future aerospace devices.

This thesis provides a justification to the usage of sCO_2 as the working fluid to increase compactness and improve performance of heat exchangers. Though MT-STHXs are a promising technology for application in the aerospace industry, insufficient experimental data exists in the literature for behavior of these heat exchangers under high temperature, high pressure sCO_2 flow. This thesis presents experimental data for these heat exchangers but with sCO_2 only as the internal fluid and operating temperatures and pressures limited to 300 °C and 100 bar. In order to achieve higher thermal cycle efficiency, the cycles require to be operated at elevated temperatures. This requires for experimental characterization of the MT-STHXs in these cycles at extreme operating conditions. Performing experiments with sCO_2 as the external working fluid and at extreme operating conditions raises safety

concerns which makes it infeasible to achieve this setup in an academic research environment. The only feasible alternative is to perform these characterization experiments in an industrial workplace but companies are less willing to make their proprietary datasets publicly available. This barrier must be overcome atleast for one test MT-STHX in order to provide a comprehensive experimental validation to the numerical model developed in this thesis aside from validation with the idealized CFD models.

The need to operate at elevated temperatures raises another important concern of the ability of these MT-STHXs to withstand long duration of unhampered operation. To address this concern, thermomechanical resilience of superalloys such as Haynes 282 that are utilized as solid materials in these MT-STHXs must be characterized and their creep, fatigue, and oxidation behavior need to be studied. Aside from the material behavior alone, the assembly technologies involved in the joining of microtubes to the header need to be ventured to achieve leak-free, stable joints that withstand prolonged exposure to high pressures and temperatures.

Another potential direction is to utilize fins on microtubes to achieve high component power densities. Fins enhance the heat transfer by providing additional heat transfer surface area and in turn reduce the volume and weight of the MT-STHX compared to bare tube MT-STHXs with the same capacity. Drastic developments need to be undergone in the processes involved in fabricating bare and finned microtubes and feasible bulk manufacturing methods must be developed. This would in turn reduce the cost of manufacturing and procurement of these microtubes and drastically reduce the capital cost of the fabricated MT-STHXs making them comparable in price to conventional MT-STHXs. With reduced cost of fabricating MT-

STHXs, most major drawbacks of conventional STHXs would be addressed and the dream of compact and highly efficient thermal cycles in aerospace systems could be realized.

Appendix A: STHX numerical model - Julia code

Calling the necessary packages

In [1]:
```
using CoolProp
using CSV
using DataFrames
using SimplePCHIP
using Dates
using SpecialFunctions
using Plots
backend(:plotly)
using LaTeXStrings
```

Function to solve for the temperature and flow field inside the HX

In [30]:
```
function HX(Dt, PiODt, PjODt, NbL, NbR, Ntt, Lk, ts, Bχ, tk, BaL, BaR, NF, Np, ṁh, T2(in), T1(in), Ratio, CaseRun, counter, Df, δfb, δft, Pf, Ct, Ncruc, ExD, P1(in), P2(in), ṁl, ttoDt, tsoDs, Ht, δsb, δtb, Nss, tsb, Bypass, FinType, NAF)

    Nk = 10 # Grid division in z-direction [-]
    Nj = 10 # Grid division in y-direction [-]

    #Call initial solid properties
    Ts = [25.0,100.0,200.0,300.0,400.0,500.0,600.0,700.0,800.0,900.0,1000.0] # Temperature of Haynes282
    Cp(s)i = [436.0,463.0,494.0,522.0,544.0,563.0,581.0,594.0,650.0,668.0,676.0] # Specific heat of Haynes282
    κsi = [10.3,12.0,14.1,16.3,18.5,20.5,22.6,24.8,26.1,27.3,28.9] # Thermal conductivity of Haynes282
    αsi = [0.00000288,0.00000315,0.00000348,0.00000381,0.00000413,0.00000444,0.00000473,0.00000509,0.00000488,0.00000498,0.00000521] # Thermal diffusivity of Haynes282
    ρsi = zeros(11) # Density of Haynes282

    for a in 1:11
        ρsi[a] = κsi[a]/(αsi[a]*Cp(s)i[a])
    end

    Cpsitp = interpolate(Ts, Cp(s)i)
    κsitp = interpolate(Ts,κsi)
    αsitp = interpolate(Ts,αsi)
    ρsitp = interpolate(Ts,ρsi)
```

The code in this chapter can be accessed and cited from GitHub and Zenodo using the DOI: 10.5281/zenodo.5117859

```
    #Parameter inputs
    Dt = Dt  # Tube outer diameter [m]
    tt = ttoDt*Dt  # Tube wall thickness [m]
    Dip = Dt - (2*tt)  # Tube inner diameter [m]
    Dint = (Dt+Dip)/2 # Intermediate tube diameter [m]
    PioDt = PioDt  # Pitch/diameter of tube in the x direction (columns
) [-]
    PjoDt = PjoDt  # Pitch/diameter of tube in the y direction (rows) [
-]
    Pi = PioDt * Dt  # Tube pitch in x direction [m]
    Pj = PjoDt * Dt  # Tube pitch in y direction [m]
    NbL = NbL # Number of baffles in the left side of the HX [-]
    NbR = NbR # Number of baffles in the right side of the HX [-]
    Ntt = Ntt # Total number of tubes on one side of the HX [-]
    ts = ts # Thickness of splitter on one side [m]
    Lk = Lk  # Height of heat exchanger [m]
    Bχ = Bχ # Percentage of shell height occupied by tubes
    Df = Df # Fin diameter [m]
    δfb = δfb # Fin base thickness [m]
    δft = δfb # Fin tip thickness (same as fin base thickness for disc
fins) [m]
    Pf = Pf # Fin pitch [m]
    Ct = Ct # Cruciform thickness
    Ch = (Dip-Ct)/2 # Cruciform height

    if Ct<0.00000001
        Ct = 0
        Ncruc = 0
        Ch = 0
    end

    testPf = 0
    if Pf<0.0000001 || (Df/Dt)<1.0001
        testPf = 1
        Df = Dt
    end

    rot = Dt/2
    rf = Df/2
    rfc = rf + (δfb/2)

    DstempA = (2*Ntt) + 1 + (2*ts/Pi) - (4*Dt/Pj) - (8*ts*Dt/(Pi*Pj))
    DstempB = ((2*Bχ/(Pi*Pj))*sqrt((1-(Bχ*Bχ))))
    DstempC = (sqrt((1-(Bχ*Bχ)))/Pi) - (2*Bχ/Pj) - ((4*Dt)*sqrt((1-(Bχ
*Bχ)))/(Pi*Pj)) - (4*Bχ*ts/(Pi*Pj))
    Ds+ = ( (-DstempC + (sqrt((DstempC*DstempC) + (4*DstempA*DstempB))
)) / (2*DstempB) )
    Ds- = ( (-DstempC - (sqrt((DstempC*DstempC) + (4*DstempA*DstempB))
)) / (2*DstempB) )
```

```
    Ds = min(Ds+,Ds-) # Shell inner diameter [m]

    if Ds<0
        Ds = max(Ds+,Ds-)
    end

    Ntj = round(Int64,(((4/Pj)*((Bx*Ds/2) - Dt)) + 1)) # Number of rows
of tubes [-]
    Nti = round(Int64,(((2/Pi)*((Ds*sqrt((1-(Bx*Bx)))/2) - ts - (Pi)))
+ 1))  # Number of columns of tubes [-]
    Lj =  (((Ntj-1) * (Pj/2))+ (2*Dt))  # Length of air flow [m]
    Li =  (((Nti-1) * (Pi/2))+(Pi))  # Width [m]

    ExD = ExD # Additional space after inclusion of side longitudinal
baffles
    NDs = Ds + ExD # New shell outer diameter after inclusion of side l
ongitudinal baffles

    tsh = tsoDs*NDs # Shell thickness [m]
    Dos = NDs + (2*tsh) # Shell outer diameter [m]
    Px = (sqrt((Pi^2)+(Pj^2)))/2 # Diagonal pitch [m]
    Lh = ((sqrt(((Ds/2)^2)-((Bx*Ds/2)^2)))) # Hexagonal cross length on
one side [m]
    Ht = Ht # Header thickness [m]
    NbT = NbL + NbR # Total number of baffles [-]

    if NF == 0
        NbT = NbL+NbR-1
    end

    Sk = zeros(NbT+2)  # Baffle spacing [m]

    geomviolate = 0

    #Check if parameters violate geometric constraints

    gap1 = Px - Dt
    if gap1<0
        geomviolate = 1
    end

    gap2 = Pi - Dt
    if gap2<0
        geomviolate = 1
    end

    gap3 = Pj - Dt
    if gap3<0
        geomviolate = 1
```

```
end

gap4 = Pi - Df
if gap4<0
    geomviolate = 1
end

gap5 = Pj - Df
if gap5<0
    geomviolate = 1
end

gap6 = Px - Df
if gap6<0
    geomviolate = 1
end

if (Pi/Dt)<=1.01
    geomviolate = 1
end

if (Pi/Df)<=1.01
    geomviolate = 1
end

if (Pj/Dt)<=1.01
    geomviolate = 1
end

if (Pj/Df)<=1.01
    geomviolate = 1
end

if (Px/Dt)<=1.01
    geomviolate = 1
end

if (Px/Df)<=1.01
    geomviolate = 1
end

if Pf<δfb
    geomviolate = 1
end

if geomviolate == 1
    @goto endit
end

#Define baffle spacing in the HX
```

```
    L_kL = L_k - (NbL*t_k)  # Length of the left side HX excluding baffle
thickness [m]
    L_kR = L_k - (NbR*t_k)  # Length of the left side HX excluding baffle
thickness [m]

    L_kRR = L_k
    if NF == 0
        L_kRR = 0
        NbT = NbL+NbR-1
        S_k[1] = (2-B_aL)*L_k/(NbL+1)
        S_k[NbL+1] = (B_aL)*L_k/(NbL+1)
        dBL = (S_k[NbL+1]-S_k[1])/NbL # the common difference between baf
fles on the left side of the HX [m]

        for dtemp in 2:NbL
            S_k[dtemp] = S_k[1] + ((dtemp-1)*dBL)
        end
    else
        S_k[1] = (2-B_aL)*L_k/(NbL+1)
        S_k[NbL+1] = (B_aL)*L_k/(NbL+1)
        S_k[NbL+2] = (B_aR)*L_kRR/(NbR+1)
        S_k[NbT+2] = (2-B_aR)*L_kRR/(NbR+1)

        dBL = (S_k[NbL+1]-S_k[1])/NbL # the common difference between baf
fles on the left side of the HX [m]
        dBR = (S_k[NbT+2]-S_k[NbL+2])/NbR # the common difference between
baffles on the right side of the HX [m]

        for dtemp in 2:NbL
            S_k[dtemp] = S_k[1] + ((dtemp-1)*dBL)
        end

        for dtemp in NbL+3:NbT+1
            S_k[dtemp] = S_k[NbL+2] + ((dtemp-NbL-2)*dBR)
        end
    end

    #Initialize thermophysical properties
    h_1i = PropsSI("H","T",(T_1(in)+273),"P",P_1(in),"CO2") # Initial Ent
halpy of sCO2 in the shell [J/kg]
    h_2i = PropsSI("H","T",(T_2(in)+273),"P",P_1(in),"CO2") # Initial Ent
halpy of sCO2 in the shell [J/kg]
    h1inew = PropsSI("H","T",(T_1(in)+273),"P",P_2(in),"CO2")
    h2inew = PropsSI("H","T",(T_2(in)+273),"P",P_2(in),"CO2")
    h1itemp = h_1i
    h2itemp = h_2i

    Q1 = abs((h1itemp-h2itemp)*ṁ_h)
    Q2 = abs((h1inew-h2inew)*ṁ_l)
```

```
    Qmax = min(Q1,Q2)

    P₁ = ones(Int(NbT+2))
    P₂ = ones(Int(NbT+2))

    a = 1
    for a in 1:(NbT+2)
        P₁[a] = P₁₍ᵢₙ₎
        P₂[a] = P₂₍ᵢₙ₎
    end

    #Variables used to define the flow correction factors
#     NF = NF # Number of folds [-]
#     Np = Np # Number of tube passes [-]
    Ncw = 0 # Number of tubes in the window [-]

    δsb = δsb # shell-to-baffle diametral clearance [-]
    lc = ((1-Bᵪ)/2)*Dₛ + (ExD/2) # Distance between the top of the baf
fle and the shell [m]
    θb = 2*acosd(1-(2*lc/NDₛ)) # angle between two radii intersected a
t the inside shell wall with the baffle cut [°]
    Asb = (π*(NDₛ-(2*tₛ))*δsb*(1-(θb/360)))/4 # shell-to-baffle leakage
flow area [m²]

    Dctl = Dₛ-(3*Dₜ) # diameter of the circle through the centers of th
e outermost tubes [m]
    θctl = 2*acosd((Dₛ-(2*(lc-(ExD/2))))/Dctl) # angle between two rad
ii intersected at the outer tube center with the baffle cut [°]
    δtb = δtb # tube-to-baffle diametral clearance [-]
    # Fw = (θctl/360) - (sind(θctl)/(2*π)) # Fw = 0 when no tubes are
in the window [-]
    Fw = 0
    Atb = (π*Dₜ*δtb*Nₜₜ*(1-Fw))/2 # tube-to-baffle leakage flow area [m²
]


    #Porosity, Specific surface are and hydraulic diameter
    XM₁ = ones(Int(Nⱼ),Int(Nₖ)) # Porosity of external sCO₂ [-]
    XM₂ = ones(Int(Nⱼ),Int(Nₖ)) # Porosity of internal sCO₂ [-]
    SW₁ = ones(Int(Nⱼ),Int(Nₖ)) # Specific surface area wetted by exte
rnal sCO₂ [1/m]
    SW₂ = ones(Int(Nⱼ),Int(Nₖ)) # Specific surface area wetted by inte
rnal sCO₂ [1/m]
    DH₁ = ones(Int(Nⱼ),Int(Nₖ)) # Hydraulic diameter of external sCO₂
[m]
    DH₂ = ones(Int(Nⱼ),Int(Nₖ)) # Hydraulic diameter of internal sCO₂
[m]
    XMₛ = ones(Int(Nⱼ),Int(Nₖ)) # Porosity of solid [-]

    θ = 0.0
```

```
    A_tot = 0.0
    V_tot = ones(Int(NbT+2))
    AtotN = 0.0

    #Gridding
    Y = ones(Int(N_j))
    Z = ones(Int(N_k))
    H_j = ones(Int(N_j))
    H_k = ones(Int(N_k))

    Y[1] = 0
    for j in 2:Int(N_j)
        Y[j] = (L_j/(N_j-1)) * (j-1)
        H_j[j-1] = Y[j]-Y[j-1]
    end
    H_j[Int(N_j)] = H_j[Int(N_j-1)]

    # Z-gridding later


    #Velocity, Reynolds number and friction factor calculation
    u_1 = ones(Int(N_j),Int(N_k)) # Hot sCO2 velocities (external flow) [
m/s]
    u_2 = ones(Int(N_j),Int(N_k)) # Cold sCO2 velocities (in tubes) [m/s]
    Re_1 = ones(Int(N_j),Int(N_k)) # Hot sCO2 Reynold numbers (external f
low) [-]
    Re_2 = ones(Int(N_j),Int(N_k)) # Cold sCO2 Reynold numbers (in tubes)
[-]
    Cd_1 = ones(Int(N_j),Int(N_k)) # Hot sCO2 drag (external flow) [-]
    Cd_2 = ones(Int(N_j),Int(N_k)) # Cold sCO2 drag (in tubes) [-]
    Conv_1 = ones(Int(N_j),Int(N_k)) # Convection heat generation (extern
al flow) [W/m^3/K]
    Conv_2 = ones(Int(N_j),Int(N_k)) # Convection heat generation (intern
al flow) [W/m^3/K]
    u_1m = ones(Int(N_j),Int(N_k)) # Maximum velocities of external flow

    T_1total = ones(Int(N_j),Int(N_k*(NbT+2)),Int(N_ti)) # Temperature of f
luid in shell [°C]
    T_2total = ones(Int(N_j),Int(N_k*(NbT+2)),Int(N_ti)) # Temperature of f
luid in tubes [°C]
    T_stotal = ones(Int(N_j),Int(N_k*(NbT+2)),Int(N_ti)) # Temperature of s
olid [°C]
    T_sototal = ones(Int(N_j),Int(N_k*(NbT+2)),Int(N_ti))
    T_sitotal = ones(Int(N_j),Int(N_k*(NbT+2)),Int(N_ti))

    T_1 = ones(Int(N_j),Int(N_k)) # Temperature of fluid in shell [°C]
    T_2 = ones(Int(N_j),Int(N_k)) # Temperature of fluid in tubes [°C]
    T_s = ones(Int(N_j),Int(N_k)) # Temperature of solid [°C]
    T_so = ones(Int(N_j),Int(N_k))
    T_si = ones(Int(N_j),Int(N_k))
```

```
    Y1 = ones(Int(Nj),Int(Nk))
    Y2 = ones(Int(Nj),Int(Nk))
    Y2o = ones(Int(Nj),Int(Nk))
    Y2i = ones(Int(Nj),Int(Nk))
    Y3 = ones(Int(Nj),Int(Nk))
    HH1 = ones(Int(Nj),Int(Nk)) # Heat transfer coefficient (external
flow) [W/m²/K]
    HH2 = ones(Int(Nj),Int(Nk)) # Heat transfer coefficient (internal
flow) [W/m²/K]
    CT1s = ones(Int(Nj),Int(Nk)) # Volumetric heat generation between e
xternal fluid and solid [W/m³/K]
    CT2s = ones(Int(Nj),Int(Nk)) # Volumetric heat generation between i
nternal fluid and solid [W/m³/K]
    GTs = ones(Int(Nj),Int(Nk))
    HTs = ones(Int(Nj),Int(Nk))
    ITs = ones(Int(Nj),Int(Nk))
    JTs = ones(Int(Nj),Int(Nk))


    AJTs = ones(Int(Nj),Int(Nk))
    BJTs = ones(Int(Nj),Int(Nk))
    CJTs = ones(Int(Nj),Int(Nk))
    AITs = ones(Int(Nj),Int(Nk))
    BITs = ones(Int(Nj),Int(Nk))
    CITs = ones(Int(Nj),Int(Nk))
    CT1 = ones(Int(Nj),Int(Nk))
    CT2 = ones(Int(Nj),Int(Nk))
    CJTss = ones(Int(Nj),Int(Nk))

    TInExt = ones(Int(NbT+2))
    TInInt = ones(Int(NbT+2))
    TOutExt = ones(Int(NbT+2))
    TOutInt = ones(Int(NbT+2))
    Tso = ones(Int(NbT+2))

    T1avgo = ones(Int(NbT+2))
    T1avgn = ones(Int(NbT+2))
    T2avgo = ones(Int(NbT+2))
    T2avgn = ones(Int(NbT+2))
    Tsoavg = ones(Int(NbT+2))

    T1ca = ones(Int(NbT+2), Nk)
    T2ca = ones(Int(NbT+2), Nj)

    AHTBi = ones(Int(NbT+2))
    AcBi = ones(Int(NbT+2))
    DhBi = ones(Int(NbT+2))
    umax = ones(Int(NbT+2))
    ReBi = ones(Int(NbT+2))
    De = ones(Int(NbT+2))
```

```
    Nf = ones(Int(NbT+2))

    ηf = ones(Int(Nⱼ),Int(Nₖ))
    SW₁mod = ones(Int(Nⱼ),Int(Nₖ))

    mfint = 0.0
    SW₂mod = ones(Int(Nⱼ),Int(Nₖ))
    ηfint = ones(Int(Nⱼ),Int(Nₖ))

    mf = 0.0
    C2f = 0.0
    Numf1 = 0.0
    Numf2 = 0.0
    Denf1 = 0.0
    Denf2 = 0.0
    Pmin = 0.0
    Lccpf = 0.0

    ΔP₁ =0.0
    η₁ = 0.0
    F₁ = 0.0
    PP₁ =0.0
    ΔP₂ =0.0
    η₂ = 0.0
    F₂ = 0.0
    PP₂ =0.0
    PPt =0.0

    ΔP₁t=0.0
    F₁t =0.0
    PP₁t=0.0
    ΔP₁w=0.0
    ΔPw =0.0

    ΔP₂t=0.0
    F₂t =0.0
    PP₂t=0.0

    tempT1 = 0.0
    tempT2 = 0.0

#     uoav=0.0
#     uiav=0.0
#     foav=0.0
#     fiav=0.0
#     Dhoav=0.0
#     Dhiav=0.0
#     ρoav=0.0
#     ρiav=0.0
```

```
#     dP2 = 0.0
#     Ltemp = 0.0

    ϕs = ones(Int(NbT+2))
    ρi = ones(Int(NbT+2))
    ρo = ones(Int(NbT+2))
    ui = ones(Int(NbT+2))
    uo = ones(Int(NbT+2))
    fi = ones(Int(NbT+2))
    fo = ones(Int(NbT+2))
    Dhi = ones(Int(NbT+2))
    Dho = ones(Int(NbT+2))
    Rei = ones(Int(NbT+2))
    Reo = ones(Int(NbT+2))
    hiav = ones(Int(NbT+2))
    hoav = ones(Int(NbT+2))
    hi = ones(Int(Nj))
    ho = ones(Int(Nk))
    hc1 = ones(Int(NbT+2))
    hc2 = ones(Int(NbT+2))
    Tsext = ones(Int(NbT+2))
    Tsavg = ones(Int(NbT+2))
    Tsint = ones(Int(NbT+2))
    ufr = ones(Int(NbT+2))
    tempTprev = 0.0

    h1i = 0.0
    Cp(1i) = 0.0
    μ1i = 0.0
    ρ1i = 0.0
    ν1i = 0.0
    κ1i = 0.0
    α1i = 0.0

    h2i = 0.0
    Cp(2i) = 0.0
    μ2i = 0.0
    ρ2i = 0.0
    ν2i = 0.0
    κ2i = 0.0
    α2i = 0.0

    Qj1 = 0.0
    Qk1 = 0.0
    T1(av) = 0.0
    T2(av) = 0.0
    Qj2 = 0.0
    Qk2 = 0.0
    ϵ = 0.0
    ϵ1 = 0.0
```

```
    ϵ₂ = 0.0
    ϵₛ = 0.0
    Nu₁ = 0.0
    Nu₂ = 0.0
    HBₖ₂ = 0
    HBₖ₂ₘ = 0
    HBⱼ₂ = 0
    HBⱼ₂ₘ = 0

    Gtemp1 = 0.0
    Htemp1 = ones(Int(Nⱼ),Int(Nₖ))
    Itemp1 = 0.0
    Jtemp1 = ones(Int(Nⱼ),Int(Nₖ))
    GTso1 = ones(Int(Nⱼ),Int(Nₖ))
    ITso1 = ones(Int(Nⱼ),Int(Nₖ))

    ζl = ones(Int(NbT+2))
    ζb = ones(Int(NbT+2))
    As = ones(Int(NbT+2))
    ζs = 2
    Aw = 0.0

    DF = 0.0
    tubeP = ones(Int(NbT+2))
    windowP = ones(Int(NbT+1))

    ΔP₁tube = 0.0
    ΔP₁tube = ΔP₁ₜ

    ΔPtur = 0.0
    ΔPce = 0.0
    PPₜ = 0.0

    uturn = ones(Int(NbT+1))
    uhead = ones(Int(NbT+1))
    uheadPr = ones(Int(NbT+1))
    Pratio = ones(Int(NbT+1))
    PRAv = 0.0
    IntTubeP = 0.0

    DPInt = ones(Int(NbT+2))

    ΔPiu = ones(Int(Nₜᵢ)) # Pressure drop in each column of tubes for
internal flow [Pa]
    ΔPiutot = 0.0 # Average pressure drop in u-bend region for interna
l flow [Pa]
    Rbend = ones(Int(Nₜᵢ)) # Radius of bend for each column of tube [m
]
    kbend = ones(Int(Nₜᵢ)) # Bend factor for each row of tube [-]
    RbendoDtint = ones(Int(Nₜᵢ)) # Ratio of radius of bend to internal
```

```
tube diameter [-]

    kbendxdata = [0.5,0.517,0.537,0.57,0.6,0.621,0.643,0.689,0.733,0.7
8,0.832,0.886,0.952,1.05,1.15,1.23,1.34,1.53,1.7,1.91,2.11,2.37,2.62,3
.26,3.71,4.32,5.1,6.32,7.33,8.1,8.93,9.7,9.97,10,11,12,13,14,15,16,17,
18,19,20,21,22,23,24,25,26,27,28,29,30,31,32,33,34,35,36,37,38,39,40,4
1,42,43,44,45,46,47,48,49,50,51,52,53,54,55,56,57,58,59,60,61,62,63,64
,65,66,67,68,69,70,71,72,73,74,75,76,77,78,79,80,81,82,83,84,85,86,87,
88,89,90,91,92,93,94,95,96,97,98,99,100,101,102,103,104,105,106,107,10
8,109,110,111,112,113,114,115,116,117,118,119,120,121,122,123,124,125,
126,127,128,129,130,131,132,133,134,135,136,137,138,139,140,141,142,14
3,144,145,146,147,148,149,150,151,152,153,154,155,156,157,158,159,160,
161,162,163,164,165,166,167,168,169,170,171,172,173,174,175,176,177,17
8,179,180,181,182,183,184,185,186,187,188,189,190,191,192,193,194,195,
196,197,198,199,200,201,202,203,204,205,206,207,208,209,210,211,212,21
3,214,215,216,217,218,219,220,221,222,223,224,225,226,227,228,229,230,
231,232,233,234,235,236,237,238,239,240,241,242,243,244,245,246,247,24
8,249,250,251,252,253,254,255,256,257,258,259,260,261,262,263,264,265,
266,267,268,269,270,271,272,273,274,275,276,277,278,279,280,281,282,28
3,284,285,286,287,288,289,290,291,292,293,294,295,296,297,298,299,300,
301,302,303,304,305,306,307,308,309,310,311,312,313,314,315,316,317,31
8,319,320,321,322,323,324,325,326,327,328,329,330,331,332,333,334,335,
336,337,338,339,340,341,342,343,344,345,346,347,348,349,350,351,352,35
3,354,355,356,357,358,359,360,361,362,363,364,365,366,367,368,369,370,
371,372,373,374,375,376,377,378,379,380,381,382,383,384,385,386,387,38
8,389,390,391,392,393,394,395,396,397,398,399,400,401,402,403,404,405,
406,407,408,409,410,411,412,413,414,415,416,417,418,419,420,421,422,42
3,424,425,426,427,428,429,430,431,432,433,434,435,436,437,438,439,440,
441,442,443,444,445,446,447,448,449,450,451,452,453,454,455,456,457,45
8,459,460,461,462,463,464,465,466,467,468,469,470,471,472,473,474,475,
476,477,478,479,480,481,482,483,484,485,486,487,488,489,490,491,492,49
3,494,495,496,497,498,499,500,501,502,503,504,505,506,507,508,509,510,
6000]
    kbendydata = [1.1,1.05,1.01,0.928,0.876,0.84,0.799,0.743,0.698,0.6
57,0.613,0.58,0.547,0.498,0.463,0.44,0.414,0.381,0.357,0.335,0.317,0.2
95,0.284,0.259,0.245,0.229,0.21,0.189,0.173,0.174,0.173,0.173,0.173,0.
173,0.173,0.173,0.173,0.173,0.173,0.173,0.173,0.173,0.173,0.173,0.173,
0.173,0.173,0.173,0.173,0.173,0.173,0.173,0.173,0.173,0.173,0.173,0.17
3,0.173,0.173,0.173,0.173,0.173,0.173,0.173,0.173,0.173,0.173,0.173,0.
173,0.173,0.173,0.173,0.173,0.173,0.173,0.173,0.173,0.173,0.173,0.173,
0.173,0.173,0.173,0.173,0.173,0.173,0.173,0.173,0.173,0.173,0.173,0.17
3,0.173,0.173,0.173,0.173,0.173,0.173,0.173,0.173,0.173,0.173,0.173,0.
173,0.173,0.173,0.173,0.173,0.173,0.173,0.173,0.173,0.173,0.173,0.173,
0.173,0.173,0.173,0.173,0.173,0.173,0.173,0.173,0.173,0.173,0.173,0.17
3,0.173,0.173,0.173,0.173,0.173,0.173,0.173,0.173,0.173,0.173,0.173,0.
173,0.173,0.173,0.173,0.173,0.173,0.173,0.173,0.173,0.173,0.173,0.173,
0.173,0.173,0.173,0.173,0.173,0.173,0.173,0.173,0.173,0.173,0.173,0.17
3,0.173,0.173,0.173,0.173,0.173,0.173,0.173,0.173,0.173,0.173,0.173,0.
173,0.173,0.173,0.173,0.173,0.173,0.173,0.173,0.173,0.173,0.173,0.173,
0.173,0.173,0.173,0.173,0.173,0.173,0.173,0.173,0.173,0.173,0.173,0.17
```

```
3,0.173,0.173,0.173,0.173,0.173,0.173,0.173,0.173,0.173,0.173,0.173,0.
173,0.173,0.173,0.173,0.173,0.173,0.173,0.173,0.173,0.173,0.173,0.173,
0.173,0.173,0.173,0.173,0.173,0.173,0.173,0.173,0.173,0.173,0.173,0.17
3,0.173,0.173,0.173,0.173,0.173,0.173,0.173,0.173,0.173,0.173,0.173,0.
173,0.173,0.173,0.173,0.173,0.173,0.173,0.173,0.173,0.173,0.173,0.173,
0.173,0.173,0.173,0.173,0.173,0.173,0.173,0.173,0.173,0.173,0.173,0.17
3,0.173,0.173,0.173,0.173,0.173,0.173,0.173,0.173,0.173,0.173,0.173,0.
173,0.173,0.173,0.173,0.173,0.173,0.173,0.173,0.173,0.173,0.173,0.173,
0.173,0.173,0.173,0.173,0.173,0.173,0.173,0.173,0.173,0.173,0.173,0.17
3,0.173,0.173,0.173,0.173,0.173,0.173,0.173,0.173,0.173,0.173,0.173,0.
173,0.173,0.173,0.173,0.173,0.173,0.173,0.173,0.173,0.173,0.173,0.173,
0.173,0.173,0.173,0.173,0.173,0.173,0.173,0.173,0.173,0.173,0.173,0.17
3,0.173,0.173,0.173,0.173,0.173,0.173,0.173,0.173,0.173,0.173,0.173,0.
173,0.173,0.173,0.173,0.173,0.173,0.173,0.173,0.173,0.173,0.173,0.173,
0.173,0.173,0.173,0.173,0.173,0.173,0.173,0.173,0.173,0.173,0.173,0.17
3,0.173,0.173,0.173,0.173,0.173,0.173,0.173,0.173,0.173,0.173,0.173,0.
173,0.173,0.173,0.173,0.173,0.173,0.173,0.173,0.173,0.173,0.173,0.173,
0.173,0.173,0.173,0.173,0.173,0.173,0.173,0.173,0.173,0.173,0.173,0.17
3,0.173,0.173,0.173,0.173,0.173,0.173,0.173,0.173,0.173,0.173,0.173,0.
173,0.173,0.173,0.173,0.173,0.173,0.173,0.173,0.173,0.173,0.173,0.173,
0.173,0.173,0.173,0.173,0.173,0.173,0.173,0.173,0.173,0.173,0.173,0.17
3,0.173,0.173,0.173,0.173,0.173,0.173,0.173,0.173,0.173,0.173,0.173,0.
173,0.173,0.173,0.173,0.173,0.173,0.173,0.173,0.173,0.173,0.173,0.173,
0.173,0.173,0.173,0.173,0.173,0.173,0.173,0.173,0.173,0.173,0.173,0.17
3,0.173,0.173,0.173,0.173,0.173,0.173,0.173,0.173,0.173,0.173,0.173,0.
173,0.173,0.173,0.173,0.173,0.173,0.173,0.173,0.173,0.173,0.173,0.173]
    kbenddata = interpolate(kbendxdata, kbendydata)

    DiffPtempInt = 100.0
    DiffPtempExt = 100.0

    u1(av) = 0.0
    u2(av) = 0.0

    Qext = 0.0
    Qint = 0.0
    FT1i = 0.0

    Dotl = 0.0
    Acr = ones(Int(NbT+2))

    rs = 0.0
    rlm = ones(Int(NbT+2))
    pcorr = 0.0

    wp = 0.0
    Abp = ones(Int(NbT+2))
```

```
    Nss = Nss # Number of sealing strip pairs
    Ncc = 0

    rb = ones(Int(NbT+2))
    Nss⁺ = 0.0
    Dcorr = 3.7 # 4.5 for Re<100

    Fc = 0.0
    Ccorr = 1.25 # 1.35 for Re<100

    Li⁺ = 1 # (equation changes when baffle spacing varies)
    Lo⁺ = 1 # (equation changes when baffle spacing varies)
    ncorr = 0.6 # 0.33 for laminar flow

    Jc = 0.0
    Jl = ones(Int(NbT+2))
    Jb = ones(Int(NbT+2))
    Js = 0.0
    Jr = 0.0

    Jcorr = ones(Int(NbT+2))

    c=0

    P1tempO = P1(in)
    P2tempO = P2(in)

    Diff3 = 100.0

    Effo = 0.00
    Effn = 0.50
    Efft = 1.00

    while DiffPtempInt>0.01 || DiffPtempExt>0.01

        @label start
        while Diff3>0 || (-1*Diff3)>1

            Fh1i = h1itemp - (Effn*Qmax/ṁh)
            FT1i = PropsSI("T","H",Fh1i,"P",P1(in),"CO2")-273


            for d in 1:NbT+2

                θ = 2*atand((Lj/(2*Lh)))
                AtotN = ( ((θ*π*NDs*NDs)/(4*360)) + ((Lh*Lj)/2) - (ts*Lj) )

                if ExD < 0
```

```
                    Atot = ( ((θ*π*NDs*NDs)/(4*360)) + ((Lh*Lj)/2) - (ts*
Lj) )
                    Vtot[d] = Atot * Sk[d]
                else
                    Atot = Li*Lj
                    Vtot[d] = Atot * Sk[d]
                end

                if testPf == 1
                    Pf = Sk[d]
                    δfb = 0
                    Df = Dt
                end

                Nf[d] = round(Int64,(Sk[d]/Pf)) # Number of fins in on
e unit cell [-]

                if Nf[d]<1
                    Pf = Sk[d]
                    δfb = 0
                    Df = Dt
                    Nf[d]=1
                end

                Pmin = Pi # minimum flow path [m]

                if FinType == 0 || FinType == 1

                    for k in 1:Int(Nk)
                        for j in 1:Int(Nj)
                            XM1[j,k] = 1 - (((Ntt*Sk[d]*π*Dt*Dt) + (Nf[d]
*Ntt*π*((Df*Df)-(Dt*Dt))*δfb))/ (4*Vtot[d]))
                            XM2[j,k] = (((Ntt*π*Dip*Dip*Sk[d]) - (Ntt*4*N
cruc*Ch*Ct*Sk[d]) - (Ntt*4*Ct*Ct*Sk[d]))/(4*Vtot[d]))
                            SW1[j,k] = (((Ntt*Nf[d]*2*π*Dt*(Pf-δfb)) + (
Ntt*Nf[d]*2*π*Df*δfb) + (Ntt*Nf[d]*π*((Df*Df)-(Dt*Dt)))) / (2*Vtot[d]))
                            SW2[j,k] = ((Ntt*π*Dip*Sk[d]) - (Ntt*Ncruc*Sk
[d]*Ct) + (Ntt*2*Ncruc*Ch*Sk[d])) / (Vtot[d])
                            DH1[j,k] = (4.0*XM1[j,k])/SW1[j,k]
                            DH2[j,k] = (4.0*XM2[j,k])/SW2[j,k]
                            XMs[j,k] = 1.0 - (XM1[j,k]+XM2[j,k])
                        end
                    end

                    ϕs[d] = XMs[1,1]

                    AHTBi[d] = Ntt*(((Nf[d]*π*Dt*(Pf-δfb)) + (Nf[d]*π*Df
*δfb) + (Nf[d]*π*((Df*Df)-(Dt*Dt))/2))) # Area of heat transfer as deri
ved by Biery [m²]
```

```
                    Pmin = Pi # minimum flow path [m]
                    if (Pi+Dt)<=(2*Px)
                        Pmin = Pi
                        AcBi[d] = 0.5*(Nti+1)*(((Nf[d]*(Pmin-Dt)*Pf) -
(Nf[d]*(Df-Dt)*δfb))) # Cross-section area as defined by Biery [m]
                    else
                        Pmin = Px
                        AcBi[d] = 0.5*(Nti+1)*2*((Nf[d]*(Pmin-Dt)*Pf) -
(Nf[d]*(Df-Dt)*δfb)) # Cross-section area as defined by Biery [m]
                    end


                elseif FinType == 2

                    for k in 1:Int(Nk)
                        for j in 1:Int(Nj)
                            XM1[j,k] = 1 - (Ntt*((2*π*Dt*Dt*Sk[d]) + (Nf[
d]*NAF*π*δfb*δfb*(Df-Dt)))/(8*Vtot[d]))
                            XM2[j,k] = (((Ntt*π*Dip*Dip*Sk[d]) - (Ntt*4*N
cruc*Ch*Ct*Sk[d]) - (Ntt*4*Ct*Ct*Sk[d]))/(4*Vtot[d]))
                            SW1[j,k] = (((Ntt*Nf[d]*2*π*Dt*Pf) + (Ntt*Nf[
d]*NAF*π*(Df-Dt)*δfb)) / (2*Vtot[d]))
                            SW2[j,k] = ((Ntt*π*Dip*Sk[d]) - (Ntt*Ncruc*Sk
[d]*Ct) + (Ntt*2*Ncruc*Ch*Sk[d])) / (Vtot[d])
                            DH1[j,k] = (4.0*XM1[j,k])/SW1[j,k]
                            DH2[j,k] = (4.0*XM2[j,k])/SW2[j,k]
                            XMs[j,k] = 1.0 - (XM1[j,k]+XM2[j,k])
                        end
                    end

                    ϕs[d] = XMs[1,1]

                    AHTBi[d] = Ntt*((Nf[d]*π*Dt*Pf) + (Nf[d]*NAF*π*(Df-D
t)*δfb)) # Area of heat transfer as derived by Biery [m²]

                    Pmin = Pi # minimum flow path [m]
                    if (Pi+Dt)<=(2*Px)
                        Pmin = Pi
                        AcBi[d] = 0.5*(Nti+1)*((Nf[d]*(Pmin-Dt)*Pf) - (
Nf[d]*(Df-Dt)*δfb)) # Cross-section area as defined by Biery [m]
                    else
                        Pmin = Px
                        AcBi[d] = 0.5*(Nti+1)*2*((Nf[d]*(Pmin-Dt)*Pf) -
(Nf[d]*(Df-Dt)*δfb)) # Cross-section area as defined by Biery [m]
                    end

                end

                DhBi[d] = (2*AcBi[d]*Pj*(Ntj+1))/(AHTBi[d]) # Hydrauli
c diameter as defined by Biery [m]
```

```
                De[d] = sqrt(((Dt*Dt) + (((Df*Df)-(Dt*Dt))*δfb/Pf))) # E
ffective diameter as defined by Kaiyuan [m]

                Z[1] = 0
                for k in 2:Int(Nk)
                    Z[k] = (Sk[d]/(Nk-1)) * (k-1)
                    Hk[k-1] = Z[k]-Z[k-1]
                end
                Hk[Int(Nk)] = Hk[Int(Nk-1)]

                #Correction factor for HTC and ΔP in the shell-side
                Dotl = Ds-(2*Dt) # diameter of the circle through the e
nds of the outermost tubes [m]
                Acr[d] = (((Ds - Dotl)/2) + (((Dctl/2)-ts)*(Pi-Dt)/Pi)
)*Sk[d] # flow area at or near the shell centerline for one crossflow
section in a shell-and-tube exchanger [m²]

                rs = (Asb/(Asb+Atb)) # [-]
                rlm[d] = ((Asb+Atb)/Acr[d]) # [-]
                pcorr = ((-0.15*(1+rs))+0.8) # [-]

                wp = 0.75*Dt # distance between the splitter and the f
irst tube [m]
                Abp[d] = (((Ds - Dotl)/2) +  (Np*wp/2)) * Sk[d] # flow
bypass area of one baffle [m²]

                Nss = Nss # Number of sealing strip pairs
                # Ncc = (Ds - (2*lc))/(Pj/2) # number of effective tub
e rows crossed during flow through one crossflow section (between baff
le tips) [-]
                Ncc = Ntj # When no tubes in the window

                rb[d] = Abp[d]/Acr[d] # [-]
                Nss⁺ = Nss/Ncc # [-]
                Dcorr = 3.7 # 4.5 for Re<100

                Fc = 1 - (2*Fw)
                Ccorr = 1.25 # 1.35 for Re<100

                Li⁺ = 1 # (equation changes when baffle spacing varies
)
                Lo⁺ = 1 # (equation changes when baffle spacing varies
)
                ncorr = 0.6 # 0.33 for laminar flow

                # Jc = 0.55 + (0.72*Fc) # correction factor for baffle
configuration
                Jc = 1 # When no tubes are in the window
                Jl[d] = ((0.44*(1-rs)) + ((1-(0.44*(1-rs)))*exp(-2.2*r
```

```
lm[d])))  # correction factor for baffle leakage effects, including bot
h tube-to-baffle and baffle- to-shell leakages
                Jb[d] = 1 # correction factor for bundle and pass part
ition bypass
                Js = ((NbT + NF - 1) + (Li⁺^(1-ncorr)) + (Lo⁺^(1-ncorr
)))/((NbT + NF - 1) + (Li⁺) + (Lo⁺)) # correction factor for larger ba
ffle spacing at the inlet and outlet sections compared to the central
baffle spacing
                Jr = 1 # different for Re<100

                if Nss⁺<0.5
                    Jb[d] = exp((-Ccorr*rb[d]*(1-((2*Nss⁺)^(0.33)))))
# correction factor for bypass flow
                else
                    Jb[d] = 1
                end

                if Bypass == 1
                    Jb[d] = 1
                end

                Jcorr[d] = Jc*Jl[d]*Jb[d]*Js*Jr # correction factor fo
r shell-side heat transfer

                Diff1 = 100
                Diff2 = 100

                if d==1
                    TInExt[d] = FT₁ᵢ
                    TInInt[d] = T₂₍ᵢₙ₎
                    Tso[d] = (TInExt[d]+TInInt[d])/2
                else
                    TInExt[d] = TOutExt[d-1]
                    TInInt[d] = TOutInt[d-1]
                    Tso[d] = (TInExt[d]+TInInt[d])/2
                end

                if d==1
                    T1avgo[d] = FT₁ᵢ
                    T2avgo[d] = T₂₍ᵢₙ₎
                    T1avgn[d] = FT₁ᵢ
                    T2avgn[d] = T₂₍ᵢₙ₎
                    Tsoavg[d] = (TInExt[d]+TInInt[d])/2
                else
                    T1avgo[d] = TInExt[Int(d-1)]
                    T2avgo[d] = TInInt[Int(d-1)]
                    T1avgn[d] = TInExt[Int(d-1)]
                    T2avgn[d] = TInInt[Int(d-1)]
                    Tsoavg[d] = (TInExt[d]+TInInt[d])/2
                end
```

```
                T1temp = T1avgn[d]+273
                T2temp = T2avgn[d]+273

                iterno = 1

                while Diff1>1 || Diff2>1

                    h1i = PropsSI("H","T",T1temp,"P",P1[d],"CO2") # In
itial Enthalpy of sCO2 in the shell [J/kg]
                    Cp(1i) = PropsSI("C","T",T1temp,"P",P1[d],"CO2") #
Initial Specific heat of sCO2 in the shell [J/kg/K]
                    μ1i = PropsSI("V","T",T1temp,"P",P1[d],"CO2") # In
itial Dynamic viscosity of sCO2 in the shell [Pa-s]
                    ρ1i = PropsSI("D","T",T1temp,"P",P1[d],"CO2") # In
itial Density of sCO2 in the shell [kg/m³]
                    ν1i = μ1i/ρ1i # Initial Kinematic viscosity of sCO
2 in the shell [m²/s]
                    κ1i = PropsSI("conductivity","T",T1temp,"P",P1[d],
"CO2") # Initial Thermal conductivity of sCO2 in the shell [W/m/K]
                    α1i = κ1i/(ρ1i*Cp(1i)) # Initial Thermal diffusivi
ty of sCO2 in the shell [m²/s]

                    h2i = PropsSI("H","T",T2temp,"P",P2[d],"CO2")  # I
nitial Enthalpy of sCO2 in the tubes [J/kg]
                    Cp(2i) = PropsSI("C","T",T2temp,"P",P2[d],"CO2")
# Initial Specific heat of sCO2 in the tubes [J/kg/K]
                    μ2i = PropsSI("V","T",T2temp,"P",P2[d],"CO2")  # I
nitial Dynamic viscosity of sCO2 in the tubes [Pa-s]
                    ρ2i = PropsSI("D","T",T2temp,"P",P2[d],"CO2") # In
itial Density of sCO2 in the tubes [kg/m³]
                    ν2i = μ2i/ρ2i # Initial Kinematic viscosity of sCO
2 in the tubes [m²/s]
                    κ2i = PropsSI("conductivity","T",T2temp,"P",P2[d],
"CO2") # Initial Thermal conductivity of sCO2 in the tubes [W/m/K]
                    α2i = κ2i/(ρ2i*Cp(2i)) # Initial Thermal diffusivi
ty of sCO2 in the tubes [m²/s]

                    if Tsoavg[d]>850
                        @goto eff
                    end

                    Cp(s) = Cpsitp(Tsoavg[d]) # Specific heat of Hayne
s282
                    ρs = ρsitp(Tsoavg[d]) # Density of Haynes282
                    κs = κsitp(Tsoavg[d]) # Thermal conductivity of Ha
ynes282
                    αs = αsitp(Tsoavg[d]) # Thermal diffusivity of Hay
nes282
```

```
                    u1(av) = 0.0
                    u2(av) = 0.0


                    for k in 1:Int(Nk)
                        u1[1,k] = ((ṁh)/(Li*Sk[d]*XM1[1,k]*ρ1i))
                        u1(av) = u1(av) + (u1[1,k]*Hk[k])
                        Re1[1,k] = abs((u1[1,k]*DH1[1,k]/ν1i))
                    end
                    u1(av) = u1(av)/Sk[d]

                    umax[d] = u1[1,1]*DH1[1,1]/DhBi[d] # Maximum veloc
ity of external flow [m/s]
                    ReBi[d] = (umax[d]*DhBi[d])/ν1i # Reynolds number
as defined by Biery [-]
                    ufr[d] = ((ṁh)/(Li*Sk[d]*ρ1i))

                    for j in 1:Int(Nj)
                        u2[j,1] = ((ṁl)/(Li*Lj*XM2[j,1]*ρ2i))
                        u2(av) = u2(av) + (u2[j,1]*Hj[j])
                        Re2[j,1] = abs((u2[j,1]*DH2[j,1]/ν2i))
                    end
                    u2(av) = u2(av)/Lj # Through each grid point

                    for k in 1:Int(Nk)
                        for j in 1:Int(Nj)
                            u1[j,k] = u1[1,k] # [m/s] Uniform flow fie
ld

                            u2[j,k] = u2[j,1] # [m/s] Uniform flow fie
ld

                            Re1[j,k] = Re1[1,k] # [m/s] Uniform flow f
ield

                            Re2[j,k] = Re2[j,1] # [m/s] Uniform flow f
ield


                            if FinType == 0
                                Cd1[j,k] = (0.3622 * ((DhBi[d]/De[d])^
(0.7642)) * ((Pi/Dt)^(0.2711)) * ((Pj/(2*Dt))^(-0.4896)) * ((Re1[1,1])^
(-0.1801)) * 4 * DH1[j,k] * DH1[j,k] * DH1[j,k]) / (DhBi[d] * DhBi[d]
* DhBi[d]) # Friction factor for bare tubes [-]
                            elseif FinType == 1
                                Cd1[j,k] = (0.5529 * ((DhBi[d]/De[d])^
(0.894)) * ((Pi/Dt)^(-0.0878)) * ((Pj/(2*Dt))^(-0.5328)) * ((Df/Dt)^(0.1
075)) * (((Pf-δfb)/Pf)^(-2.2775)) * ((Re1[1,1])^(-0.2071)) * 4 * DH1[j
,k] * DH1[j,k] * DH1[j,k]) / (DhBi[d] * DhBi[d] * DhBi[d]) # Friction
factor for disc fins [-]
                            elseif FinType == 2
                                Cd1[j,k] = (0.2252 * ((DhBi[d]/De[d])^
(0.3195)) * ((Pi/Dt)^(1.1363)) * ((Pj/(2*Dt))^(0.0696)) * ((Df/Dt)^(-0.8
203)) * (((Pf-δfb)/Pf)^(0.2288)) * ((Re1[1,1])^(-0.1976)) * 4 * DH1[j,
```

```
k] * DH1[j,k] * DH1[j,k]) / (DhBi[d] * DhBi[d] * DhBi[d]) # Friction f
actor for pin-fins [-]
                            end

                            if (Re2[j,k]) < 2300
                                Cd2[j,k] = 64/(Re2[j,k]) # Internal Dr
ag
                            end
                            if (Re2[j,k]) > 10000
                                FF = (((0.790*log(Re2[j,k]))-1.64)^2)
                                Cd2[j,k] = 1/(FF) # Internal Drag
                            end
                            if (Re2[j,k]) > 2300 && (Re2[j,k]) < 10000
                                AA = 64.0/2300.0
                                BB = 1.0/((((0.790*log(Re2[j,k]))-1.64
))^2)
                                Cd2[j,k] = AA + ((BB-AA)*(Re2[j,k]-230
0)/(10000-2300)) # Internal Drag
                            end

                            Conv1[j,k] = (ρ1i*Cp(1i)*u1[j,k]*XM1[j,k]/
(Hj[j])) # Refer closed VAT equations
                            Conv2[j,k] = (ρ2i*Cp(2i)*u2[j,k]*XM2[j,k]/
(Hk[k])) # Refer closed VAT equations
                        end
                    end

                    Qj1 = 0.0
                    Qk1 = 0.0
                    T1(av) = 0.0
                    T2(av) = 0.0
                    Qj2 = 0.0
                    Qk2 = 0.0
                    ϵ = 0.0
                    ϵ1 = 0.0
                    ϵ2 = 0.0
                    ϵs = 0.0
                    Nu1 = 0.0
                    Nu2 = 0.0
                    HBk2 = 0
                    HBk2m = 0
                    HBj2 = 0
                    HBj2m = 0

                    #Temperature field setup and thermal calculations
                    Pr1i = ν1i/α1i # Prandtl number of external fluid
[-]
                    Pr2i = ν2i/α2i # Prandtl number of internal fluid
[-]
```

```
                    for k in 1:Int(Nₖ)
                        for j in 1:Int(Nⱼ)
                            T₁[j,k] = TInExt[d] # Temperature of fluid
in shell [°C]
                            T₂[j,k] = TInInt[d] # Temperature of fluid
in tubes [°C]
                            Tₛ[j,k] = (TInInt[d]+TInExt[d])/2.0 # Temp
erature of solid [°C]
                            Tₛₒ[j,k] = Tₛ[j,k] # Outer surface temperat
ure [°C]
                            Tₛᵢ[j,k] = Tₛ[j,k] # Inner surface temperat
ure [°C]

                            Y₁[j,k] = TInExt[d]
                            Y₂[j,k] = TInExt[d]
                            Y₃[j,k] = TInExt[d]
                            Y₂ₒ[j,k] = TInExt[d]
                            Y₂ᵢ[j,k] = TInExt[d]


                            if (Re₂[j,k]) < 2100
                                Nu₂ = 4.36 # Nusselt number of fluid i
n tubes [-]
                            else
                                Nu₂ = (Pr₂ᵢ*(Re₂[j,k]-1000)*(Cd₂[j,k]/
8))/(1+(12.7*((Cd₂[j,k]/8)^(0.5))*((Pr₂ᵢ^(2/3))-1)))
                            end

                            if FinType == 0
                                HH₁[j,k] = (0.3283 * ((DhBi[d]/Dₑ[d])^
(0.4585)) * ((PᵢoDₜ)^(0.0739)) * ((PⱼoDₜ/2)^(-0.2187)) * ((ReBi[d])^(0.
6111)) * K₁ᵢ * (Pr₁ᵢ^(0.333))) / DhBi[d] # Heat transfer coefficient f
or bare tubes [W/m²/K]
                                HH₁[j,k] = HH₁[j,k]*Jcorr[d]
                                HH₂[j,k] = (Nu₂*K₂ᵢ)/DH₂[1,1] # Heat t
ransfer coefficient (internal flow) [W/m²/K]
                            elseif FinType == 1
                                HH₁[j,k] = (0.3574 * ((DhBi[d]/Dₑ[d])^
(0.5029)) * ((PᵢoDₜ)^(-0.1789)) * ((PⱼoDₜ/2)^(-0.16)) * ((Df/Dₜ)^(-0.330
4)) * (((Pf-δfb)/Pf)^(-2.3461)) * ((ReBi[d])^(0.6176)) * K₁ᵢ * (Pr₁ᵢ^(
0.333))) / DhBi[d] # Heat transfer coefficient for Disc fins [W/m²/K]
                                HH₁[j,k] = HH₁[j,k]*Jcorr[d]
                                HH₂[j,k] = (Nu₂*K₂ᵢ)/DH₂[1,1] # Heat t
ransfer coefficient (internal flow) [W/m²/K]
                            elseif FinType == 2
                                HH₁[j,k] = (0.3264 * ((DhBi[d]/Dₑ[d])^
(0.3163)) * ((PᵢoDₜ)^(0.3123)) * ((PⱼoDₜ/2)^(-0.008)) * ((Df/Dₜ)^(0.0329
)) * (((Pf-δfb)/Pf)^(0.1077)) * ((ReBi[d])^(0.5895)) * K₁ᵢ * (Pr₁ᵢ^(0.
333))) / DhBi[d] # Heat transfer coefficient for pin-fins [W/m²/K]
                                HH₁[j,k] = HH₁[j,k]*Jcorr[d]
```

```
                                HH₂[j,k] = (Nu₂*K₂ᵢ)/DH₂[1,1] # Heat t
ransfer coefficient (internal flow) [W/m²/K]
                            end


                            if FinType == 0 || FinType == 1

                                if δfb>0
                                    mf = ((2*HH₁[j,k])/(Kₛ*δfb))^(0.5)
                                    C2f = ((2*rₒₜ/mf) / ((rfc*rfc)-(rₒₜ
*rₒₜ)))
                                    Numf1 = besselk(1,(mf*rₒₜ))*bessel
i(1,(mf*rfc))
                                    Numf2 = besseli(1,(mf*rₒₜ))*bessel
k(1,(mf*rfc))
                                    Denf1 = besseli(0,(mf*rₒₜ))*bessel
k(1,(mf*rfc))
                                    Denf2 = besselk(0,(mf*rₒₜ))*bessel
i(1,(mf*rfc))
                                    ηf[j,k] = C2f * ((Numf1-Numf2)/(De
nf1+Denf2)) # Efficiency of a single disc fin [-]
                                else
                                    ηf[j,k]=0
                                end

                                if Ct>0.0000001
                                    mfint = ((HH₂[j,k]*2*(Ct+Sₖ[d]))/(
Kₛ*Ct*Sₖ[d]))
                                    ηfint[j,k] = tanh(mfint*Ch)/(mfint
*Ch)
                                else
                                    ηfint[j,k] = 0
                                    Ct = 0
                                end

                                SW₁mod[j,k] = (((Nₜₜ*Nf[d]*2*π*Dₜ*(Pf-δf
b)) + (Nₜₜ*Nf[d]*2*π*Df*δfb*ηf[j,k]) + (Nₜₜ*Nf[d]*π*((Df*Df)-(Dₜ*Dₜ))*ηf[
j,k])) / (2*Vₜₒₜ[d])) # Modified specific wetted area for energy equati
on [1/m]
                                SW₂mod[j,k] = ((Nₜₜ*π*Dᵢₚ*Sₖ[d]) - (Nₜₜ*N
cruc*Sₖ[d]*Ct) + (Nₜₜ*2*Ncruc*Ch*Sₖ[d]*ηfint[j,k])) / (Vₜₒₜ[d])

                            elseif FinType == 2

                                if δfb>0
                                    mf = ((4*HH₁[j,k])/(Kₛ*δfb))^(0.5)
                                    Lccpf = ((Df-Dₜ)/2) + (δfb/4)
                                    ηf[j,k] = tanh(mf*Lccpf)/(mf*Lccpf
) # Efficiency of a single pin fin [-]
                                else
```

```
                                    ηf[j,k]=0
                                end

                                if Ct>0.0000001
                                    mfint = ((HH₂[j,k]*2*(Ct+Sₖ[d]))/(
Kₛ*Ct*Sₖ[d]))
                                    ηfint[j,k] = tanh(mfint*Ch)/(mfint
*Ch)
                                else
                                    ηfint[j,k] = 0
                                    Ct = 0
                                end

                                SW₁mod[j,k] = (((Nₜₜ*Nf[d]*2*π*Dₜ*Pf) +
(Nₜₜ*Nf[d]*NAF*π*(Df-Dₜ)*δfb*ηf[j,k])) / (2*Vₜₒₜ[d])) # Modified specific
wetted area for energy equation [1/m]
                                SW₂mod[j,k] = ((Nₜₜ*π*Dᵢₚ*Sₖ[d]) - (Nₜₜ*N
cruc*Sₖ[d]*Ct) + (Nₜₜ*2*Ncruc*Ch*Sₖ[d]*ηfint[j,k])) / (Vₜₒₜ[d])

                            end

                            CT₁ₛ[j,k] = HH₁[j,k]*SW₁mod[j,k]
                            CT₂ₛ[j,k] = HH₂[j,k]*SW₂mod[j,k]

                            Gtemp1 = ((HH₁[j,k]*0.5*Dₜ*log(Dₜ/Dint))/((
HH₁[j,k]*0.5*Dₜ*log(Dₜ/Dint))+Kₛ))-1
                            GTso1[j,k] = Gtemp1+1
                            Itemp1 = ((HH₂[j,k]*0.5*Dᵢₚ*log(Dint/Dᵢₚ))
/((HH₂[j,k]*0.5*Dᵢₚ*log(Dint/Dᵢₚ))+Kₛ))-1
                            ITso1[j,k] = Itemp1+1
                            GTs[j,k] = CT₁ₛ[j,k]*Gtemp1
                            ITs[j,k] = CT₂ₛ[j,k]*Itemp1

                            Htemp1[j,k] = Kₛ/((HH₁[j,k]*0.5*Dₜ*log(Dₜ/D
int))+Kₛ)
                            Jtemp1[j,k] = Kₛ/((HH₂[j,k]*0.5*Dᵢₚ*log(Di
nt/Dᵢₚ))+Kₛ)
                            HTs[j,k] = CT₁ₛ[j,k]*Htemp1[j,k]
                            JTs[j,k] = CT₂ₛ[j,k]*Jtemp1[j,k]
                        end
                    end

                    for k in 1:Int(Nₖ)
                        for j in 1:Int(Nⱼ)

                            Kₛₖ = Kₛ

                            if k == 1
                                HBₖ₂ = Hₖ[1]^2
                                HBₖ₂ₘ = HBₖ₂
```

```
                    else
                        HBk2m = (Hk[k-1]*((Hk[k-1]+Hk[k])/2.0))
                        HBk2 = (Hk[k]*((Hk[k-1]+Hk[k])/2.0))
                    end

                    Ksj = Ks

                    if j == 1
                        HBj2 = Hj[1]^2
                        HBj2m = HBj2
                    else
                        HBj2m = (Hj[j-1]*((Hj[j-1]+Hj[j])/2.0)
)
                        HBj2 = (Hj[j]*((Hj[j-1]+Hj[j])/2.0))
                    end

                    AJTs[j,k] = (XMs[j,k]*Ksk)/HBk2m
                    BJTs[j,k] = (XMs[j,k]*Ksk)/HBk2
                    CJTs[j,k] = AJTs[j,k] + BJTs[j,k]
                    AITs[j,k] = (XMs[j,k]*Ksj)/HBj2m
                    BITs[j,k] = (XMs[j,k]*Ksj)/HBj2
                    CITs[j,k] = AITs[j,k] + BITs[j,k]

                    CT1[j,k] = Conv1[j,k] + CT1s[j,k]
                    CT2[j,k] = Conv2[j,k] + CT2s[j,k]

                    CJTss[j,k] = (CJTs[j,k]+HTs[j,k]+JTs[j,k])
                end
            end


        # Iterative procedure to obtain convergence
            for m in 1:10000

                #Solid side temperature
                for k in 1:Int(Nk)
                    for j in 1:Int(Nj)

                        if j == Int(Nj)
                            Tsp = Ts[j,k]
                        else
                            Tsp = Ts[(j+1),k]
                        end

                        if j == 1
                            Tsm = Ts[j,k]
                        else
                            Tsm = Ts[(j-1),k]
                        end
```

```
                                if k == Int(Nk)
                                    Tsjp = Ts[j,k]
                                else
                                    Tsjp = Ts[j,(k+1)]
                                end

                                if k == 1
                                    Tsjm = Ts[j,k]
                                else
                                    Tsjm = Ts[j,(k-1)]
                                end

                                Y2[j,k] = (((AJTs[j,k]*Tsjm)+(BJTs[j,k]
*Tsjp))/CJTss[j,k]) - (GTs[j,k]*T1[j,k]/CJTss[j,k]) - (ITs[j,k]*T2[j,k]/
CJTss[j,k])

                            end
                        end


                        #External flow temperature
                        for k in 1:Int(Nk)
                            for j in 1:Int(Nj)
                                Y2o[j,k] = (GTso1[j,k]*T1[j,k])+(Htemp
1[j,k]*Y2[j,k])
                                if j == 1
                                    Y1[j,k] = TInExt[d]
                                else
                                    Y1[j,k] = (Y1[(j-1),k]-(CT1s[j,k]*
Y2o[j,k]/Conv1[j,k]))/(1.0-(CT1s[j,k]/Conv1[j,k]))
                                end
                            end
                        end


                        #Internal flow temperature
                        for j in 1:Int(Nj)
                            for k in 1:Int(Nk)
                                Y2i[j,k] = (ITso1[j,k]*T2[j,k])+(Jtemp
1[j,k]*Y2[j,k])
                                if k == 1
                                    Y3[j,k] = TInInt[d]
                                else
                                    Y3[j,k] = ((CT2s[j,k]*Y2i[j,k]/Con
v2[j,k])+Y3[j,(k-1)])/(1.0+(CT2s[j,k]/Conv2[j,k]))
                                end
                            end
                        end

                        #Error calculation
```

```
        ϵ = 0
        for k in 2:Int(Nₖ-1)
            for j in 2:Int(Nⱼ-1)
                ϵ₁ = abs((T₁[j,k]-Y₁[j,k])/T₁[j,k])
                ϵₛ = abs((Tₛ[j,k]-Y₂[j,k])/Tₛ[j,k])
                ϵₛₒ = abs((Tₛₒ[j,k]-Y₂ₒ[j,k])/Tₛₒ[j,k])
                ϵₛᵢ = abs((Tₛᵢ[j,k]-Y₂ᵢ[j,k])/Tₛᵢ[j,k])
                ϵ₂ = abs((T₂[j,k]-Y₃[j,k])/T₂[j,k])

                if ϵ < ϵ₁
                    ϵ = ϵ₁
                end
                if ϵ < ϵₛ
                    ϵ = ϵₛ
                end
                if ϵ < ϵₛₒ
                    ϵ = ϵₛₒ
                end
                if ϵ < ϵₛᵢ
                    ϵ = ϵₛᵢ
                end
                if ϵ < ϵ₂
                    ϵ = ϵ₂
                end
            end
        end


        #Temperature field updation
        for k in 1:Int(Nₖ)
            for j in 1:Int(Nⱼ)
                T₁[j,k] = Y₁[j,k]
                Tₛ[j,k] = Y₂[j,k]
                Tₛₒ[j,k] = Y₂ₒ[j,k]
                Tₛᵢ[j,k] = Y₂ᵢ[j,k]
                T₂[j,k] = Y₃[j,k]
            end
        end

        if((m+1) > 10) && (ϵ < 0.1*(10^-5))
            break #Exit clause
        end

    end

    tempT1 = TInExt[1]

    tempT2 = TInExt[1]

    for j in 1:Nⱼ
```

```
                    for k in 1:Nₖ
                        if T₁[j,k]<0 || T₂[j,k]<0
                            @goto eff
                        end
                    end
                end

                for j in 1:Nⱼ
                    for k in 1:Nₖ
                        if isnan(T₁[j,k]) || isnan(T₂[j,k]) || isn
an(-T₁[j,k]) || isnan(-T₂[j,k])
                            @goto eff
                        end
                    end
                end

                iterno = iterno+1

                hiav[d] = 0.0
                hi[1] = PropsSI("H","T",(T₂[1,Nₖ]+273),"P",P₂[d],"
CO2")
                for a in 2:Nⱼ
                    hi[a] = PropsSI("H","T",(T₂[a,Nₖ]+273),"P",P₂[
d],"CO2")
                    hiav[d] = (((hi[a]+hi[a-1])/2)*(Lⱼ/Nⱼ)) + hiav
[d]
                end
                hiav[d] = hiav[d]/(Lⱼ-(Lⱼ/Nⱼ))

                hoav[d] = 0.0
                ho[1] = PropsSI("H","T",(T₁[Nⱼ,1]+273),"P",P₁[d],"
CO2")
                for a in 2:Nₖ
                    ho[a] = PropsSI("H","T",(T₁[Nⱼ,a]+273),"P",P₁[
d],"CO2")
                    hoav[d] = (((ho[a]+ho[a-1])/2)*(Sₖ[d]/Nₖ)) + ho
av[d]
                end
                hoav[d] = hoav[d]/(Sₖ[d]-(Sₖ[d]/Nₖ))

                if hiav[d]>3982400 || hoav[d]>3982400
                    @goto eff
                end

                TOutExt[d] = PropsSI("T","H",hoav[d],"P",P₁[d],"CO
2")-273
                TOutInt[d] = PropsSI("T","H",hiav[d],"P",P₂[d],"CO
2")-273

                T1avgo[d] = T1avgn[d]
```

```
                    T1avgn[d] = (TInExt[d]+TOutExt[d])/2
                    T2avgo[d] = T2avgn[d]
                    T2avgn[d] = (TInInt[d]+TOutInt[d])/2
                    Tsoavg[d] = (T1avgn[d]+T2avgn[d])/2
                    Tsext[d] = Tso[1,1]
                    Tsavg[d] = Ts[1,1]
                    Tsint[d] = Tsi[1,1]

                    if Tsoavg[d]>850
                        @goto eff
                    end

                    Diff1 = abs(T1avgn[d]-T1avgo[d])
                    Diff2 = abs(T2avgn[d]-T2avgo[d])

                    T1temp = T1avgn[d]+273
                    T2temp = T2avgn[d]+273
                end

                for k in 1:Nk
                    T1ca[d,k] = T1[Nj,k]
                end
                for j in 1:Nj
                    T2ca[d,j] = T2[j,Nk]
                end

                for k in 1:Nk
                    for j in 1:Nj
                        T1total[j,Int(((d-1)*Nk)+k),1] = T1[j,k] # Tem
perature of fluid in shell [°C]
                        T2total[j,Int(((d-1)*Nk)+k),1] = T2[j,k] # Tem
perature of fluid in tubes [°C]
                        Tstotal[j,Int(((d-1)*Nk)+k),1] = Ts[j,k] # Temp
erature of solid [°C]
                        Sotal[j,Int(((d-1)*Nk)+k),1] = Tso[j,k]
                        Sitotal[j,Int(((d-1)*Nk)+k),1] = Tsi[j,k]
                    end
                end

                ρi[d] = ρ2i
                ρo[d] = ρ1i
                ui[d] = u2(av)
                uo[d] = u1(av)
                fi[d] = Cd2[1,1]
                fo[d] = Cd1[1,1]
                Dhi[d] = DH2[1,1]
                Dho[d] = DH1[1,1]
                Rei[d] = Re2[1,1]
                Reo[d] = Re1[1,1]
                hc1[d] = HH1[1,1]
```

```
t(((d-1)*Nk)+k),1]
                    end
                end
            end
        end

        #Pressure drop and Pumping Power calculation

        a=1
        b=1

        ζs = 2
        Aw = 0.0
        ΔP1t = 0.0
        ΔP2t = 0.0

        for dtemp in 1:NbT+2
            ζl[dtemp] = exp((-1.33*(1+rs)*((rlm[dtemp])^(pcorr)))) # C
orrection factor for tube-to-baffle and shell-to-baffle leakage
            ζb[dtemp] = 1 # correction factor for bypass flow
            ζs = 2 # correction factor for inlet and outlet losses (eq
uation changes when baffle spacing varies)

            if Nss+<0.5
                ζb[dtemp] = exp((-Dcorr*rb[dtemp]*(1-((2*Nss+)^(0.33))
))) # correction factor for bypass flow
            else
                ζb[dtemp] = 1
            end

            As[dtemp] = (((Ds/2)-ts)*Sk[dtemp]*(1-(Dt/Pi))) # Area at th
e centerline of the shell [m²]
            Aw = ((π*NDs*NDs/8) - (AtotN) - (ts*NDs))/2 # Area of the w
indow for external flow turning [m²]

            if Bypass == 1
                ζb[dtemp] = 1 # correction factor for bypass flow
            end
        end

        DF = 0.0
        tubeP = ones(Int(NbT+2))
        windowP = ones(Int(NbT+1))

        for a in 1:Int(NbT+2)
            if (a == 1) || (a == (NbT+2))
                ΔP1 = 1.0 * (((fo[a]*ρo[a]*(uo[a]^2)*Lj) / (Dho[a]*2.0
))) *(1+(Ncw/Ncc))*ζb[a]*ζs*ζl[a] # Entrance and exit pressure drop in
external flow [N/m²]
            else
```

```
                ΔP₁ = ((fo[a]*ρo[a]*(uo[a]^2)*Lⱼ) / (Dho[a]*2.0))*ζb[a
]*ζl[a] # pressure drop in center [N/m²]
            end
            η₁ = 1.0 # Pump efficiency [-]
            F₁ = (ΔP₁*Lᵢ*Sₖ[a]*XM₁[1,1]) # [N]
            PP₁ = ((F₁*uo[a])/η₁) # [W]
            ΔP₁ₜ = ΔP₁ₜ+ΔP₁
            F₁ₜ = F₁ₜ + F₁
            PP₁ₜ = PP₁ₜ + PP₁
            DF = (((fo[b]*ρo[b]*(uo[b]^2)*π*Dₜ*Sₖ[b]))/2.0)+DF
            tubeP[a] = ΔP₁
        end

        ΔP₁tube = 0.0
        ΔP₁tube = ΔP₁ₜ

        for a in 1:(NbT+1)
            ΔPw = ((ṁₕ*ṁₕ*(2 + (0.6*Ncw)))/(2*ρo[a]*As[a]*Aw))*ζl[a] #
Pressure drop in the window for external flow [N/m²]
            η₁ = 1.0 # Pump efficiency [-]
            F₁ = (ΔPw*Lᵢ*Sₖ[a]*XM₁[1,1]) # [N]
            PP₁ = ((F₁*uo[a])/η₁) # [W]
            ΔP₁w = ΔP₁w+ΔPw
            ΔP₁ₜ = ΔP₁ₜ+ΔPw
            F₁ₜ = F₁ₜ + F₁
            PP₁ₜ = PP₁ₜ + PP₁
            windowP[a] = ΔPw
        end


        for b in 1:Int(NbT+2)
            ΔP₂ = (((fi[b]*ρi[b]*(ui[b]^2)*(Sₖ[b])/(Dhi[b]*2.0))))
            η₂ = 1.0 # Pump efficiency [-]
            F₂ = (ΔP₂*Lᵢ*Lⱼ*XM₂[1,1]) # [N]
            PP₂ = ((F₂*u₂[1,1])/η₂) # [W]
            ΔP₂ₜ = ΔP₂ₜ+ΔP₂
            F₂ₜ = F₂ₜ + F₂
            PP₂ₜ = PP₂ₜ + PP₂
            DPInt[b] = ΔP₂
        end

        DFO = DF/(NbT+2)

        Dexp = 1.8*(min(Pᵢ,Pⱼ,Pₓ)-(Dₜ/4)) # Diameter of expansion (ima
ginary circle)
        σ = (Dhi[1]*Dhi[1])/(Dexp*Dexp) # Ratio of area of cotracted t
o expanded tube
        Ke = ((1-σ)^(2))
        Kc = (0.5*(1-σ))
        Gt = ṁₕ/(Nₜₜ*π*Dhi[1]*Dhi[1]/4)
```

```
        ΔPce = (0.5*(NF+1)*(Kc+Ke)*Gt*Gt)/(2*((ρi[1]+ρi[(NbT+2)])/2))
# (NF+1)/2 instead of NF+1 for U-tubes

        ΔPiutot = 0.0 # Average pressure drop in u-bend region for int
ernal flow [Pa]

        ρibend = (ρi[NbL+1]+ρi[NbL+2])/2
        uibend = (ui[NbL+1]+ui[NbL+2])/2
        fibend = (fi[NbL+1]+fi[NbL+2])/2

        c = 0
        θbend = 180 # bending angle of tube [in degrees]

        for c in 1:Nti
            Rbend[c] = ts + (c*Pi/2)
            RbendoDtint[c] = Rbend[c]/Dip
            kbend[c] = kbenddata(RbendoDtint[c])
            ΔPiu[c] = ρibend*(uibend^2)*0.5*((fibend*π*Rbend[c]*θbend/
(Dip*180))+kbend[c])
            ΔPiutot = ΔPiutot + ΔPiu[c]
        end

        ΔPiutot = ΔPiutot/Nti

        ΔP2t = ΔP2t + ΔPce + ΔPiutot # Total internal pressure drop [N/
m²]

        PPt = PP1t + (PP2t*Ntt)

        P1temp1 = P1(in)
        P2temp1 = P2(in)
        P1tempF = 0.0
        P2tempF = 0.0
        for a in 1:NbT+2
            if a == 1
                P1[a] = P1temp1 - ((tubeP[a]+(windowP[a]/2))/2)
                P1temp1 = P1temp1 - ((tubeP[a]+(windowP[a]/2)))
            elseif a == (NbT+2)
                P1[a] = P1temp1 - ((tubeP[a]+(windowP[a-1]/2))/2)
                P1temp1 = P1temp1 - ((tubeP[a]+(windowP[a-1]/2)))
            else
                P1[a] = P1temp1 - ((tubeP[a]+(windowP[a-1]/2)+(windowP
[a]/2))/2)
                P1temp1 = P1temp1 - ((tubeP[a]+(windowP[a-1]/2)+(windo
wP[a]/2)))
            end

            if a == 1
                P2[a] = P2temp1 - (((DPInt[a]/2)+(ΔPce/2)))
```

```
                P2temp1 = P2temp1 - (DPInt[a]+(ΔPce/2))
            elseif a == (NbL+2)
                P₂[a] = P2temp1 - ((DPInt[a]/2)+(ΔPiutot))
                P2temp1 = P2temp1 - (DPInt[a]+(ΔPiutot))
            else
                P₂[a] = P2temp1 - ((DPInt[a]/2))
                P2temp1 = P2temp1 - (DPInt[a])
            end
        end
        P1tempF = P1temp1
        P2tempF = P2temp1 - (ΔPce/2)

        DiffPtempInt = abs((P2tempF-P2tempO)/P2tempO)
        DiffPtempExt = abs((P1tempF-P1tempO)/P1tempO)

        P1tempO = P1tempF
        P2tempO = P2tempF

        Diff3 = 100.0

        Effo = 0.00
        Effn = Effn
        Efft = 1.00

        if (ΔP₁ₜ>=P₁₍ᵢₙ₎) || (ΔP₂ₜ>=P₂₍ᵢₙ₎)
            @goto pressexcess
        end

    end


    PRAv = 0.0
    IntTubeP = 0.0

    for dtemp in 1:NbT+1
        Aturn = ((π*NDₛ*NDₛ/8) - (AtotN) - (tₛ*NDₛ))/2
        uturn[dtemp] = ṁₕ/(ρo[dtemp]*Aturn)
        uhead[dtemp] = (uturn[dtemp]*uturn[dtemp])/(2*9.81)
        uheadPr[dtemp] = (ρo[dtemp]*uturn[dtemp]*uturn[dtemp])/2
        if dtemp != 1
            IntTubeP = ((fo[dtemp]*ρo[dtemp]*(uo[dtemp]^2)*Lⱼ) / (Dho[
dtemp]*2.0))*ζb[dtemp]*ζl[dtemp]
        else
            IntTubeP = ((fo[dtemp]*ρo[dtemp]*(uo[dtemp]^2)*Lⱼ) / (Dho[
dtemp]*2.0))
        end
        Pratio[dtemp] = IntTubeP/uheadPr[dtemp]
        PRAv = PRAv + Pratio[dtemp]
    end
```

```
    PRAv = PRAv/(NbT+1)

    #Calculate heat exchanger effectiveness

    heia = PropsSI("H","T",(TOutExt[NbT+2]+273),"P",P1(in),"CO2")
    heoa = PropsSI("H","T",(TInExt[1]+273),"P",P1(in)-ΔP1t,"CO2")
    heii = PropsSI("H","T",(T1(in)+273),"P",P1(in),"CO2")
    heoi = PropsSI("H","T",(T2(in)+273),"P",P1(in),"CO2")
    Qae = ṁh*(heia-heoa)
    Qme = ṁh*(heii-heoi)

    hiia = PropsSI("H","T",(TInInt[1]+273),"P",P2(in),"CO2")
    hioa = PropsSI("H","T",(TOutInt[NbT+2]+273),"P",P2(in)-ΔP2t-(ΔPce/2
),"CO2")
    hiii = PropsSI("H","T",(T1(in)+273),"P",P2(in),"CO2")
    hioi = PropsSI("H","T",(T2(in)+273),"P",P2(in),"CO2")
    Qai = ṁl*(hioa-hiia)
    Qmi = ṁl*(hiii-hioi)

    Qm = min(Qme,Qmi)

    HXEffExt = Qae/Qm
    HXEffInt = Qai/Qm

    #Calculate heat transfer coefficient and Reynolds number
    Reintav = 0.0
    Reextav = 0.0
    hintav = 0.0
    hextav = 0.0
    ufront = 0.0
    uinternal = 0.0
    umaximum = 0.0

    for d in 1:(NbT+2)
        Reintav = Reintav + Rei[d]
        Reextav = Reextav + Reo[d]
        hintav = hintav + hc2[d]
        hextav = hextav + hc1[d]
        ufront = ufront + ufr[d]
        uinternal = uinternal + ui[d]
        umaximum = umaximum + umax[d]
    end

    Reintav = Reintav/(NbT+2)
    Reextav = Reextav/(NbT+2)
    hintav = hintav/(NbT+2)
    hextav = hextav/(NbT+2)
    ufront = ufront/(NbT+2)
    uinternal = uinternal/(NbT+2)
    umaximum = umaximum/(NbT+2)
```

```
    #Calculate Volume and weight
    Volume = 0.0
    NfinsL = 0
    NfinsR = 0
    ρs = ρsitp(550)
    for dtemp in 1:NbL+1
        NfinsL = NfinsL + Nf[dtemp]
    end
    for dtemp in NbL+2:NbT+2
        NfinsR = NfinsR + Nf[dtemp]
    end
    NfinsL = round(Int64,NfinsL)
    NfinsR = round(Int64,NfinsR)
    Volume = Volume + (NbT*((0.5*π*((NDs^2)-(Ntt*(Dt^2)))/4)-(ts*NDs))*tk
) + (π*((Dos^2)-(NDs^2))*Lk/4) + (ts*(NF+1)*NDs*Lk) + (2*Ht*π*((Dos^2)-(Nt
t*(Dip^2)))/4) + ((NF)*NfinsL*Ntt*π*((Df*Df)-(Dt*Dt))*δfb/4)+ ((NF)*Nfins
R*Ntt*π*((Df*Df)-(Dt*Dt))*δfb/4) + ((NF+1)*Ntt*π*((Dt*Dt)-(Dip*Dip))*Lk/4) +
((NF+1)*Ntt*((Ncruc*Ct*Ch*Lk) + (Ct*Ct*Lk))) + (((2*ExD)+(2*Lj))*tsb*Lk)
    Weight = Volume*ρs
    HXVolume = (π*Dos*Dos*(Lk+(2*Ht)))/4

    print("Internal pressure drop                    : ",round((ΔP2t/10
0000),digits=3)," bar \n")
    print("External pressure drop                    : ",round((ΔP1t/10
0000),digits=3)," bar \n\n")
    print("Pumping power (Internal flow)             : ",round((PP2t*Ntt)
,digits=3)," Watts \n")
    print("Pumping power (External flow)             : ",round((PP1t),d
igits=3)," Watts \n")
    print("Total pumping power                       : ",round((PPt),di
gits=3)," Watts \n\n")

    print("Total power (External)                    : ",round((Qae),di
gits=3)," Watts \n")
    print("Total power (Internal)                    : ",round((Qai),di
gits=3)," Watts \n")
    print("Maximum available power                   : ",round((Qm),dig
its=3)," Watts \n\n")

    print("Heat exchanger effectiveness (External)   : ", round(HXEffEx
t, digits=3) ,"\n")
    print("Heat exchanger effectiveness (Internal)   : ", round(HXEffIn
t, digits=3) ,"\n\n")

    print("External flow inlet temperature  [°C]     : ",round(TOutExt[
NbT+2], digits=2),"\n")
    print("External flow outlet temperature [°C]     : ",round(TInExt[1
], digits=2),"\n")
    print("Internal flow inlet temperature  [°C]     : ",round(TInInt[1
```

```
], digits=2),"\n")
    print("Internal flow outlet temperature [°C]    : ",round(TOutInt[
NbT+2], digits=2),"\n\n")

    print("HX Length                        [m]     : ",round(Lk, digi
ts=6),"\n")
    print("Solid volume                     [m³]    : ",round(Volume,
digits=6),"\n")
    print("HX Weight                        [kg]    : ",round(Weight,
digits=4),"\n")
    print("HX Volume                        [m³]    : ",round(HXVolume
, digits=6),"\n\n")

    output = open("HXTestData.csv", "a")
    CSV.File(output; header=false)
    CSV.File(output; dateformat="mm/dd/yyyy")
    Time = Dates.now()
    Time = Dates.format(Time, "e, dd u yyyy HH:MM:SS")
    OutParameters = [Int(counter) Time round(TOutExt[NbT+2],digits=2)
round(TInInt[1],digits=2) round(TInExt[1],digits=2) round(TOutInt[NbT+
2],digits=2) round(HXEffExt,digits=3) round(HXEffInt,digits=3) round(N
Ds,digits=4) round(Dos,digits=4) round(Dip,digits=6) round(Dt,digits=6)
round(ExD,digits=4) round(Ntt*2,digits=2) round(NbT,digits=2) round(tk,
digits=6) round(Ntj,digits=2) round(Nti,digits=2) round(Pj,digits=6) ro
und(Pi,digits=6) round(Lk,digits=3) round(Df,digits=6) round(δfb,digit
s=8) round(δft,digits=8) round(Pf,digits=8) round(Ct,digits=4) round(R
eintav,digits=2) round(Reextav,digits=2) round(ufront,digits=4) round(
uinternal,digits=4) round(hintav,digits=2) round(hextav,digits=2) roun
d((ΔP1w/100000),digits=3) round((ΔP1tube/100000),digits=3) round(PRAv,
digits=3) round((ΔP1t/100000),digits=3) round((ΔP2t/100000),digits=3) r
ound(PPt,digits=2) round(Qae,digits=2) round(Qai,digits=2) round(Qme,d
igits=2) round(Volume,digits=6) round(Weight,digits=3) round(HXVolume,
digits=6)]
    CSV.write(output, DataFrame(OutParameters);append=true)
    close(output)


    @goto finishit

    @label endit
    output = open("HXTestData.csv", "a")
    CSV.File(output; header=false)
    CSV.File(output; dateformat="mm/dd/yyyy")
    Time = Dates.now()
    Time = Dates.format(Time, "e, dd u yyyy HH:MM:SS")
    OutParameters = [Int(counter) Time "Violates constraints" "Violate
s constraints" "Violates constraints" "Violates constraints" "Violates
constraints" "Violates constraints" round(NDs,digits=3) round(Dos,digit
s=3) round(Dip,digits=6) round(Dt,digits=6) round(ExD,digits=4) round(N
tt,digits=2) round(NbT,digits=2) round(tk,digits=6) round(Ntj,digits=2)
```

```
round(Nti,digits=2) round(Pj,digits=6) round(Pi,digits=6) round(Lk,digi
ts=3) round(Df,digits=6) round(δfb,digits=8) round(δft,digits=8) round
(Pf,digits=8) "Violates constraints" "Violates constraints" "Violates
constraints" "Violates constraints" "Violates constraints" "Violates c
onstraints" "Violates constraints" "Violates constraints" "Violates co
nstraints" "Violates constraints"]
    CSV.write(output, DataFrame(OutParameters);append=true)
    close(output)

    @goto finishit

    @label pressexcess
    print("Pressure drop exceeds the input value!")
    @goto finishit

    @label finishit

    return T1total,T2total,Tstotal,Tsototal,Tsitotal,Nk,Nj,Nti,Ntj,NbT,Pj
,Pi,P1(in),P2(in),tubeP,windowP,DPInt,ΔPce

end
```

Out[30]: HX (generic function with 1 method)

Main function calling the HX function

In [31]:
```
function main()

    Dt = 0.002  # Tube outer diameter [m]
    PioDt = 1.50  # Pitch/diameter of tube in the x direction (columns
) [-]
    PjoDt = 2.90  # Pitch/diameter of tube in the y direction (rows) [
-]
    NbL = 5 # Number of baffles in the left side of the HX [-]
    NbR = 5 # Number of baffles in the right side of the HX [-]
    Ntt = 100 # Total number of tubes on one side of the HX [-]
    Lk = 0.5  # Length of heat exchanger [m]

    ts = 0.001 # Thickness of longitudinal baffle on one side [m]
    Bχ = 0.5 # Percentage of shell height occupied by tubes [-]
    tk = 0.0005  # Baffle thickness [m]
    BaL = 1.0 # Baffle spacing factor in the left side of the HX (0-1)
[-]
    BaR = 1.0 # Baffle spacing factor in the right side of the HX (0-1
) [-]
    NF = 1 # Number of folds [-]
    Np = 1 # Number of tube passes [-]
```

```
    ṁₕ = 0.1  # Hot side mass flow (External) [kg/s]
    ṁₗ = 0.1  # Cold side mass flow (Internal)[kg/s]
    Ratio = 1.00  # (ṁₕ*Cₚ₍ₕ₎/(ṁₗ*Cₚ₍ₗ₎)

    T₁₍ᵢₙ₎ = 800.00  # Hot inlet temperature (External) [°C]
    T₂₍ᵢₙ₎ = 300.00  # Cold inlet temperature (Internal) [°C]
    P₁₍ᵢₙ₎ = 8e6  # External flow inlet pressure [Pa]
    P₂₍ᵢₙ₎ = 25e6  # Internal flow inlet pressure [Pa]

    FinType = 0 # 0 for bare tubes, 1 for disc fins, 2 for pin-fins

    NAF = Int(10) # Total number of cylindrical pin-fins in the annula
r direction on one tube; 0 for disc fins and bare tubes

    DfoDₜ = 1.0 # Fin diameter to tube OD ratio [m] (Varies between 1
to min(Pd,Pl,Pt)); 1 for bare tubes
    Df = DfoDₜ * Dₜ # Fin diameter [m]
    δfboDt = 0.0 # Fin base thickness to fin diameter ratio [-] (varie
s between 0 to 0.1); 0 for bare tubes
    δfb = δfboDt * Dₜ # Fin base thickness [m]
    δft = δfb # Fin tip thickness (same as fin base thickness for disc
fins and cylindrical pin-fins) [m]
    PfoδfbPfoδfb = 4.0 # Fin pitch to fin base thickness ratio [-] (varies b
etween 2 to 10)
    Pf = PfoδfbPfoδfb * δfb # Fin pitch [m]

    CtoDt = 0.0 # Cruciform thickness to tube OD ratio [-] (between 0-
0.2); 0 for tubes w/o internal augmentation
    Ct = CtoDt*Dₜ # Cruciform thickness [m]
    Ncruc = 4 # Number of "longitudinal internal fins" (cruciform)

    if FinType == 0
        DfoDₜ = 1.0 # Fin diameter to tube OD ratio [m] (Varies betwee
n 1 to min(Pd,Pl,Pt)); 1 for bare tubes
        Df = DfoDₜ * Dₜ # Fin diameter [m]
        δfboDt = 0.0 # Fin base thickness to fin diameter ratio [-] (v
aries between 0 to 0.1); 0 for bare tubes
        δfb = δfboDt * Dₜ # Fin base thickness [m]
        δft = δfb # Fin tip thickness (same as fin base thickness for
disc fins and cylindrical pin-fins) [m]
        PfoδfbPfoδfb = 4.0 # Fin pitch to fin base thickness ratio [-] (vari
es between 2 to 10)
        Pf = PfoδfbPfoδfb * δfb # Fin pitch [m]
    end

    CtoDt = 0.0 # Cruciform thickness to tube OD ratio [-] (between 0-
0.2); 0 for tubes w/o internal augmentation
    Ct = CtoDt*Dₜ # Cruciform thickness [m]
    Ncruc = 4 # Number of "longitudinal internal fins" (cruciform)
```

```
    ExD = 0.01 # Extra space taken by the side longitudinal baffles [m
]

    ttoDt = 0.2 # Ratio of tube thickness to tube OD [-]
    tsoDs = 0.1 # Ratio of shell thickness to shell ID [-]
    Ht = 0.01 # Header thickness [m]
    δsb = 0.0 # Diametral clearance between shell and baffle [m]
    δtb = 0.0508*0.001 # Diametral clearance between tube and baffle h
ole [m]
    tsb = 0.00254 # Thickness of side longitudinal baffle [m]

    Bypass = 1 # 0 to consider bypass effects; 1 to neglect bypass eff
ects

    Nss = 0 # Number of sealing strips [-]

    if Ct<0.0000001
        Ct = 0
        Ncruc = 0
        Ch = 0
    end

    if δfb<0.0000001 || DfoDt<1.0001
        Pf = 0
        δfb = 0
        Df = Dt
    end

    if (FinType == 0 || FinType == 1 || FinType == 2)
    else
        print("Please re-run with a valid external fin type")
    end

    counter = 1

    CaseRun = 0

    IJulia.clear_output(true)

    Header=["HX No." "Date" "Inlet Te [°C]" "Inlet Ti [°C]" "Outlet Te
[°C]" "Outlet Ti [°C]" "ϵe [-]" "ϵi [-]" "Shell Di [m]" "Shell Do [m]"
"Tube Di [m]" "Tube Do [m]" "ExD [m]" "Number of tubes [-]" "Number of
baffles [-]" "Baffle thickness [m]" "Number of rows [-]" "Number of co
lumns [-]" "Longitudinal pitch [m]" "Transverse pitch [m]" "Length of
HX [m]" "Fin diameter [m]" "Fin base thickness [m]" "Fin tip thickness
[m]" "Fin pitch [m]" "Cruciform thickness [m]" "Re internal [-]" "Re e
xternal [-]" "External frontal velocity [m/s]" "Internal flow velocity
[m/s]" "HTC internal [W/m²K]" "HTC external [W/m²K]" "Window ΔPe [bar]
" "Tube bundle ΔPe" "Core ΔP/V [-]" "ΔPe [bar]" "ΔPi [bar]" "Pumping p
ower [W]" "Total power (ext) [W]" "Total power (int) [W]" "Maximum ava
```

```
ilable power [W]" "Solid Volume [m³]" "HX Weight [kg]" "HX Volume [m³]
"]
    output = open("HXTestData.csv", "a")
    CSV.File(output; header=false)
    CSV.write(output, DataFrame(Header);append=true)
    close(output)

    @time Outputs = HX(Dt, PiODt, PjODt, NbL, NbR, Ntt, Lk, ts, Bχ, tk, Ba
L, BaR, NF, Np, ṁh, T2(in), T1(in), Ratio, CaseRun, counter, Df, δfb, δ
ft, Pf, Ct, Ncruc, ExD,P1(in),P2(in),ṁl, ttoDt, tsoDs, Ht, δsb, δtb, Nss
, tsb, Bypass, FinType, NAF)

end
```

Out[31]: main (generic function with 1 method)

Run the code

In [32]:
```
Outputs = main();
```

```
Internal pressure drop                    : 0.623 bar
External pressure drop                    : 0.143 bar

Pumping power (Internal flow)             : 4260.431 Watts
Pumping power (External flow)             : 32.593 Watts
Total pumping power                       : 4293.025 Watts

Total power (External)                    : 52376.412 Watts
Total power (Internal)                    : 49989.139 Watts
Maximum available power                   : 60121.287 Watts

Heat exchanger effectiveness (External)   : 0.871
Heat exchanger effectiveness (Internal)   : 0.831

External flow inlet temperature  [°C]     : 800.29
External flow outlet temperature [°C]     : 368.14
Internal flow inlet temperature  [°C]     : 300.0
Internal flow outlet temperature [°C]     : 697.36

HX Length                        [m]      : 0.5
Solid volume                     [m³]     : 0.001567
HX Weight                        [kg]     : 12.8665
HX Volume                        [m³]     : 0.003523

  1.342915 seconds (1.22 M allocations: 26.352 MiB, 0.37% gc time)
```

Plot temperature contours

In [ ]:
```
T1 = Outputs[1];
T2 = Outputs[2];
Ts = Outputs[3];
Tso = Outputs[4];
Tsi = Outputs[5];
zgrid = Outputs[6];
ygrid = Outputs[7];
Ncolumns = Outputs[8];
Nrows = Outputs[9];
Nbaffles = Outputs[10];
Pl = Outputs[11];
Pt = Outputs[12];
EPin = Outputs[13];
IPin = Outputs[14];
DpTB = Outputs[15];
DpW = Outputs[16];
DpInt = Outputs[17];
DpCE = Outputs[18];
```

In [ ]:
```
backend(:plotly)
T1updated = ones(ygrid,(zgrid*(Nbaffles+2)),Ncolumns)

for i in 1:ygrid
    for j in 1:(zgrid*(Nbaffles+2)) #(Nk*Nbaffles)
        for k in 1:Ncolumns

            Diff = j
            while Diff>(2*ygrid)
                Diff = Diff-(2*ygrid)
            end

            if Diff<(zgrid+1)
                UCno = Int((j-Diff)/ygrid)+1
            else
                UCno = Int((j-Diff+ygrid)/ygrid)+1
            end

            if iseven(UCno)
                T1updated[i,j,k] = T1[(ygrid-i+1),((UCno*ygrid)-Diff+y
grid+1),k]
            else
                T1updated[i,j,k] = T1[i,j,k]
            end
        end
    end
```

```
end

T2yavg = ones(1,(zgrid*(Nbaffles+2)),Ncolumns)

for i in 1:Ncolumns
    for k in 1:(zgrid*(Nbaffles+2))
        temp = 0.0
        for j in 1:ygrid
            temp = temp + T2[j,k,i]
        end
        T2yavg[1,k,i] = temp/ygrid
    end
end

Tsyavg = ones(1,(zgrid*(Nbaffles+2)),Ncolumns)

for i in 1:Ncolumns
    for k in 1:(zgrid*(Nbaffles+2))
        temp = 0.0
        for j in 1:ygrid
            temp = temp + Ts[j,k,i]
        end
        Tsyavg[1,k,i] = temp/ygrid
    end
end

Tsoyavg = ones(1,(zgrid*(Nbaffles+2)),Ncolumns)

for i in 1:Ncolumns
    for k in 1:(zgrid*(Nbaffles+2))
        temp = 0.0
        for j in 1:ygrid
            temp = temp + Tso[j,k,i]
        end
        Tsoyavg[1,k,i] = temp/ygrid
    end
end

Tsiyavg = ones(1,(zgrid*(Nbaffles+2)),Ncolumns)

for i in 1:Ncolumns
    for k in 1:(zgrid*(Nbaffles+2))
        temp = 0.0
        for j in 1:ygrid
            temp = temp + Tsi[j,k,i]
        end
        Tsiyavg[1,k,i] = temp/ygrid
    end
end
```

```
ygridnew = Int(ygrid*20)

totTyz = ones(ygridnew,(zgrid*(Nbaffles+2)),Ncolumns)

for i in 1:Ncolumns
    for k in 1:(zgrid*(Nbaffles+2))
        for jt in 1:ygridnew

            if jt>(Int((ygridnew/4)+6))
                j = Int(round((jt/10)-(ygrid/2),digits=0))
            else
                j = 1
            end

            if jt>(Int(ygridnew/4)) && jt<(Int((3*ygridnew/4)+1))
                if j<(Int((ygrid/2)-14)) || j>(Int((ygrid/2)+15))
                    totTyz[jt,k,i] = T1updated[j,k,i]
                elseif j == (Int((ygrid/2)-10)) || j == (Int((ygrid/2)
+11))
                    totTyz[jt,k,i] = Tsiyavg[1,k,i]
                elseif j > (Int((ygrid/2)-10)) && j < (Int((ygrid/2)+1
1))
                    totTyz[jt,k,i] = T2yavg[1,k,i]
                else
                    totTyz[jt,k,i] = Tsoyavg[1,k,i]
                end
            end

            Diff = k
            while Diff>(2*ygrid)
                Diff = Diff-(2*ygrid)
            end

            if Diff<(zgrid+1)
                UCno = Int((k-Diff)/ygrid)+1
            else
                UCno = Int((k-Diff+ygrid)/ygrid)+1
            end

            if isodd(UCno)
                if jt<(Int((ygridnew/4)+1))
                    totTyz[jt,k,i] = (T1[1,Int(((UCno*ygrid)-(ygrid/2)
)),i])
                elseif jt>(Int((3*ygridnew/4)))
                    totTyz[jt,k,i] = (T1[ygrid,Int(((UCno*ygrid)-(ygri
d/2))),i])
                end
            else
                if jt<(Int((ygridnew/4)+1))
                    totTyz[jt,k,i] = (T1[ygrid,Int(((UCno*ygrid)-(ygri
```

```
d/2))),i])
                elseif jt>(Int((3*ygridnew/4)))
                    totTyz[jt,k,i] = (T1[1,Int(((UCno*ygrid)-(ygrid/2)
)),i])
                end
            end

        end
    end
end
```

In [ ]:

```
backend(:plotly)
ys = [string("Ny ",i) for i in 1:ygridnew]
zs = [string("Nz ",i) for i in 1:(zgrid*(Nbaffles+2))]
plot3 = heatmap(totTyz[:,:,1], yflip=false, c=cgrad([:blue4,:blue1,:co
rnflowerblue,:aqua,:aquamarine3,:lime,:yellow,:orange,:red,:maroon]))

pointsz= ones(2,(Nbaffles+1))
pointsy = ones(2,(Nbaffles+1))

for i in 1:(Nbaffles+1)
    pointsz[1,i] = i*ygrid
    pointsz[2,i] = i*ygrid

    if iseven(i)
        pointsy[1,i] = ygridnew
        pointsy[2,i] = Int(ygridnew/4)
    else
        pointsy[1,i] = 0
        pointsy[2,i] = Int(3*ygridnew/4)
    end
end

for i in 1:(Nbaffles+1)
    plot3 = plot!(pointsz[:,i], pointsy[:,i], c=([:black]), line=4)
end

points1z = [zgrid 0 0 0 (zgrid*(Nbaffles+2)) (zgrid*(Nbaffles+2));(zgr
id*(Nbaffles+1)) (zgrid*(Nbaffles+2)) 0 0 (zgrid*(Nbaffles+2)) (zgrid*
(Nbaffles+2))]
points1y = [0 ygridnew 0 (Int((ygridnew/2)+105)) 0 (Int((ygridnew/2)+1
05));0 ygridnew (Int((ygridnew/2)-95)) ygridnew (Int((ygridnew/2)-95))
ygridnew]

for i in 1:6
    plot3 = plot!(points1z[:,i], points1y[:,i], c=([:black]), line=4)
end

points2z = [0 0 0 0;(zgrid*(Nbaffles+2)) (zgrid*(Nbaffles+2)) (zgrid*(
```

```
Nbaffles+2)) (zgrid*(Nbaffles+2))]
points2y = [(Int((ygridnew/2)-145)) (Int((ygridnew/2)-95)) (Int((ygrid
new/2)+105)) (Int((ygridnew/2)+155));(Int((ygridnew/2)-145)) (Int((ygr
idnew/2)-95)) (Int((ygridnew/2)+105)) (Int((ygridnew/2)+155))]

for i in 1:4
    plot3 = plot!(points2z[:,i], points2y[:,i], c=([:black]), line=2,
legend=false)
end

plot!(grid=false, axis=nothing, border=:none, size = (950, 250))

savefig("TempDistSV.pdf")

@show plot3
```

In [ ]:

```
backend(:plotly)
xgrid = Int(Ncolumns)

T2xavg = ones(ygrid,(zgrid*(Nbaffles+2)),1)

for i in 1:ygrid
    for k in 1:(zgrid*(Nbaffles+2))
        temp = 0.0
        for j in 1:Ncolumns
            temp = temp + T2[i,k,j]
        end
        T2xavg[i,k,1] = temp/Ncolumns
    end
end

Tsxavg = ones(ygrid,(zgrid*(Nbaffles+2)),1)

for i in 1:ygrid
    for k in 1:(zgrid*(Nbaffles+2))
        temp = 0.0
        for j in 1:Ncolumns
            temp = temp + Ts[i,k,j]
        end
        Tsxavg[i,k,1] = temp/Ncolumns
    end
end

Tsoxavg = ones(ygrid,(zgrid*(Nbaffles+2)),1)

for i in 1:ygrid
    for k in 1:(zgrid*(Nbaffles+2))
        temp = 0.0
        for j in 1:Ncolumns
```

```
            temp = temp + Tso[i,k,j]
        end
        Tsoxavg[i,k,1] = temp/Ncolumns
    end
end

Tsixavg = ones(ygrid,(zgrid*(Nbaffles+2)),1)

for i in 1:ygrid
    for k in 1:(zgrid*(Nbaffles+2))
        temp = 0.0
        for j in 1:Ncolumns
            temp = temp + Tsi[i,k,j]
        end
        Tsixavg[i,k,1] = temp/Ncolumns
    end
end

xgridnew = Int(xgrid*20)
totTxz = ones(ygrid,(zgrid*(Nbaffles+2)),xgridnew)

for j in 1:ygrid
    for k in 1:(zgrid*(Nbaffles+2))
        for it in 1:xgridnew

            if it>11
                i = Int(round((it/20),digits=0))
            else
                i = 1
            end

            if i<(Int(round((xgrid/2)-(Int(round(((xgrid/10)+1),digits
=0))),digits=0))) || i>(Int(round((xgrid/2)+(Int(round(((xgrid/10)+1),
digits=0))),digits=0)))
                totTxz[j,k,it] = T1updated[j,k,i]
            elseif i==(Int(round((xgrid/2)-(Int(round(((xgrid/10)+1),d
igits=0))),digits=0))) || i==(Int(round((xgrid/2)+(Int(round(((xgrid/1
0)+1),digits=0))),digits=0)))
                totTxz[j,k,it] = Tsoxavg[j,k,1]
            elseif i==(Int(round((xgrid/2)-(Int(round(((xgrid/10)+0),d
igits=0)))-0.5,digits=0))) || i==(Int(round((xgrid/2)+(Int(round(((xgr
id/10)+0),digits=0)))+0.5,digits=0)))
                totTxz[j,k,it] = Tsixavg[j,k,1]
            else
                totTxz[j,k,it] = T2xavg[j,k,1]
            end


        end
    end
```

```
end
```

In [ ]:

```
backend(:plotly)
### xgridnew = Int(xgrid*20)
xs = [string("Ny ",i) for i in 1:xgridnew]
zs = [string("Nz ",i) for i in 1:(zgrid*(Nbaffles+2))]
plot2 = heatmap(zs, xs, totTxz[8,:,:], transpose=true, yflip=false, c=
cgrad([:blue4,:blue1,:cornflowerblue,:aqua,:aquamarine3,:lime,:yellow,
:orange,:red,:maroon]))

pointsz = ones(2,(Nbaffles+1))
pointsx = ones(2,(Nbaffles+1))

for i in 1:(Nbaffles+1)
    pointsz[1,i] = i*ygrid
    pointsz[2,i] = i*ygrid

    if iseven(i)
        pointsx[1,i] = xgridnew
        pointsx[2,i] = 0
    else
        pointsx[1,i] = 0
        pointsx[2,i] = xgridnew
    end
end

for i in 1:(Nbaffles+1)
    plot2 = plot!(pointsz[:,i], pointsx[:,i], c=([:black]), line=4)
end

points1z = [0 0 0 0 (zgrid*(Nbaffles+2)) (zgrid*(Nbaffles+2));(zgrid*(
Nbaffles+2)) (zgrid*(Nbaffles+2)) 0 0 (zgrid*(Nbaffles+2)) (zgrid*(Nba
ffles+2))]
points1y = [0 xgridnew 0 ((Int(round((xgrid/2)+(Int(round(((xgrid/10)+
1),digits=0))),digits=0)))-0.5)*20 0 ((Int(round((xgrid/2)+(Int(round(
((xgrid/10)+1),digits=0))),digits=0)))-0.5)*20;0 xgridnew ((Int(round(
(xgrid/2)-(Int(round(((xgrid/10)+1),digits=0))),digits=0)))+0.5)*20 xg
ridnew ((Int(round((xgrid/2)-(Int(round(((xgrid/10)+1),digits=0))),dig
its=0)))+0.5)*20 xgridnew]

for i in 1:6
    plot2 = plot!(points1z[:,i], points1y[:,i], c=([:black]), line=4)
end

points2x = [0 0 0 0;(zgrid*(Nbaffles+2)) (zgrid*(Nbaffles+2)) (zgrid*(
Nbaffles+2)) (zgrid*(Nbaffles+2))]
points2z = [((Int(round((xgrid/2)-(Int(round(((xgrid/10)+1),digits=0))
),digits=0)))-0.5)*20 ((Int(round((xgrid/2)-(Int(round(((xgrid/10)+1),
digits=0))),digits=0)))+0.5)*20 ((Int(round((xgrid/2)+(Int(round(((xgr
```

```
id/10)+1),digits=0))),digits=0)))-0.5)*20 ((Int(round((xgrid/2)+(Int(r
ound(((xgrid/10)+1),digits=0))),digits=0)))+0.5)*20;((Int(round((xgrid
/2)-(Int(round(((xgrid/10)+1),digits=0))),digits=0)))-0.5)*20 ((Int(ro
und((xgrid/2)-(Int(round(((xgrid/10)+1),digits=0))),digits=0)))+0.5)*2
0 ((Int(round((xgrid/2)+(Int(round(((xgrid/10)+1),digits=0))),digits=0
)))-0.5)*20 ((Int(round((xgrid/2)+(Int(round(((xgrid/10)+1),digits=0))
),digits=0)))+0.5)*20]

for i in 1:4
    plot2 = plot!(points2x[:,i], points2z[:,i], c=([:black]), line=2,
legend=false)
end

plot!(grid=false, axis=nothing, border=:none, size = (950, 250))

savefig("TempDistTV.pdf")

@show plot2
```

In [ ]:

```
backend(:gr)

PExt = ones((2*Nbaffles)+4)
i = 1
while i<=((2*Nbaffles)+4)
    if i==1
        PExt[i] = EPin
        i = i + 1
    else
        PExt[i] = PExt[i-1] - DpTB[Int(Nbaffles+3-(i/2))]
        if i != (Int((2*Nbaffles)+4))
            PExt[i+1] = PExt[i] - DpW[Int(Nbaffles+2-(i/2))]
        end
        i = i + 2
    end
end
LocExt = range(1,(Int((2*Nbaffles)+4));step=1)
PExt = PExt/100000

Pspace = ((PExt[1]-(PExt[(2*Nbaffles)+4]))/5)
Pticks = ones(6)
for i in 1:5
    if i == 1
        Pticks[i] = round(PExt[(2*Nbaffles)+4],digits=3)
    else
        Pticks[i] = round(Pticks[i-1]+Pspace,digits=3)
    end
end
Pticks[6] = round(EPin/100000,digits=3)

p1 = plot(LocExt,PExt; line=:scatter, markershape=:circle, markeralpha
=1.0, markercolor=:maroon, grid=false, xlabel="Unit cell location", yl
abel="External flow pressure [bar]", label="", framestyle = :box, tick
font=font(9),guidefont=font(9))
p1 = ylims!((PExt[(2*Nbaffles)+4]-0.02),PExt[1]+0.01)
p1 = yticks!(Pticks)
p1 = xlims!((0,(2*Nbaffles)+5))
p1 = xticks!(1:(2*Nbaffles)+4)
p1 = plot!(size=(950,380))

# savefig("ExternalPressurePlot.pdf")

print(PExt)

@show p1
```

In [ ]:

```
backend(:gr)

PInt = ones(Int(Nbaffles+5))
i = 1
while i<=(Int(Nbaffles+5))
    if i==1
        PInt[i] = IPin
    elseif i==2 || i==(Nbaffles+5)
        PInt[i] = PInt[i-1] - (DpCE/2)
    else
        PInt[i] = PInt[i-1] - DpInt[i-2]
    end
    i = i + 1
end
LocInt = range(1,(Int(Nbaffles+5));step=1)
PInt = PInt/100000

PIspace = ((PInt[1]-(PInt[Nbaffles+5]))/5)
PIticks = ones(6)
for i in 1:5
    if i == 1
        PIticks[i] = round(PInt[Nbaffles+5],digits=3)
    else
        PIticks[i] = round(PIticks[i-1]+PIspace,digits=3)
    end
end
PIticks[6] = round(IPin/100000,digits=3)

p2 = plot(LocInt,PInt; line=:scatter, markershape=:circle, markeralpha
=1.0, markercolor=:maroon, grid=false, xlabel="Unit cell location", yl
abel="Internal flow pressure [bar]", label="", framestyle = :box, tick
font=font(9),guidefont=font(9))
p2 = ylims!((PInt[Nbaffles+5]-0.05),PInt[1]+0.05)
p2 = yticks!(PIticks)
p2 = xlims!((0,Nbaffles+6))
p2 = xticks!(1:Nbaffles+5)
p2 = plot!(size=(950,400))

print(PInt)

# savefig("InternalPressurePlot.pdf")

@show p2
```

Appendix B: sCO_2-air MT-STHX experimental datasets

The datasets obtained from the experiments detailed in Chapter 4 are provided in this chapter.

Table B.1: Thermohydraulic test data with internal (sCO_2) mass flow rate at 12 g/s.

Case	External flow (air)						Internal flow (sCO_2)					
	$\dot{m}_e$ [g/s]	Re_e	T_{ei} [°C]	P_{ei} [kPa]	T_{eo} [°C]	P_{eo} [kPa]	$\dot{m}_i$ [g/s]	Re_i	T_{ii} [°C]	P_{ii} [MPa]	T_{io} [°C]	P_{io} [MPa]
1-01	5	1308	166.7	2.8	78.02	0.7	12	9796	68.2	10.29	86.4	10.25
1-02	10	2580	166.3	8.3	92.41	2.8	12	9813	68.2	10.31	100.6	10.27
1-03	15	3846	162.1	17.9	102.96	5.5	12	9817	68.3	10.29	108.0	10.25
1-04	20	5112	158.4	29.6	109.89	9.7	12	9826	68.3	10.26	112.2	10.22
1-05	25	6392	153.9	42.1	113.73	13.8	12	9810	68.5	10.29	113.7	10.25
1-06	30	7668	151.3	56.5	116.6	19.3	12	9807	68.5	10.29	114.8	10.25
1-07	35	9150	134.4	71.0	108.71	26.2	12	9842	68.4	10.26	106.4	10.23
1-08	40	10777	117.4	86.2	94.25	33.8	12	9390	58.6	10.28	89.7	10.25
1-09	45	12295	108.0	101.3	89.4	40.7	12	9385	58.5	10.26	85.1	10.23

The data in this section has been published as "Jin, Kaiyuan; Krishna, Akshay Bharadwaj; Wong, Zachary; Fisher, Timothy; Ayyaswamy, Portonovo; Catton, Ivan (2022), "Thermohydraulic experimental data for a supercritical carbon dioxide - air microtube heat exchanger", Mendeley Data, V1, doi: 10.17632/mn2wwp9r23.1"

Table B.2: Thermohydraulic test data with internal (sCO_2) mass flow rate at 15 g/s.

Case	External flow (air)						Internal flow (sCO_2)					
	$\dot{m}_e$ [g/s]	Re_e	T_{ei} [°C]	P_{ei} [kPa]	T_{eo} [°C]	P_{eo} [kPa]	$\dot{m}_i$ [g/s]	Re_i	T_{ii} [°C]	P_{ii} [MPa]	T_{io} [°C]	P_{io} [MPa]
2-01	5	1310	166.9	2.1	76.2	0.7	15	12132	67.8	10.36	82.2	10.33
2-02	10	2592	166.2	8.3	88.1	2.8	15	12190	68.1	10.39	94.7	10.35
2-03	15	3867	162	17.9	97.4	5.5	15	12206	68.2	10.38	101.7	10.35
2-04	20	5141	158.25	29.6	104.0	9.7	15	12202	68.2	10.38	106.1	10.35
2-05	25	6425	153.9	42.7	108.2	14.5	15	12185	68.3	10.40	108.2	10.37
2-06	30	7705	151.18	57.2	111.5	20.0	15	12193	68.3	10.39	109.8	10.35
2-07	35	9187	134.14	71.0	104.7	26.2	15	12209	68.3	10.38	102.4	10.35
2-08	40	10822	116.87	85.5	90.5	33.1	15	11585	58.5	10.39	85.7	10.35
2-09	45	12340	107.52	100.7	86.2	41.4	15	11536	58.2	10.38	81.8	10.35

Table B.3: Thermohydraulic test data with internal (sCO_2) mass flow rate at 15 g/s.

Case	External flow (air)						Internal flow (sCO_2)					
	$\dot{m}_e$ [g/s]	Re_e	T_{ei} [°C]	P_{ei} [kPa]	T_{eo} [°C]	P_{eo} [kPa]	$\dot{m}_i$ [g/s]	Re_i	T_{ii} [°C]	P_{ii} [MPa]	T_{io} [°C]	P_{io} [MPa]
3-01	5	1313	166.7	2.1	73.9	0.7	18	14402	67.1	10.43	78.8	10.39
3-02	10	2600	166.3	8.3	84.8	2.1	18	14548	67.6	10.43	89.9	10.39
3-03	15	3881	162.3	17.2	93.4	5.5	18	14567	67.9	10.45	96.8	10.41
3-04	20	5160	158.2	29.6	100.0	9.7	18	14593	68.0	10.43	101.3	10.40
3-05	25	6452	153.7	41.4	104.0	13.8	18	14568	68.1	10.46	104.0	10.42
3-06	30	7732	151.2	56.5	107.6	19.3	18	14580	68.2	10.45	105.7	10.41
3-07	35	9210	134.5	71.7	101.7	26.2	18	14576	68.0	10.45	99.2	10.41

Case	External flow (air)						Internal flow (sCO_2)					
	$\dot{m}_e$ [g/s]	Re_e	T_{ei} [°C]	P_{ei} [kPa]	T_{eo} [°C]	P_{eo} [kPa]	$\dot{m}_i$ [g/s]	Re_i	T_{ii} [°C]	P_{ii} [MPa]	T_{io} [°C]	P_{io} [MPa]
3-08	40	10853	116.9	86.2	87.7	33.1	18	13965	58.1	10.30	82.9	10.26
3-09	45	12356	108.2	100.7	84.3	40.7	18	13775	58.0	10.39	79.7	10.36

Table B.4: Thermohydraulic test data with internal (sCO_2) mass flow rate at 15 g/s.

Case	External flow (air)						Internal flow (sCO_2)					
	$\dot{m}_e$ [g/s]	Re_e	T_{ei} [°C]	P_{ei} [kPa]	T_{eo} [°C]	P_{eo} [kPa]	$\dot{m}_i$ [g/s]	Re_i	T_{ii} [°C]	P_{ii} [MPa]	T_{io} [°C]	P_{io} [MPa]
4-01	5	1315	166.6	2.8	72.3	0.7	21	16626	66.3	10.48	76.1	10.43
4-02	10	2607	166.0	8.3	82.0	2.8	21	16789	67.0	10.52	85.9	10.47
4-03	15	3895	162.1	17.2	89.9	5.5	21	16866	67.4	10.52	92.4	10.48
4-04	20	5176	158.9	29.0	96.3	9.0	21	16943	67.6	10.48	97.2	10.44
4-05	25	6471	154.0	41.4	100.5	13.8	21	16899	67.8	10.53	99.6	10.49
4-06	30	7753	151.8	56.5	104.2	18.6	21	16923	67.9	10.52	102.0	10.47
4-07	35	9238	134.5	70.3	98.7	25.5	21	16899	67.6	10.52	96.9	10.47
4-08	40	10878	117.2	85.5	85.1	33.1	21	15992	57.8	10.47	80.1	10.43
4-09	45	12390	108.0	100.0	81.8	40.7	21	15847	57.5	10.45	77.0	10.41

Table B.5: Thermohydraulic test data with internal (sCO_2) mass flow rate at 15 g/s.

Case	$\dot{m}_e$ [g/s]	Re_e	T_{ei} [°C]	P_{ei} [kPa]	T_{eo} [°C]	P_{eo} [kPa]	ΔP_1 [kPa]	ΔP_2 [kPa]	ΔP_3 [kPa]	ΔP_4 [kPa]	ΔP_5 [kPa]
5-01	5	2060	20.0	1.37	19.9	0.23	0.19	0.19	0.20	0.23	0.77
5-02	10	4120	20.0	6.21	19.9	2.06	0.38	0.72	0.74	0.86	1.87

Case	$\dot{m}_e$ [g/s]	Re_e	T_{ei} [°C]	P_{ei} [kPa]	T_{eo} [°C]	P_{eo} [kPa]	ΔP_1 [kPa]	ΔP_2 [kPa]	ΔP_3 [kPa]	ΔP_4 [kPa]	ΔP_5 [kPa]
5-03	15	6182	19.9	13.10	19.7	4.54	0.72	1.48	1.52	1.82	3.26
5-04	20	8246	19.7	21.37	19.5	7.25	1.18	2.40	2.47	3.01	4.76
5-05	25	10309	19.6	32.41	19.3	12.24	1.72	3.42	3.55	4.34	6.72
5-06	30	12375	19.5	43.44	19.0	16.94	2.21	4.43	4.62	5.72	8.99
5-07	35	14459	18.9	55.85	18.3	22.74	3.79	5.38	5.70	7.05	10.89
5-08	40	16532	18.5	58.61	18.5	51.75	4.83	6.44	6.86	8.49	13.25
5-09	45	18608	18.3	69.64	18.3	61.63	5.86	7.43	8.01	9.87	15.47

References

[1] Yoonhan Ahn et al. "Review of supercritical CO_2 power cycle technology and current status of research and development". In: *Nuclear engineering and technology* 47.6 (2015), pp. 647–661.

[2] M.A. Reyes-Belmonte et al. "Optimization of a recompression supercritical carbon dioxide cycle for an innovative central receiver solar power plant". In: *Energy* 112 (2016), pp. 17–27. ISSN: 0360-5442. DOI: 10.1016/j.energy.2016.06.013.

[3] John Dyreby et al. "Design Considerations for Supercritical Carbon Dioxide Brayton Cycles With Recompression". In: *Journal of Engineering for Gas Turbines and Power* 136.10 (July 2014). 101701. ISSN: 0742-4795. DOI: 10.1115/1.4027936.

[4] Yaping Liu, Ying Wang, and Diangui Huang. "Supercritical CO_2 Brayton cycle: A state-of-the-art review". In: *Energy* 189 (2019), p. 115900.

[5] Thomas Conboy et al. "Performance characteristics of an operating supercritical CO_2 Brayton cycle". In: *Turbo Expo: Power for Land, Sea, and Air* Volume 5: Manufacturing Materials and Metallurgy; Marine; Microturbines and Small Turbomachinery; Supercritical CO_2 Power Cycles (June 2012), pp. 941–952. DOI: 10.1115/GT2012-68415.

[6] Craig S Turchi et al. "Thermodynamic study of advanced supercritical carbon dioxide power cycles for concentrating solar power systems". In: *Journal of Solar Energy Engineering* 135.4 (2013).

[7] Michael Persichilli et al. "Supercritical CO_2 power cycle developments and commercialization: why sCO_2 can displace steam ste". In: *Power-Gen India & Central Asia* 2012 (2012), pp. 19–21.

[8] Jason D Miller et al. "Comparison of supercritical CO_2 power cycles to steam Rankine cycles in coal-fired applications". In: *Turbo Expo: Power for Land, Sea, and Air*. Vol. 50961. American Society of Mechanical Engineers. 2017, V009T38A026.

[9] Dia Milani et al. "Optimizing an advanced hybrid of solar-assisted supercritical CO_2 Brayton cycle: a vital transition for low-carbon power generation industry". In: *Energy Conversion and Management* 148 (2017), pp. 1317–1331.

[10] Mounir Mecheri and Yann Le Moullec. "Supercritical CO_2 Brayton cycles for coal-fired power plants". In: *Energy* 103 (2016), pp. 758–771. ISSN: 0360-5442. DOI: 10.1016/j.energy.2016.02.111.

[11] Heyang Miao, Zhongwei Wang, and Yaobin Niu. "Performance analysis of cooling system based on improved supercritical CO_2 Brayton cycle for scramjet". In: *Applied Thermal Engineering* 167 (2020), p. 114774. ISSN: 1359-4311. DOI: 10.1016/j.applthermaleng.2019.114774.

[12] Jan Syblik et al. "Analysis of supercritical CO_2 Brayton power cycles in nuclear and fusion energy". In: *Fusion Engineering and Design* 146 (2019). SI:SOFT-30, pp. 1520–1523. ISSN: 0920-3796. DOI: 10.1016/j.fusengdes.2019.02.119.

[13] Ali Sulaiman Alsagri, Andrew Chiasson, and Mohamed Gadalla. "Viability assessment of a concentrated solar power tower with a supercritical CO_2 Brayton cycle power plant". In: *Journal of Solar Energy Engineering* 141.5 (2019).

[14] Yann Le Moullec. "Conceptual study of a high efficiency coal-fired power plant with CO_2 capture using a supercritical CO_2 Brayton cycle". In: *Energy* 49 (2013), pp. 32–46.

[15] Florian Jacob et al. "Performance of a supercritical CO_2 bottoming cycle for aero applications". In: *Applied Sciences* 7.3 (2017), p. 255.

[16] Brian D Iverson et al. "Supercritical CO_2 Brayton cycles for solar-thermal energy". In: *Applied Energy* 111 (2013), pp. 957–970.

[17] Elisa Guelpa and Vittorio Verda. "Exergoeconomic analysis for the design improvement of supercritical CO_2 cycle in concentrated solar plant". In: *Energy* 206 (2020), p. 118024.

[18] Xurong Wang and Yiping Dai. "Exergoeconomic analysis of utilizing the transcritical CO_2 cycle and the ORC for a recompression supercritical CO_2 cycle waste heat recovery: A comparative study". In: *Applied energy* 170 (2016), pp. 193–207.

[19] Jian Song et al. "Performance improvement of a preheating supercritical CO_2 (S-CO_2) cycle based system for engine waste heat recovery". In: *Energy Conversion and Management* 161 (2018), pp. 225–233.

[20] Jin Su Kwon et al. "Compact heat exchangers for supercritical CO_2 power cycle application". In: *Energy Conversion and Management* 209 (2020), p. 112666. ISSN: 0196-8904. DOI: 10.1016/j.enconman.2020.112666.

[21] Jacob F Hinze, Gregory F Nellis, and Mark H Anderson. "Cost comparison of printed circuit heat exchanger to low cost periodic flow regenerator for use as recuperator in a

s-CO_2 Brayton cycle". In: *Applied energy* 208 (2017), pp. 1150–1161. DOI: 10.1016/j.apenergy.2017.09.037.

[22] Alan Kruizenga et al. "Supercritical carbon dioxide heat transfer in horizontal semicircular channels". In: *Journal of Heat transfer* 134.8 (2012).

[23] Brian M Fronk and Alexander S Rattner. "High-flux thermal management with supercritical fluids". In: *Journal of Heat Transfer* 138.12 (2016).

[24] Jiangfeng Guo and Xiulan Huai. "Performance analysis of printed circuit heat exchanger for supercritical carbon dioxide". In: *Journal of Heat Transfer* 139.6 (2017).

[25] Eric M Clementoni, Timothy L Cox, and Martha A King. "Response of a compact recuperator to thermal transients in a supercritical carbon dioxide Brayton cycle". In: *Turbo Expo: Power for Land, Sea, and Air*. Vol. 50961. 2017, V009T38A002.

[26] Tianrui Deng et al. "Dynamic modelling and transient characteristics of supercritical CO_2 recompression Brayton cycle". In: *Energy* 180 (2019), pp. 292–302.

[27] Chien-Yuh Yang and Kun-Chieh Liao. "Effect of experimental method on the heat transfer performance of supercritical carbon dioxide in microchannel". In: *Journal of Heat Transfer* 139.11 (2017).

[28] SM Liao and TS Zhao. "Measurements of heat transfer coefficients from supercritical carbon dioxide flowing in horizontal mini/micro channels". In: *J. Heat Transfer* 124.3 (2002), pp. 413–420.

[29] Qi Li et al. "Compact heat exchangers: A review and future applications for a new generation of high temperature solar receivers". In: *Renewable and Sustainable Energy Reviews* 15.9 (2011), pp. 4855–4875.

[30] Ji Hwan Jeong et al. "Review of heat exchanger studies for high-efficiency gas turbines". In: *Turbo Expo: Power for Land, Sea, and Air*. Vol. 47934. 2007, pp. 833–840.

[31] Donato Aquaro and MJATE Pieve. "High temperature heat exchangers for power plants: Performance of advanced metallic recuperators". In: *Applied Thermal Engineering* 27.2-3 (2007), pp. 389–400.

[32] Bong Yoo, Ronald F Kulak, and Yun-Jae Kim. "Pressure and thermal stress analyses of a generation IV reactor system, mini-channel heat exchanger". In: *International Conference on Nuclear Engineering*. Vol. 42444. 2006, pp. 167–171.

[33] Motoaki Utamura. "Thermal-hydraulic characteristics of microchannel heat exchanger and its application to solar gas turbines". In: *Turbo Expo: Power for Land, Sea, and Air*. Vol. 47934. 2007, pp. 287–294.

[34] Guangxu Liu et al. "A review on the thermal-hydraulic performance and optimization of printed circuit heat exchangers for supercritical CO_2 in advanced nuclear power systems". In: *Renewable and Sustainable Energy Reviews* 133 (2020), p. 110290.

[35] Ajinkya Meshram et al. "Modeling and analysis of a printed circuit heat exchanger for supercritical CO_2 power cycle applications". In: *Applied Thermal Engineering* 109 (2016), pp. 861–870.

[36] Zhuo Ren et al. “Local Flow and Heat Transfer of Supercritical CO_2 in Semicircular Zigzag Channels of Printed Circuit Heat Exchanger during Cooling”. In: *Heat Transfer Engineering* 42.22 (2021), pp. 1889–1913.

[37] Muhammad Saeed and Man-Hoe Kim. “Thermal and hydraulic performance of SCO_2 PCHE with different fin configurations”. In: *Applied thermal engineering* 127 (2017), pp. 975–985.

[38] Xiao Long Li et al. “Numerical analysis of slotted airfoil fins for printed circuit heat exchanger in S-CO_2 Brayton cycle”. In: *Journal of Nuclear Engineering and Radiation Science* 5.4 (2019).

[39] Keyong Cheng et al. “Experimental investigation of thermal-hydraulic characteristics of a printed circuit heat exchanger used as a pre-cooler for the supercritical CO_2 Brayton cycle”. In: *Applied Thermal Engineering* 171 (2020), p. 115116.

[40] Joo Hyun Park et al. “Experimental study of a straight channel printed circuit heat exchanger on supercritical CO_2 near the critical point with water cooling”. In: *International Journal of Heat and Mass Transfer* 150 (2020), p. 119364.

[41] Huzhong Zhang et al. “Experimental and Numerical Study of an 80-kW Zigzag Printed Circuit Heat Exchanger for Supercritical CO_2 Brayton Cycle”. In: *Journal of Thermal Science* 30.4 (2021), pp. 1289–1301.

[42] Wenxiao Chu et al. “Experimental study on small scale printed circuit heat exchanger with zigzag channels”. In: *Heat Transfer Engineering* 42.9 (2021), pp. 723–735.

[43] Yuan Jiang et al. "Optimal design of microtube recuperators for an indirect supercritical carbon dioxide recompression closed Brayton cycle". In: *Applied energy* 216 (2018), pp. 634–648.

[44] M Monjurul Ehsan et al. "Design and comparison of direct and indirect cooling system for 25 MW solar power plant operated with supercritical CO_2 cycle". In: *Energy conversion and management* 168 (2018), pp. 611–628.

[45] Ramesh K Shah and Dusan P Sekulic. *Fundamentals of heat exchanger design*. John Wiley & Sons, 2003.

[46] Kuppan Thulukkanam. *Heat exchanger design handbook*. CRC press, 2000.

[47] Resat Selbaş, Önder Kızılkan, and Marcus Reppich. "A new design approach for shell-and-tube heat exchangers using genetic algorithms from economic point of view". In: *Chemical Engineering and Processing: Process Intensification* 45.4 (2006), pp. 268–275. ISSN: 0255-2701. DOI: 10.1016/j.cep.2005.07.004.

[48] Mohsen Mirzaei, Hassan Hajabdollahi, and Hadi Fadakar. "Multi-objective optimization of shell-and-tube heat exchanger by constructal theory". In: *Applied Thermal Engineering* 125 (2017), pp. 9–19. ISSN: 1359-4311. DOI: 10.1016/j.applthermaleng.2017.06.137.

[49] Simin Wang, Jian Wen, and Yanzhong Li. "An experimental investigation of heat transfer enhancement for a shell-and-tube heat exchanger". In: *Applied Thermal Engineering* 29.11 (2009), pp. 2433–2438. ISSN: 1359-4311. DOI: 10.1016/j.applthermaleng.2008.12.008.

[50] Tubular Exchanger Manufacturers Association. *Standard of Tubular Exchanger Manufacturers Association*. Tech. rep. Tubular Exchanger Manufacturers Association, 2019.

[51] Lalit Chordia, Marc A Portnoff, and Ed Green. *High temperature heat exchanger design and fabrication for systems with large pressure differentials*. Tech. rep. Thar Energy, LLC, Pittsburgh, PA (United States), 2017. DOI: 10.2172/1349235.

[52] Hao-fei Cai et al. "Experimental investigation on convective heat transfer and pressure drop of supercritical CO_2 and water in microtube heat exchangers". In: *International Journal of Heat and Mass Transfer* 163 (2020), p. 120443.

[53] Tracey Ziev et al. "Economics of an Additive Manufactured Heat Exchanger for Concentrating Solar Power". In: (2022).

[54] Kyle A Rozman et al. *Performance of Ni-superalloy Haynes 282 with exposure to supercritical gases*. Tech. rep. NETL, 2016.

[55] KL Kruger. "HAYNES 282 alloy". In: *Materials for ultra-supercritical and advanced ultra-supercritical power plants*. Elsevier, 2017, pp. 511–545.

[56] Brice Cassenti and Alexander Staroselsky. "The effect of thickness on the creep response of thin-wall single crystal components". In: *Materials Science and Engineering: A* 508.1-2 (2009), pp. 183–189.

[57] BS Petukhov. "Heat transfer and friction in turbulent pipe flow with variable physical properties". In: *Advances in heat transfer*. Vol. 6. Elsevier, 1970, pp. 503–564.

[58] Volker Gnielinski. “New equations for heat and mass transfer in turbulent pipe and channel flow”. In: *Int. Chem. Eng.* 16.2 (1976), pp. 359–368.

[59] A Zukauskas. *Air cooled heat exchangers*. McGraw-Hill New York, 1981, pp. 49–83.

[60] TH Hwang and SC Yao. “A simple heat transfer correlation for cross flow in tube bundles”. In: *International communications in heat and mass transfer* 13.1 (1986), pp. 3–10.

[61] ED Grimson. “Correlation and utilization of new data on flow resistance and heat transfer cross-flow of gases over tube banks”. In: *Trans. ASME* 59 (1937), pp. 583–594.

[62] Orville L Pierson. “Experimental investigation of the influence of tube arrangement on convection heat transfer and flow resistance in cross flow of gases over tube banks”. In: *Trans. ASME* 59.7 (1937), pp. 563–572.

[63] R Gregorig. *Wärmeaustauscher, HR Sauerlander & Co.* 1959.

[64] William Morrow Kays and Alexander Louis London. *Compact heat exchangers*. McGraw-Hill, New York, NY, 1984.

[65] A Žukauskas. “Heat transfer from tubes in crossflow”. In: *Advances in heat transfer*. Vol. 8. Elsevier, 1972, pp. 93–160.

[66] Max Jakob. “Heat transfer and flow resistance in cross flow of gases over tube bank”. In: *Trans. ASME* 60 (1938), p. 384.

[67] AY Gunter, WA Shaw, et al. “A general correlation of friction factors for various types of surfaces in cross flow”. In: *trans. ASME* 67.8 (1945), pp. 643–660.

[68] DF Boucher and CE Lapple. "Pressure Drop Across Tube Banks-Critical Comparison of Available Data and of Proposed Methods of Correlation". In: *Chemical Engineering Progress* 44.2 (1948), pp. 117–134.

[69] Arthur E Bergles. *Techniques to augment heat transfer. Handbook of heat transfer.(A 74-17085 05-33) New York*. Vol. 1973. 1973, p. 10.

[70] Arthur E Bergles. *The imperative to enhance heat transfer*. Springer, 1999, pp. 13–29.

[71] S.M. Yang and W.Q. Tao. *Heat transfer*. 4th Edition. Beijing: Higher Education Press, 2006.

[72] Kai-Shing Yang et al. "A comparative study of the airside performance of heat sinks having pin fin configurations". In: *International Journal of Heat and Mass Transfer* 50.23-24 (2007), pp. 4661–4667.

[73] ON Şara. "Performance analysis of rectangular ducts with staggered square pin fins". In: *Energy Conversion and Management* 44.11 (2003), pp. 1787–1803.

[74] En Tian, Ya-Ling He, and Wen-Quan Tao. "Numerical simulation of finned tube bank across a staggered circular-pin-finned tube bundle". In: *Numerical Heat Transfer, Part A: Applications* 68.7 (2015), pp. 737–760.

[75] N Sahiti et al. "Performance comparison of pin fin in-duct flow arrays with various pin cross-sections". In: *Applied Thermal Engineering* 26.11-12 (2006), pp. 1176–1192.

[76] JC Biery. "Prediction of heat transfer coefficients in gas flow normal to finned and smooth tube banks". In: (1981).

[77] Z Mirkovic. "Heat transfer and flow resistance correlation for helically finned and staggered tube banks in cross flow". In: *Heat exchangers: design and theory source book* (1974), pp. 559–584.

[78] Feng Zhou. "Development of Closure for Heat Exchangers Based on Volume Averaging Theory". PhD thesis. University of California, Los Angeles, 2014.

[79] NH Kim, B Youn, and RL Webb. "Air-side heat transfer and friction correlations for plain fin-and-tube heat exchangers with staggered tube arrangements". In: *Journal of Heat Transfer* 121.3 (1999).

[80] Feng Zhou and Ivan Catton. "Volume Averaging Theory (VAT) based modeling and closure evaluation for fin-and-tube heat exchangers". In: *Heat and Mass Transfer* 48.10 (2012), pp. 1813–1823.

[81] Akshay Bharadwaj Krishna et al. *akshayb29/Shell-and-Tube-Heat-Exchanger-STHX-numerical-model: Shell-and-tube heat exchanger numerical model*. July 2021. DOI: 10.5281/zenodo.5117859.

[82] Akshay Bharadwaj Krishna et al. "Modeling of Supercritical CO_2 Shell-and-Tube Heat Exchangers Under Extreme Conditions: Part II: Heat Exchanger Model". In: *Journal of Heat Transfer* 144.5 (Mar. 2022). ISSN: 0022-1481. DOI: 10.1115/1.4053511.

[83] Yonghua You et al. "Numerical modeling and experimental validation of heat transfer and flow resistance on the shell side of a shell-and-tube heat exchanger with flower baffles". In: *International Journal of Heat and Mass Transfer* 55.25 (2012), pp. 7561–7569. ISSN: 0017-9310. DOI: 10.1016/j.ijheatmasstransfer.2012.07.058.

[84] S V Patankar and D B Spalding. "A calculation procedure for the transient and steady-state behavior of shell-and-tube heat exchangers". In: *Heat exchangers: Design and Theory Sourcebook* 1 (1974).

[85] D. Butterworth. "The development of a model for three-dimensional flow in tube bundles". In: *International Journal of Heat and Mass Transfer* 21.2 (1978), pp. 253–256. ISSN: 0017-9310. DOI: 10.1016/0017-9310(78)90231-4.

[86] William T. Sha. "An overview on rod-bundle thermal-hydraulic analysis". In: *Nuclear Engineering and Design* 62 (1980), pp. 1–24.

[87] W. T. Sha et al. "Multidimensional numerical modeling of heat exchangers". In: *Journal of Heat Transfer* 104.3 (Aug. 1982), pp. 417–425. ISSN: 0022-1481. DOI: 10.1115/1.3245109.

[88] Donald Quentin Kern. *Process heat transfer*. Vol. 5. McGraw-Hill New York, 1950.

[89] K J Bell. "Delaware method for shell side design". In: *Heat Exchangers-Thermal Hydraulic Fundamentals and Design* (1981), pp. 581–618.

[90] Stephen Whitaker. *The method of volume averaging*. Vol. 13. Springer Science & Business Media, 2013.

[91] V.S. Travkin and I. Catton. "Porous media transport descriptions — non-local, linear and non-linear against effective thermal/fluid properties". In: *Advances in Colloid and Interface Science* 76-77 (1998), pp. 389–443. ISSN: 0001-8686. DOI: 10.1016/S0001-8686(98)00054-2.

[92] V. S. Travkin et al. "Transport Phenomena in Heterogeneous Media: Experimental Data Reduction and Analysis". In: vol. Application of Porous Media Methods for Engineered Materials. ASME International Mechanical Engineering Congress and Exposition. Nov. 1999, pp. 21–31. DOI: 10.1115/IMECE1999-0796.

[93] V. S. Travkin. "Relating Semiconductor Heat Sink Local and Non-Local Experimental and Simulation Data to Upper Scale Design Goals". In: vol. Heat Transfer: Volume 7 — Heat Transfer in Electronic Equipment, Student Research, and Visualization Techniques. ASME International Mechanical Engineering Congress and Exposition. Nov. 2001, pp. 101–112. DOI: 10.1115/IMECE2001/HTD-24383.

[94] Krsto Sbutega. "Modeling and optimization of spatially evolving heat sinks using volume averaging theory". PhD thesis. University of California, Los Angeles, 2015.

[95] Feng Zhou and Ivan Catton. "Numerical Evaluation of Flow and Heat Transfer in Plate-Pin Fin Heat Sinks with Various Pin Cross-Sections". In: *Numerical Heat Transfer, Part A: Applications* 60.2 (2011), pp. 107–128. DOI: 10.1080/10407782.2011.588574.

[96] Ivan Catton. "Conjugate Heat Transfer Within a Heterogeneous Hierarchical Structure". In: *Journal of Heat Transfer* 133.10 (Aug. 2011). 103001. ISSN: 0022-1481. DOI: 10.1115/1.4003576.

[97] Feng Zhou et al. "Obtaining closure for fin-and-tube heat exchanger modeling based on volume averaging theory (VAT)". In: *Journal of Heat Transfer* 133.11 (2011).

[98] David Geb et al. "Genetic algorithm optimization of a finned-tube heat exchanger modeled with volume-averaging theory". In: *Journal of heat transfer* 135.8 (2013).

[99] Frank P Incropera et al. *Fundamentals of heat and mass transfer*. Wiley, 2011.

[100] Isaak E Idelchik. "Handbook of hydraulic resistance". In: *Washington* (1986).

[101] Ian H Bell et al. "Pure and pseudo-pure fluid thermophysical property evaluation and the open-source thermophysical property library CoolProp". In: *Industrial & engineering chemistry research* 53.6 (2014), pp. 2498–2508.

[102] Haynes International. *Haynes International - HAYNES® 282® Alloy*. 2021. URL: http://haynesintl.com/docs/default-source/pdfs/new-alloy-brochures/high-temperature-alloys/brochures/282-brochure.pdf?sfvrsn=20..

[103] Akshay Bharadwaj Krishna et al. "Modeling of Supercritical CO_2 Shell-and-Tube Heat Exchangers Under Extreme Conditions. Part I: Correlation Development". In: *Journal of Heat Transfer* 144.5 (Mar. 2022). ISSN: 0022-1481. DOI: 10.1115/1.4053510.

[104] Rajiv Mukherjee et al. "Effectively design shell-and-tube heat exchangers". In: *Chemical Engineering Progress* 94.2 (1998), pp. 21–37.

[105] Hao-fei Cai et al. "Numerical investigation on heat transfer of supercritical carbon dioxide in the microtube heat exchanger at low reynolds numbers". In: *International Journal of Heat and Mass Transfer* 151 (2020), p. 119448.

[106] CE Taylor and IG Currie. "Sealing strips in tubular heat exchangers". In: (1987).

[107] David John Martin, MA Hollingworth, and VR Mayhew. "The effect of bypass lanes and sealing-strips in shell-and-tube heat exchangers". PhD thesis. University of Bristol, 1989.

[108] Joint Committee for Guides in Metrology. "Evaluation of measurement data—Guide to the expression of uncertainty in measurement". In: *JCGM* 100.2008 (2008), pp. 1–116.

[109] K. Muralikrishna and U.V. Shenoy. "Heat exchanger design targets for minimum area and cost". In: *Chemical Engineering Research and Design* 78.2 (2000), pp. 161–167. ISSN: 0263-8762. DOI: 10.1205/026387600527185.

[110] TK Poddar and GT Polley. "Heat exchanger design through parameter plotting". In: *Chemical Engineering Research and Design* 74.8 (1996), pp. 849–852.

[111] Benoît Allen and Louis Gosselin. "Optimal geometry and flow arrangement for minimizing the cost of shell-and-tube condensers". In: *International Journal of Energy Research* 32.10 (2008), pp. 958–969. DOI: 10.1002/er.1398.

[112] Kwasi Foli et al. "Optimization of micro heat exchanger: CFD, analytical approach and multi-objective evolutionary algorithms". In: *International Journal of Heat and Mass Transfer* 49.5-6 (2006), pp. 1090–1099. DOI: 10.1016/j.ijheatmasstransfer.2005.08.032.

[113] Renan Hilbert et al. "Multi-objective shape optimization of a heat exchanger using parallel genetic algorithms". In: *International Journal of Heat and Mass Transfer* 49.15 (2006), pp. 2567–2577. ISSN: 0017-9310. DOI: 10.1016/j.ijheatmasstransfer.2005.12.015.

[114] Antonio C. Caputo, Pacifico M. Pelagagge, and Paolo Salini. "Heat exchanger design based on economic optimisation". In: *Applied Thermal Engineering* 28.10 (2008), pp. 1151–1159. ISSN: 1359-4311. DOI: 10.1016/j.applthermaleng.2007.08.010.

[115] Arzu Şencan Şahin, Bayram Kılıç, and Ulaş Kılıç. "Design and economic optimization of shell and tube heat exchangers using Artificial Bee Colony (ABC) algorithm". In: *Energy Conversion and Management* 52.11 (2011), pp. 3356–3362. ISSN: 0196-8904. DOI: 10.1016/j.enconman.2011.07.003.

[116] R.V. Rao, V.J. Savsani, and D.P. Vakharia. "Teaching–learning-based optimization: An optimization method for continuous non-linear large scale problems". In: *Information Sciences* 183.1 (2012), pp. 1–15. ISSN: 0020-0255. DOI: 10.1016/j.ins.2011.08.006.

[117] R. Venkata Rao and Vivek Patel. "Multi-objective optimization of heat exchangers using a modified teaching-learning-based optimization algorithm". In: *Applied Mathematical Modelling* 37.3 (2013), pp. 1147–1162. ISSN: 0307-904X. DOI: 10.1016/j.apm.2012.03.043.

[118] Amin Hadidi, Mojtaba Hadidi, and Ali Nazari. "A new design approach for shell-and-tube heat exchangers using imperialist competitive algorithm (ICA) from economic point of view". In: *Energy Conversion and Management* 67 (2013), pp. 66–74. ISSN: 0196-8904. DOI: 10.1016/j.enconman.2012.11.017.

[119] Amin Hadidi and Ali Nazari. "Design and economic optimization of shell-and-tube heat exchangers using biogeography-based (BBO) algorithm". In: *Applied Thermal Engineering* 51.1 (2013), pp. 1263–1272. ISSN: 1359-4311. DOI: 10.1016/j.applthermaleng.2012.12.002.

[120] V.K. Patel and R.V. Rao. "Design optimization of shell-and-tube heat exchanger using particle swarm optimization technique". In: *Applied Thermal Engineering* 30.11

(2010), pp. 1417–1425. ISSN: 1359-4311. DOI: 10.1016/j.applthermaleng.2010.03.001.

[121] Viviana Cocco Mariani et al. "A chaotic quantum-behaved particle swarm approach applied to optimization of heat exchangers". In: *Applied Thermal Engineering* 42 (2012). Heat Powered Cycles Conference, 2009, pp. 119–128. ISSN: 1359-4311. DOI: 10.1016/j.applthermaleng.2012.03.022.

[122] E C Laskari, K E Parsopoulos, and M N Vrahatis. "Particle swarm optimization for minimax problems". In: *Proceedings of the 2002 Congress on Evolutionary Computation. CEC'02 (Cat. No. 02TH8600)*. Vol. 2. IEEE. 2002, pp. 1576–1581.

[123] Rong Ge et al. "Escaping from saddle points—online stochastic gradient for tensor decomposition". In: *Conference on learning theory*. PMLR. 2015, pp. 797–842.

[124] RK Shah and KJ Bell. *CRC handbook of thermal engineering*. 2000.

[125] Warren M Rohsenow, James P Hartnett, Young I Cho, et al. *Handbook of heat transfer*. Vol. 3. McGraw-Hill New York, 1998.

[126] Geoffrey Frederick Hewitt. *Heat exchanger design handbook*. Begell House, 1998.

[127] Jiangfeng Guo, Lin Cheng, and Mingtian Xu. "Optimization design of shell-and-tube heat exchanger by entropy generation minimization and genetic algorithm". In: *Applied Thermal Engineering* 29.14 (2009), pp. 2954–2960. ISSN: 1359-4311. DOI: 10.1016/j.applthermaleng.2009.03.011.

[128] JiangFeng Guo, Lin Cheng, and MingTian Xu. "Entransy dissipation number and its application to heat exchanger performance evaluation". In: *Chinese Science Bulletin* 54.15 (2009), pp. 2708–2713.

[129] Jiangfeng Guo, Mingtian Xu, and Lin Cheng. "The application of field synergy number in shell-and-tube heat exchanger optimization design". In: *Applied Energy* 86.10 (2009), pp. 2079–2087. ISSN: 0306-2619. DOI: 10.1016/j.apenergy.2009.01.013.

[130] G P Purohit. "Estimating costs of shell-and-tube heat exchangers". In: *Chemical engineering* 90.17 (1983), pp. 56–67.

[131] Arkadie Pikulik and H E Diaz. "Cost estimating for major process equipment". In: *Chemical engineering* (1977), pp. 106–122.

[132] K M Guthrie. "Capital cost estimating, Modern Cost Engineering Techniques". In: *Chemical engineering* (1969), pp. 114–142.

[133] Armando B Corripio, K S Chrien, and L B Evans. "Estimate costs of heat exchangers and storage tanks via correlations". In: *Chemical Engineering Magazine, Modern Cost Engineering II* (1984), pp. 144–146.

[134] Marcel Taal et al. "Cost estimation and energy price forecasts for economic evaluation of retrofit projects". In: *Applied Thermal Engineering* 23.14 (2003). Process Integration, Modelling and Optimisation for Energy Saving and Pollution Reduction, pp. 1819–1835. ISSN: 1359-4311. DOI: 10.1016/S1359-4311(03)00136-4.

[135] James Kennedy and Russell Eberhart. "Particle swarm optimization". In: *Proceedings of ICNN'95-international conference on neural networks*. Vol. 4. IEEE. 1995, pp. 1942–1948.

[136] Russell Eberhart and James Kennedy. "A new optimizer using particle swarm theory". In: *MHS'95. Proceedings of the Sixth International Symposium on Micro Machine and Human Science*. Ieee. 1995, pp. 39–43.

[137] Hanhong Zhu et al. "Particle Swarm Optimization (PSO) for the constrained portfolio optimization problem". In: *Expert Systems with Applications* 38.8 (2011), pp. 10161–10169. ISSN: 0957-4174. DOI: 10.1016/j.eswa.2011.02.075.

[138] Harish Garg. "A hybrid PSO-GA algorithm for constrained optimization problems". In: *Applied Mathematics and Computation* 274 (2016), pp. 292–305. ISSN: 0096-3003. DOI: 10.1016/j.amc.2015.11.001.

[139] Saptarshi Sengupta, Sanchita Basak, and Richard Alan Peters. "Particle Swarm Optimization: A survey of historical and recent developments with hybridization perspectives". In: *Machine Learning and Knowledge Extraction* 1.1 (2019), pp. 157–191.

[140] Jagdish Chand Bansal et al. "Inertia weight strategies in particle swarm optimization". In: *2011 Third world congress on nature and biologically inspired computing*. IEEE. 2011, pp. 633–640.

[141] Federico Marini and Beata Walczak. "Particle swarm optimization (PSO). A tutorial". In: *Chemometrics and Intelligent Laboratory Systems* 149 (2015), pp. 153–165. ISSN: 0169-7439. DOI: 10.1016/j.chemolab.2015.08.020.